PBRM1 loss in clear cell renal cell carcinoma leads to a proangiogenic phenotype via the CXCL5/CXCR2 axis that can be targeted by CXCR2 inhibition

Doctoral thesis

to obtain a doctorate (PhD)

from the Faculty of Medicine

of the University of Bonn

Ngoc Khanh Tran

from Ho Chi Minh City, Vietnam

2025

Written with authorization of

the Faculty of Medicine of the University of Bonn

First reviewer: Prof. Dr. med. Manuel Ritter

Second reviewer: Prof. Dr. med. Kerstin Junker

Day of oral examination: 26/05/2025

From the Department of Urology and Pediatric Urology, University Hospital Bonn and University Hospital Saarland

Table of contents

List of abbreviations

Abbreviation	Meaning
°C	Celsius degree
Ab	Antibody
AJCC	American Joint Committee on Cancer
AKT	Protein kinase B
ANOVA	Analysis of variance
ARNT	Aryl hydrocarbon receptor nuclear translocator
ATAC-seq	Assay for transposase-accessible chromatin using sequencing
BAF	BRG1-associated factor
BAH	Bromo-adjacent homology domain
BAP1	BRCA1 associated protein-1
BD	Bromodomain
BH	Benjamini-Hochberg
CA9/CA IX	Carbonic anhydrase IX
CAM	Chicken chorioallantoic membrane
ccRCC	Clear cell renal cell carcinoma
CD	Cluster of differentiation
cGAS/STING	Cyclic GMP-AMP synthase/stimulator of IFN genes
CI	Confidence Interval
CM	Conditioned-media
CPM	Counts per million
CTL	Cytotoxic T lymphocyte
CTLA-4	Cytotoxic T-lymphocyte associated protein 4
Ctrl	Control
CXCL	CXC ligand
CXCR	CXC receptor
DBS	Double-strand break
DEG	Differential gene expression
DNA	Deoxyribonucleic acid
DSS	Disease-specific survival
EC	Endothelial cell
ECM	Extracellular matrix
ECPM	Endothelial cell proliferation medium

ED	Embryonic development day
ELISA	Enzyme-linked Immunosorbent Assay
EPC	Endothelial progenitor cell
EPO	Erythropoietin
ERK	Extracellular signal-regulated kinase
EtOH	Ethanol
EZH2	Enhancer of zeste homolog 2
FBS	Fetal bovine serum
FDA	Food and drugs administration
FDR	False discovery rate
GSEA	Gene set enrichment analysis
GSK-3	Glycogen synthase kinase-3
HIF	Hypoxia-inducible factors
HMG	High-mobility group domain
HMVEC-L	Human lung microvascular endothelial cells
HR	Hazard ratio
HSPG	Heparan sulfate proteoglycan
HUVEC	Human umbilical vein endothelial cell
ICB	Immune checkpoint blockade
ICGC	International Cancer Genome Consortium
IFN	Interferon
Ig	Immunoglobulin
IL	Interleukin
IMDC	International mRCC Database Consortium
IQR	Interquartile range
JAK	Janus kinase
kDa	Kilo Dalton
KDR	Kinase insert domain receptor
KO	Knock-out
Log_2 FC	Log_2 fold change
M	Molar
m/v	Mass/volume
MAPK	Mitogen-activated protein kinase
MDSC	Myeloid derived suppressor cell
mg	Milligram

MIF	Macrophage migration-inhibitory factor
min	Minutes
ml	Millilitre
mM	Millimolar
mRCC	Metastatic renal cell carcinoma
mRNA	Messenger ribonucleic acid
mTOR	Mammalian target of rapamycin
mut/Mb	Mutations per megabase
ncBAF	Non-canonical BAF
NF-κB	Nuclear factor kappa-light-chain-enhancer of activated B cells
ng	Nanogram
NR	Not reached
NS	Not significant
ORR	Objective response rate
OS	Overall survival
PARPi	Poly-(ADP-Ribose) polymerase inhibitor
PBAF	Polybromo-associated BAF
PBRM1	Polybromo-1
PBS	Phosphate buffered saline
PCA	Principal component analysis
PD-1	Programmed death receptor-1
PD-L1	Programmed death-ligand 1
PDGFB	Platelet-derived growth factor B
Pen/Strep	Peniciline/Streptavidine
PFA	Paraformaldehyde
PFS	Progression-free survival
pg	Picogram
PI3K	Phosphoinositide 3-kinase
PLC	Phosphoinositide phospholipase C
PMSF	Phenylmethylsulfonyl fluoride
RECIST	Response Evaluation Criteria in Solid Tumours
RT	Room temperature
SCLC	Small cell lung cancer
SDS-PAGE	Sodium dodecylsulfate polyacrylamide gel electrophoresis
SETD2	SET domain containing 2

siRNA	Small interfering RNA
SNP	Single nucleotide polymorphism
STAT3	Signal transducer and activator of transcription 3
SWI/SNF	SWItch/Sucrose Non-Fermentable
TAMs	Tumor-associated macrophages
TANs	Tumor-associated neutrophils
TCGA	The Cancer Genome Atlas
TCGA-KIRC	Clear cell renal cell carcinoma from TCGA
TKI	Tyrosine kinase inhibitor
TMB	Tumor mutational burden
TME	Tumor microenvironment
TNF	Tumor necrosis factor
U	Unit
v/v	Volume/volume
VEGF	Vascular endothelial growth factor
VEGFR	Vascular endothelial growth factor receptor
VHL	Von Hippel-Lindau
w/v	Weigh/volume
WB	Western blot
WES	Whole exome sequencing
WT	Wild-type
µg	Microgram
µl	Microlitre

1. Introduction

1.1. Renal cell carcinoma: epidemiology, subtypes, and current treatments

In 2022, kidney cancers ranked 14th (434,419 new cases) and 16th (155,702 deaths) in terms of the most frequently diagnosed cancers and mortality worldwide, respectively (Bray et al., 2024). In the United States, it is expected that 81,610 newly-diagnosed kidney cancer cases and 14,390 deaths from kidney cancer in 2024 will be recorded (Siegel et al., 2024). In Germany, the incidence rates of kidney cancer were 6.6 (per 100,000 persons) for women and 15.2 for men in 2020; besides, the mortality rate in men (4.2) was double the mortality rate in women (1.9) (Barnes et al., 2024).

Renal cell carcinoma (RCC) is the predominant subtype of kidney cancer that accounts for roughly four-fifths of all kidney tumors (Escudier et al., 2019). Well-established risk factors of RCC include tobacco smoking, obesity, high blood pressure, and acquired cystic kidney disease (Kabaria et al., 2016). More than half of RCC cases are incidentally discovered through non-invasive imaging techniques. Currently, there is no effective screening modality for the early detection of RCC. The 5-year survival rate of RCC patients with localized disease is around 95%, but fewer than 20% patients with metastatic diseases survive 5 years (Kalra et al., 2016).

With regard to histologic categorization, RCC can be stratified into clear cell renal cell carcinoma (ccRCC) representing approximately 80% of all RCC and non-ccRCC including papillary RCC (app. 15% of all RCC), chromophobe (app. 5%), collecting tube (<2%), and other rare variants (Young et al., 2024). Each RCC subtype exhibits distinct gross and microscopic morphology as well as unique alterations at both gene and chromosomal levels (Linehan & Ricketts, 2019).

For patient with localized RCC disease, partial or radical nephrectomy by open, laparoscopic, or robot-assisted surgeries is the standard-of-care. On the other hand, patients with unresectable RCC tumors or metastatic RCC undergo systemic treatments. RCC, in general, is resistant to chemotherapy (Yagoda et al., 1993). Prior to 2005, doctors solely relied on two drugs, which were recombinant interleukine-2 (IL-2) and interferon-α (IFNα), to treat metastatic RCC (**Figure 1.1**) (Hsieh et al., 2017). Nowadays, vascular endothelial growth factor (VEGF) -targeted therapies or anti-angiogenic tyrosine kinase inhibitors (TKIs), mTOR inhibitors, and immune checkpoint blockades (ICBs) form the

backbone of RCC treatment that has help double the median survival from 15 months (treated with recombinant cytokines) to >30 months. In December 2023, the FDA approved the use of belzutifan, a selective HIF2α inhibitor, for patients with advanced ccRCC pretreated with either anti programmed death receptor-1 (PD-1) or programmed death-ligand 1 (PD-L1) inhibitor and VEGF/TKI based on the results of LITESPARK-005 study—a phase 3 clinical trial. The standard of care for treatment-naïve patients involves the combination of an PD-1 or PD-L1 drug with either an anti-VEGF/TKI agent or an intensified ICB with combination of anti-PD-1/ PD-L1 with a cytotoxic T-lymphocyte associated protein 4 (CTLA-4) inhibitor (Young et al., 2024). For second-line therapy, subsequent TKIs such as cabozantinib, axitinib, pazopanib, and sunitinib are preferred choices. To estimate prognosis in first-line and second-line treatments, patients can be assigned into three risk categories (favourable, intermediate, or poor) based on the International mRCC Database Consortium (IMDC) scoring system, including the following risk factors: Karnofsky performance status, time from diagnosis to treatment, hemoglobin, neutrophil count, platelet count, and calcium level (Heng et al., 2009; Ko et al., 2015).

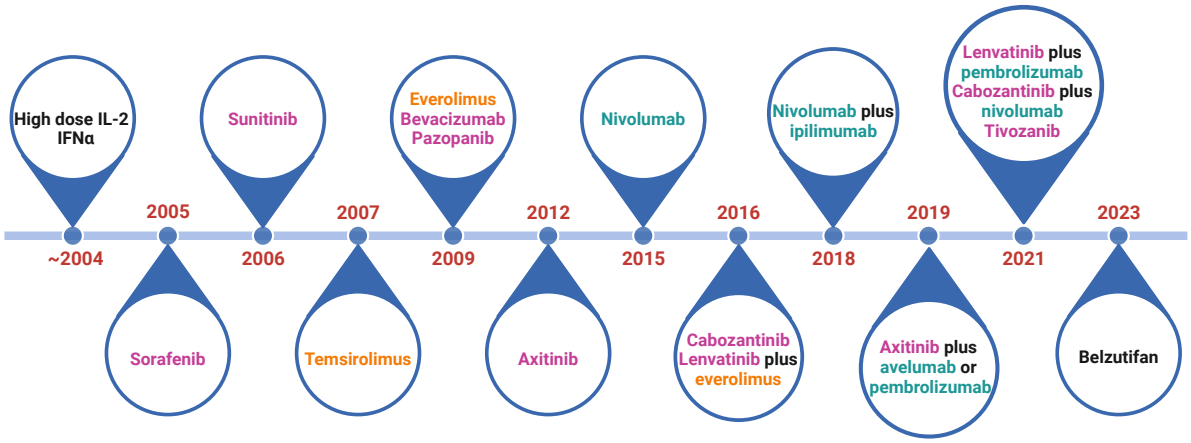

Figure 1.1: Approval timeline for systemic treatments in RCC. The therapeutic options evolve from dark ages (before 2005) to golden ages as a result of the advent of targeted therapies, including VEGF/TKI-targeted agents (pink), ICBs (light sea green), and mTOR inhibitors (orange).

1.2. Clear cell renal cell carcinoma

1.2.1. ccRCC histopathology and metastatic sites

ccRCC tumors—the most prominent RCC subtype—have a honeycomb-like architecture with small groups of polygonal or rounded cancer cells confined to a branching network of vasculatures. The name “clear cell” derives from the clear cytoplasm of cancer cells ascribed to the high cytoplasmic concentration of lipid and glycogen.

In the IMDC cohort, patients with ccRCC presented with a median of 2 metastatic sites, and some patients demonstrated distinct >5 metastatic sites (Dudani et al., 2021). The five most frequent metastatic settlements for ccRCC are the lung (70% of 9,252 ccRCC cases), lymph nodes (45%), bone (32%), liver (18%), and adrenal gland (10%). Critically, the location of metastasis is strongly associated with patients' overall survival (OS). In multivariable Cox regression analyses, pleura, brain, liver, and bone are metastatic sites that are correlated with the worst OS outcomes. In addition, ccRCC patients with pancreatic metastasis experience the longest median OS (50.1 months) and a 40% risk reduction for death (hazard ratio, 0.60 [95% CI, 0.51 to 0.72]; $P < .001$). Consistently, Singla and co-workers demonstrated that the presence of pancreatic metastases in ccRCC patients is a prognostic factor associated with better survival, independent of IMDC risk stratification (Singla et al., 2020).

1.2.2. ccRCC mutation profile

Large-scale exome sequencing revealed that there are four genes consistently mutated with frequencies of ≥ 10% with great variations across different ccRCC cohorts comprising von Hippel-Lindau (*VHL*) (52.3-82.4% of tumor specimens), Polybromo-1 (*PBRM1*) (32.9-46%) SET domain containing-2 (*SETD2*) (11.5-30%), and BRCA1 associated protein-1 (*BAP1*) (10.1%-19%) (Creighton et al., 2013; Farley et al., 2013; Hsieh et al., 2017; Nickerson et al., 2008; Varela et al., 2011). *VHL* is located on cytoband 3p25-26, and strikingly, *PBRM1*, *SETD2*, and *BAP1* are all situated in close proximity on cytoband 3p21. Furthermore, the deletion of loci 3p21 and 3p25 is frequent genomic event in ccRCC. Specifically, loss of the short arm of chromosome 3 with bands p21-p25 is detected in 94% (226/240) of ccRCC specimens using single nucleotide polymorphism (SNP) microarray analysis (Sato et al., 2013). In accordance with this, loss of heterozygosity in the 3p21-p25 region occurs in approximately 90% of ccRCC samples from The Cancer Genome Atlas (TCGA-KIRC) samples (Creighton et al., 2013). The TRACERx Renal study links loss of chromosome 3p with the concomitant gain of chromosome 5q (enhanced mTORC1 and MYC signaling) to chromothripsis, a phenomenon involving the rearrangements of chromosomal segments from one or a few chromosomes within circumscribed genomic regions (Mitchell et al., 2018). Moreover, the study extrapolated that the loss of 3p is an event preceding the introduction of mutations in the second allele

of *VHL*, *PBRM1*, *BAP1*, and *SETD2*, resulting in the biallelic inactivation of these genes. Notably, hypermethylation of CpG islands in the *VHL* promoter region is observed in 7-8% of ccRCC tumors (Creighton et al., 2013; Sato et al., 2013). In stark contrast, epigenetic silencing via promoter hypermethylation of *PBRM1*, *BAP1*, or *SETD2* is absent or an isolated event in ccRCC (Ibragimova et al., 2013).

1.2.3. ccRCC immunophenotype

The investigation of gene expression from TCGA cohorts demonstrated that ccRCC is among the most highly immune-infiltrated solid tumor, especially $CD8^+$ T cells, Th1 cells, Th17 cells, T central memory cells, and T effector memory cells (Şenbabaoğlu et al., 2016). The same observation that three-quarters of RCC samples have a high frequency of intratumoral $CD8^+$ T cells was reported by Braun and colleagues (Braun et al., 2020). Correspondingly, ccRCC has a high degree of immune cytolytic activity, which is determined by the level of granzyme A (*GZMA*) and perforin (*PRF1*) transcripts (Rooney et al., 2015). The putative underlying cause for increased T-cell infiltration in ccRCC is high tumor mutational load culminating in the expansion of the neoantigen pool that fosters antigen-specific T cell infiltration, thus better response to immunotherapy. However, ccRCC tumors have low tumor mutational burden (TMB) with a median of 1.42 mutations per megabase (mut/Mb; range: 0.035 – 2.77) compared to 14.4 mut/Mb (range: 8.0–24.9) in melanoma—a well-known immunological hot tumor (de Velasco et al., 2016; Hodis et al., 2012). In a pan-cancer analysis, 6 out of 30 cancer types, consisting of endometrial cancer, skin cutaneous melanoma, lung adenocarcinoma, cervical squamous cell carcinoma, bladder cancer, and colon adenocarcinoma, but not ccRCC, show a positive association between the level of $CD8^+$ T cell infiltration and neoantigen load (McGrail et al., 2021). Besides, when ccRCC tumors from CheckMate009, CheckMate010, and CheckMate025 datasets are dichotomized into TMB-high (≥ 10 mut/Mb) and TMB-low subgroups, counterintuitively, there is a higher response rate to nivolumab (an anti-PD-1 drug) in TMB-low tumors than TMB-high tumors. Moreover, an analysis using the same datasets does not show any correlation between baseline $CD8^+$ T cell infiltration and improved survival in nivolumab-treated patients (Braun et al., 2020).

1.3. pVHL and HIF in ccRCC

1.3.1. pVHL and hypoxia pathway in ccRCC

VHL—a tumor suppressor gene—codes for pVHL which is composed of 213 amino acids with the molecular weight of 30 kDa (Gossage et al., 2015). pVHL19, another isoform with a molecular weight of 19 kDa, contains less than the original pVHL 53 amino acid residues stemming from alternate translation-initiation site which the codons from 1 to 53 are excluded from translation. Both isoforms exhibit tumor suppressor function. pVHL, an E3 ubiquitin ligase, interacts with elongin C, elongin B, cullin 2, and the RING finger protein RBX1 to form the VCB–CR complex. Under physoxic conditions, the VCB-CR complex binds alpha subunit of hypoxia-inducible factor (HIF1α and HIF2α), which is hydroxylated by oxygen-sensing prolyl hydroxylases, and tags them with ubiquitin for proteasomal decay **(Figure 1.2)**. Hypoxia—a non-physiological low level of oxygen, typically 3-5% of O_2—is a universal characteristic of the majority of tumors facilitating tumor proliferation, angiogenesis, and metastasis (Muz et al., 2015). For example, the oxygenation level in non-cancerous kidney cortex is 9.5%; conversely, oxygen concentration in renal tumors drops to 1.3%. Due to tumor-intrinsic hypoxia and pseudohypoxia resulting from the lack of pVHL function in sporadic ccRCC patients, HIFα proteins are incessantly abundant. Consequently, transcriptional complexes between HIFα and HIF1β (or aryl hydrocarbon receptor nuclear translocator—ARNT) subunits are formed. The heterodimeric complexes then migrate to the nuclear and bind to hypoxia-response elements (HREs) to instigate the anomalous transcription of HIF-inducible genes, such as genes involved in angiogenesis and oxygen supply (*VEGF*; *PDGFB*, Platelet-derived growth factor B; *ANGPT2*, Angiopoietin 2; and *EPO*, Erythropoietin), in pro- and anti-apoptosis (*BNIP3/3L*; *PMAIP1*; *MCL1*; and *NPM1,* Nucleophosmin), and in glycolytic pathway (glucose transporters *SLC2A1*-GLUT1, as well as *SLC2A3*-GLUT3; and 12 essential enzymes for glycolysis) (Dengler et al., 2014). Indeed, hypoxia, angiogenesis, and glycolysis pathways are substantially activated in ccRCC tumors relative to normal kidney tissues in a multi-omics analysis of treatment-naïve tumors (Clark et al., 2019). Furthermore, HIFs can exert their gene-expression regulatory function through upregulating expression of several microRNAs and histone demethylases.

Although biallelic inactivation of *VHL* is a truncal event in ccRCC tumor evolution (Gerlinger et al., 2014; Mitchell et al., 2018), the loss of *VHL* alone is inadequate for cell transformation and ccRCC initiation. Homozygous knockout of *Vhl* in kidney of genetically engineered mice using various Cre drivers exclusively expressed by specific renal epithelial cell types, consisting of *Pepck*, *Pax8*, and *Thp*, has failed to produce ccRCC tumors despite of initial formation of renal cysts (Kapitsinou & Haase, 2008). Mitchell and colleagues have approximated that there is a time lag of 15 to 30 years from the loss of both *VHL* alleles to the first diagnosis of RCC using Bayesian mathematical modeling (Mitchell et al., 2018).

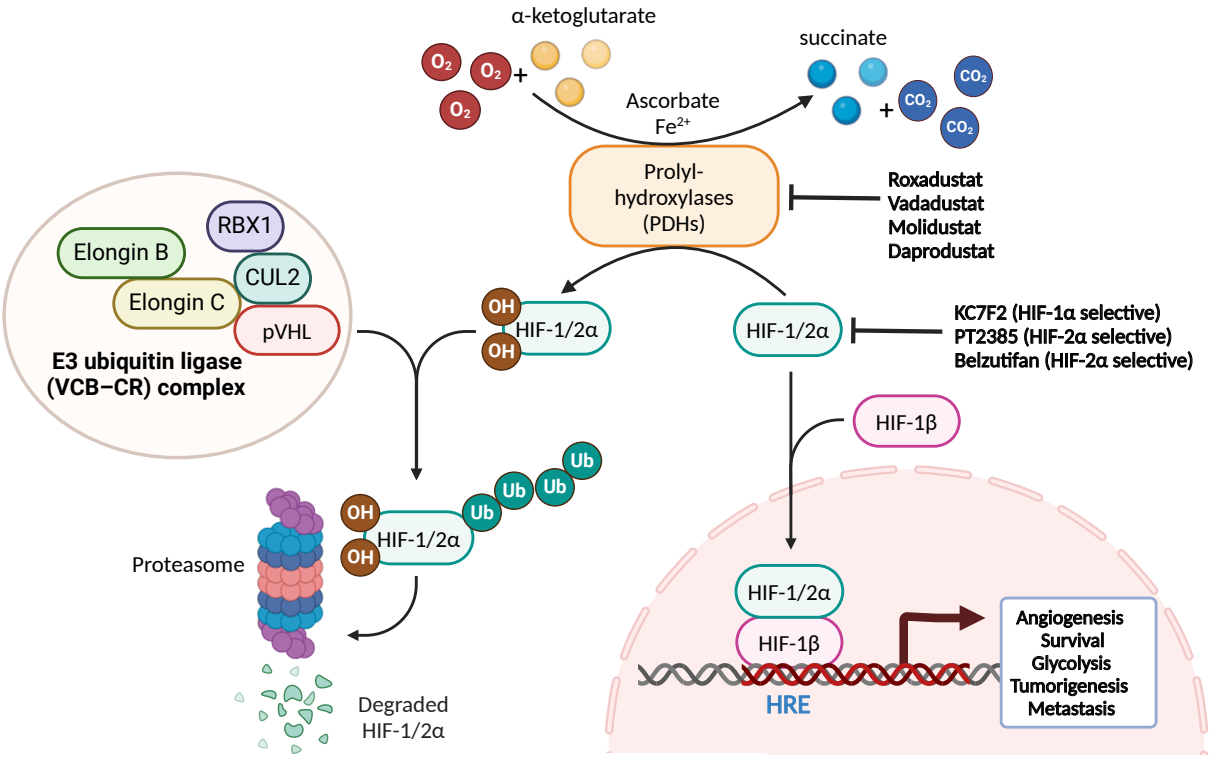

Figure 1.2: The molecular machinery underlying hypoxia response. Under normoxia, oxygen-dependent prolyl hydroxylase domains (PHDs) hydroxylate specific proline residues within hypoxia inducible factor α (HIFα) subunits, which in turn can be recognized and decorated with ubiquitin by von Hippel–Lindau protein (pVHL) for degradation by proteasomes. Under hypoxia, the enzyme activity of PHDs is abrogated, allowing the dimerization between HIFα and HIFβ subunits and the activation of HIF-regulated genes. Pharmacological inhibition of PHDs has been approved for the treatment of anaemia in patients with chronic kidney disease. Besides, targeting HIFα has emerged as a novel therapeutic choice for RCC. CUL2, cullin 2; HREs, hypoxia-response elements; RBX1, RING finger protein.

1.3.2. The HIF transcription factor family and its related downstream pathways

HIFs act as transcription factors that consist of a HIFα protein (HIF1α, HIF2α, or HIF3α) and a constitutively-expressed HIF1β (Gossage et al., 2015). HIF1α can be found in

almost all tissues of the body. In contrast, HIF2α is restrictedly expressed in endothelial, lung, renal and hepatic cells, while HIF3α is specific to the heart, lung, skeletal muscle, and placenta (Duan, 2016). HIF1α, HIF2α, and full-length HIF3α are transcription activators, whereas HIF-3α4—an alternative spliced variant that is devoid of the oxygen-dependent degradation domain (ODD) and trans-activation domains—functions as dominant-negative repressor. The transcriptional repertoires activated by HIF1α or HIF2α overlap but are not identical (Keith et al., 2012). While HIF1α favorably modulates the expression of glycolysis-associated genes, HIF2α regulates various genes with diverse functions, for instances erythropoiesis, cell cycle progression, and growth factor.

Strikingly, c-Myc, a proto-oncogene that stimulates cell cycle progression and proliferation, is augmented by HIF2α, but is repressed by HIF1α (Gordan et al., 2007). Though both HIF1α and HIF2α possess PER/ARNT/SIM (PAS)-B domain in their structures, HIF1α outcompetes HIF2α in binding to SP1, a c-Myc cofactor, via PAS-B owing to the phosphorylation of HIF2α at threonine-324 residue. The consequence of the lack of c-Myc/SP1 interaction due to the HIF1α-SP1 binding is the attenuation of c-Myc transcriptional repression of *CDKN1A, CDKN1B* (p21 and p27, respectively—cyclin-dependent kinase inhibitors), *MSH2*, *MSH6* (DNA mismatch repair protein), and *NBN* (subunit of DNA double strand break). Moreover, HIF1α dislocates MAX from c-Myc/MAX complexes, obviating c-Myc/MAX heterodimer binding to target promoters, which in turn depleting the expression of cell cycle-promoting genes such as *CCND2* (G1/S specific cyclin D2), and *E2F1*, while elevating the expression of *CDKN1A, CDKN1B*. Conversely, in the presence of accumulated HIF2α, more c-Myc/MAX complexes are stabilized, thus triggering the opposite transcriptional effects. HIF2α/c-Myc actuates a successful cell cycle not only via modulating cyclins and cyclin inhibitor, but also through restricting DNA damage by inducing the expression of BRAC1 and BARD1—key players in homologous recombination repair, accordingly less formation of γH2AX—a sensitive indicator of DNA double strand breaks (Gordan et al., 2008). In agreement with these molecular mechanistic insights, ccRCC pVHL-deficit tumor growth in both in vitro and in xenograft nude mice model was accelerated either by overexpression of HIF2α using retroviral vector or by downregulation of HIF1α using short hairpin (Raval et al., 2005; Shen et al., 2011). On the other hand, deactivation of HIF2α via knockdown or pharmacological

inhibition has been shown to suppress ccRCC tumor formation in the aforementioned models (Cho et al., 2016).

1.3.3. The roles of HIF1α and HIF2α in ccRCC

There's a propensity for HIF2α expression to occur concurrently with HIF1α deficiency in a subset of ccRCC clinical samples. Loss of long arm of chromosome 14, which harbors *HIF1A,* is observed in 45% samples of TCGA-KIRC cohort (Creighton et al., 2013) and is associated with significant reduction in OS (Monzon et al., 2011). In the TRACERx renal population, co-deletion of chromosomes 9p and 14q soars from 35% of cases with only primary tumors at presentation to 71% of cases with metastatic diseases, supporting that the collateral loss of 9p and 14q is the primary force of metastasis in ccRCC (Turajlic et al., 2018). Of note, non-silent mutations of *HIF1A*, observed at a frequency of less than 1% that is independently validated in two ccRCC cohorts (Creighton et al., 2013; Dalgliesh et al., 2010), represents another mechanism to diminish HIF1α expression and activity. Together, these lines of evidence substantiate the tumor-suppressive role of HIF1α and the oncogenic role of HIF2α. Interestingly, Hoefflin and colleagues highlighted that HIF1α is necessitated for ccRCC tumor initiation in conditional knock-out *Vhl*$^{fl/fl}$, *Trp53*$^{fl/fl}$, *Rb1*$^{fl/fl}$ mice (Hoefflin et al., 2020). As a result, the HIFα subunits, especially HIF2α, have emerged as a promising target for new line therapy in ccRCC, which is proven by the recent FDA approval of belzutifan, a selective HIF2α inhibitor, for patients with advanced ccRCC. The first interim analysis of LITESPARK-005 study showed that belzutifan is superior to everolimus concerning progression-free survival (PFS), drug tolerability, and patients' quality of life (Choueiri et al., 2024). The estimated percentage of patients who were alive and had no disease progression at 18 months was 24% (95% CI, 19.0 to 29.4) in the belzutifan group and 8.3% (95% 4.9 to 12.7) in the everolimus group. The objective response rate (ORR), assessed according to Response Evaluation Criteria in Solid Tumours **(**RECIST) 1.1, at 25 months was 22.7% (95% CI, 18.6 to 27.3) in the belzutifan group and 3.5% (95% CI, 1.9 to 5.9) in the everolimus group.

1.4. Polypromo-1

1.4.1. PBRM1 protein structure

PBRM1, also known as BAF180, is a specific-subunit of the chromatin remodeling Polybromo-associated BAFs (PBAFs) complex—a subfamily of SWItch/Sucrose Non-Fermentable (SWI/SNF) complexes. The SWI/SNF complexes regulate gene expression through transiently mobilizing nucleosomes so that the transcriptional machinery can access the DNA and initiate transcriptional responses. More than one copy of PBRM1 exist in each PBAF complex (Mashtalir et al., 2018). PBRM1 is the last subunit to be assembled to finalize the PBAF complexes, thus deletion of PBRM1 does not disturb PBAF complex assembly. PBRM1 is composed of six tandem bromodomains (BDs) that collaboratively bind nucleosomes decorated with acetylated lysine residues on histone tails, along with two bromo-adjacent homology (BAH) domains, and a high-mobility group (HMG) domain. The interaction between specific histones, such as H3K14ac, H3K4me3, or H4K16ac, and PBRM1 is primarily facilitated by BD2 and BD4, which can be further enhanced by BD1 and BD5 but reduced by BD3 (Slaughter et al., 2018). Missense mutations in BD4 of PBRM1 or a PBRM1 variant lacking all six BDs accelerates cell proliferation, while the loss of both BD1 and BD2 does not give rise to the same effect (Gao et al., 2017). The BD4 of PBRM1 is also pivotal for the recognition of acetylated lysine 382 of p53 (Cai et al., 2019). The abolishment of PBRM1-p53 interaction due to BD4-mutated PBRM1 dampens the transcriptional activation of certain p53-target genes, especially *CDKN1A*, which encodes for p21, and thus fails to suppress ccRCC growth in mouse model.

1.4.2. *PBRM1* mutations in ccRCC pathogenesis

PBRM1 mutations are not unique to ccRCC and also frequently occur in gastric adenocarcinoma or urothelial cancer as well as in other cancer entities at a lower rate (Mittal & Roberts, 2020). In ccRCC, *PBRM1*-inactivating mutations are the second most common event preceded by *VHL* mutations (Varela et al., 2011). *PBRM1* mutation is a truncal event that drives cancer progression and metastasis, as evidenced by 74% of ccRCC cases harboring clonal *PBRM1* mutations (Turajlic et al., 2018) and 90% (87/97 patients) concordance of *PBRM1* mutations between primary and matched metastatic ccRCC tumors (Eckel-Passow et al., 2017). Remarkably, Turajlic and colleagues

employed intra-tumoral multi-region-based sequencing and observed that the *PBRM1* mutation and *BAP1* mutation are not co-occurrence at the clonal level, but instead co-exist and are distinctively distributed in subclones with disparate evolutionary trajectories in the same ccRCC patient (Turajlic et al., 2018).

Kidney-specific genetic ablation of either *Vhl* or *Pbrm1* in *Pax8-Cre* mice does not engender kidney tumors (Espana-Agusti et al., 2017), while the co-current knock-out of both *Vhl*$^{fl/fl}$/*Pbrm1*$^{fl/fl}$ by either *Pax8* or *Ksp* Cre driver induces the formation of low-grade tumors that moderately resemble human ccRCC tumors in terms of the presence of clear cytoplasmic (abundant lipid and glycogen) cancer cells, positive staining for carbonic anhydrase IX (CA9) (ccRCC common marker), CD31 (endothelial marker), and Ki-67 (proliferation maerker), and the abundance of HIF1α and HIF2α, culminating in the mounting activation of HIF-dependent pathways (Gu et al., 2017; Nargund et al., 2017). It is noteworthy that co-deletion of both *Vhl*$^{fl/fl}$/*Pbrm1*$^{fl/fl}$ by either *Villin or Sglt2*—both express restrictedly in proximal tubule epithelial cells—Cre driver fails to induce tumors (Gu et al., 2017), which brings into question of the general belief that the cells of origin in ccRCC are proximal tubule epithelial cells.

1.4.3. *PBRM1* as predictive biomarker in ccRCC

The predictive role of *PBRM1* mutation has been immensely investigated in both ICB-based and VEGF/TKI-based therapies. The IMmotion150 phase 2 clinical trial compared atezolizumab + bevacizumab and atezolizumab monotherapy with sunitinib in previously untreated patients with locally advanced or metastatic RCC (McDermott et al., 2018). Whole exome sequencing (WES) of 201 tumors in this study showed that 44% cases have *PBRM1* alterations. Moreover, in sunitinib-treated groups, patients with mutated *PBRM1* experienced PFS advantage, with a 62% risk reduction for death, compared with those without mutations; this prolonged survival is not observed in either atezolizumab + bevacizumab or atezolizumab monotherapy group. In the phase 3 JAVELIN Renal 101 trial (N = 733), which compared avelumab + axitinib versus sunitinib as first-line treatments in RCC patients, investigators examined the effect of *BAP1*, *PBRM1*, *MTOR* and *VHL* mutations on PFS (Motzer et al., 2020). Contrary to the findings of the IMmotion150 trial, PFS is similar within both treatment arms notwithstanding the *PBRM1* mutation status. In the CheckMate 214 cohort, 1082 patients were randomized to

receive nivolumab plus ipilimumab or sunitinib in RCC as first-line treatment with WES data available for 481 patients (Motzer et al., 2022). 32% of the genomic-analyzed cases are *PBRM1* mutated. In patients with *PBRM1* wild-type (WT), PFS is significantly longer in the ICB combination group (p=0.04) but not in the sunitinib group. After multiple hypothesis testing adjustment, neither PFS nor OS differs based on *PBRM1* mutation status. Altogether, at least in the first-line setting, it seems that *PBRM1* mutations are modestly predictive in the anti-VEGF/TKI but not with ICB therapy. A meta-analysis of 9 publications, which used *PBRM1* mutated status and PFS to evaluate *PBRM1* predictive potential, concluded that patients with *PBRM1* mutations showed survival gains by anti-VEGF agents in the first-line treatment and by ICBs in the second-line therapy (Ghiglione et al., 2022).

1.5. Tumor Angiogenesis

1.5.1. Historical perspective

Half a century has passed since Judah Folkman conceptualized angiogenesis as not merely a by-product of excessive tumor proliferation, but rather an essential driver of tumor growth (Folkman, 1971). He is the first to coin the term “anti-angiogenesis” and postulate that the inhibition of angiogenesis would be a powerful approach for cancer therapy. Subsequently, in the early 1990s, Kim et al. elucidated the critical role of VEGF in tumor neo-vascularization *in vivo*; consistently, the suppression of vascular network formation as well as tumor growth was achieved *in vivo* by using a VEGFA antibody (Kim et al., 1993). Later, tumor angiogenesis was recognized by Hanahan and Weinberg as a distinct hallmark of cancer (Hanahan & Weinberg, 2000). The introduction of bevacizumab into the first and second line treatments of metastatic colorectal cancer marks a significant milestone in cancer therapy (Hurwitz et al., 2004), thereby sparking interest in developing a plethora of biologic drugs and TKIs targeting diverse angiogenic pathways that were subsequently approved for use in various cancer types (Kuo et al., 2024).

1.5.2. The “angiogenic switch” and the morphological traits of tumor vasculature

The sprouting and branching of new vessels from the preexisting ones under normal healthy conditions, namely physiological angiogenesis, happens during embryonic development but is inactive in adults with the exception of female reproductive cycle and

wound-healing (Bergers & Benjamin, 2003; Chung et al., 2010). Vascular homeostasis is in balance due to the precise synchronization between endogenous pro-angiogenic factors and anti-angiogenic signals (thrombospondin-1, angiostatin, endostatin, canstatin, and tumstatin). In cancer, there is a pre-vascular phase with the absence of angiogenic activity. In this stage, tumor mass is relatively small (a few cubic millimeters) and malignant cells are mostly at their dormant state (Folkman & Kalluri, 2003). When the pro-angiogenic signals tip over because of metabolic stress (hypoxia, low pH, low glucose and high reactive oxygen species), mechanical stress, accumulation and activation of oncogenes (*MYC*, *KRAS*, and *SRC*), and inflammatory responses, the formation of new blood vessels from the parental capillaries is initiated, also known as “angiogenic switch”, which in turn instigating the exponential growth of the malignant cells.

Unlike the hierarchically organized vasculature of non-malignant tissues, tumor blood vessels are characterized by their chaotic and tortuous architecture (Martin et al., 2019; Morikawa et al., 2002). This disorganized structures often marked by excessive branching, uneven shapes, and blind ends, results from a constant flux of proangiogenic signaling. The discontinuous layer of endothelial cell (EC) lining of these vessels, the reduction of pericyte coverage, the abundant fenestrations, and the anomalous formation of basement membrane all contribute to irregular perfusion, fluid leakage, and microhemorrhaging within tumors. Additionally, the compression of vessels caused by mechanical forces from proliferating cancer cells and their extracellular matrix (ECM) exacerbates vascular hyperpermeability and drastically reduces blood flow. This poor blood flow aggravates hypoxic and acidic tumor microenvironment (TME) as well as limits the extravasation of immune cells especially cytotoxic T lymphocytes (CTLs), and the delivery of therapeutic agents to the tumor site.

1.5.3. The mechanisms of tumor vascularization

Different mechanisms are exploited by tumor to induce tumor vascularization (**Figure 1.3**). First, sprouting angiogenesis is a complex, multi-step process that predominates as the primary mechanisms of tumor angiogenesis (Hillen & Griffioen, 2007). This process begins with the activation of ECs by specific growth factors binding to their receptors, which leads to the localized degradation of the ECM and basement membrane by activated proteases. In consequence, ECs can proliferate and migrate to the surrounding

matrix. A single cell at the tip of parent vessel, so called “tip cell”, becomes leading migratory cell, leading vessel elongation towards a chemotactic gradient and inhibiting adjacent cells from adopting the same fate through lateral inhibition. The “stalk cells” are differentiated under the effect of the tip cell, successively proliferate and construct new blood vessel lumen, which eventually connects with the parental vessel. The newly formed vascular sprouts then connect with each other through anastomosis, enabling complete perfusion of the vascular network. Intussusceptive angiogenesis involves the formation of transluminal tissue pillars within existing blood vessel, which then splits this preexisting vessel into two new vessels. The process was first discovered in capillary remodeling in lung (Caduff et al., 1986). Intussusceptive angiogenesis has an advantage over sprouting in terms of energy efficiency due to negligible requirement for EC proliferation and migration. Vasculogenesis refers to the de novo formation of blood vessel through the recruitment of bone-marrow derived endothelial progenitor cells (EPCs) to the tumor site and the differentiation of these cells into mature ECs. EPCs express specific markers, including CD34, VEGFR2, CD31, CD146, and CD144 (Chambers et al., 2021). The trans-differentiation of cancer stem cells into ECs and pericytes, leading to neovascularization, has been documented in several tumor types. This phenomenon initially observed in glioblastoma; the researchers even detected somatic mutations in ECs within tumors that are similar to those carried by the cancer cells themselves, further supporting the idea of a neoplastic origin for these endothelial-like cells. Vasculogenic mimicry is accomplished by the organization of cancer cells to form vessel-like structures that proactively help maintain sufficient supply of nutrients and oxygen for their growth, thus bypassing the involvement of ECs. Vasculogenic mimicry is principally observed in aggressive tumors and is associated with poor prognosis in various cancers. Finally, vessel co-option is a non-angiogenic mechanism by which cancer cells migrate along the basolateral side of pre-existing blood vessels or invade the tissue area between these vessels, ultimately gaining access to host vasculature to satisfy their soaring metabolic demands. Vessel co-option as well as vasculogenic mimicry are contributory factors to the limited success of anti-angiogenic therapies as they allow tumors to circumvent the requirement for new blood vessel formation.

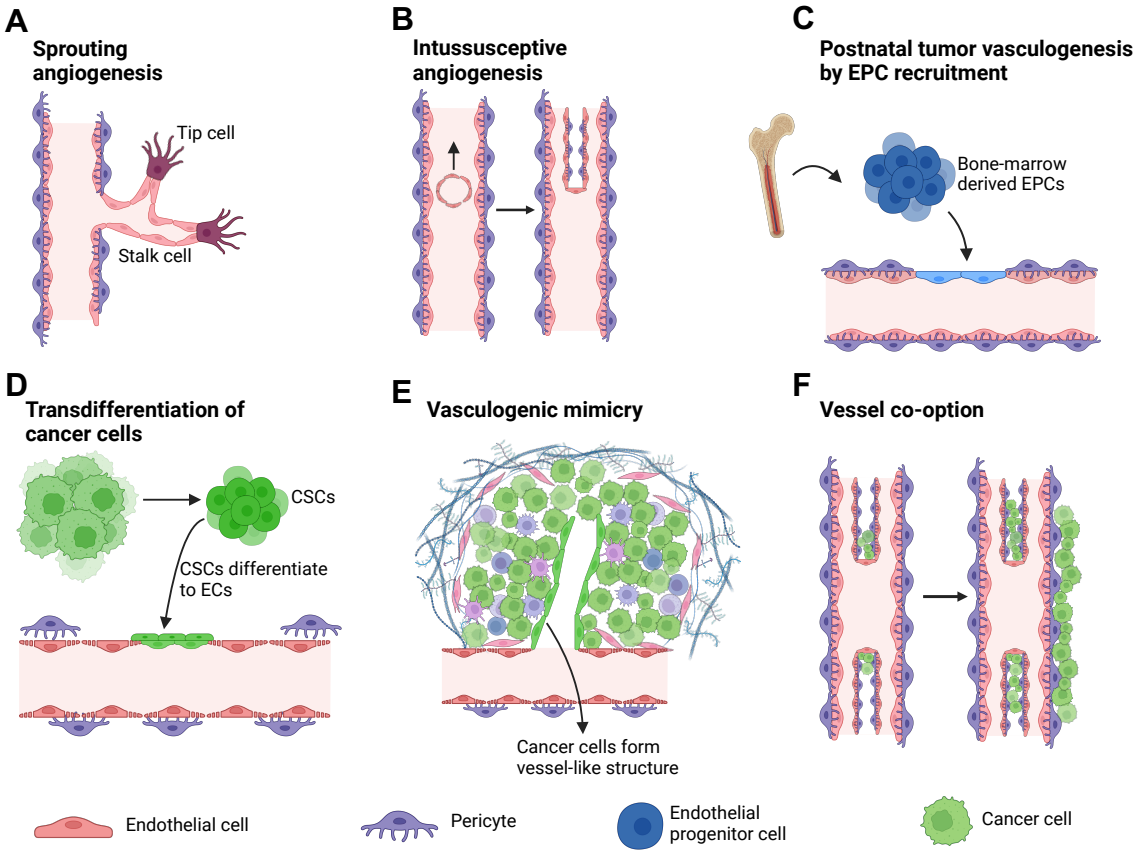

Figure 1.3: Modes of tumor vascularization. (A) Sprouting angiogenesis is primarily induced in response to VEGFA. Tip endothelial cells (ECs) sense and migrate along VEGFA gradient, while proliferative ECs called stalk cells form the nascent vascular lumen during sprouting extension. (B) Intussusceptive angiogenesis refers to the process of forming new blood vessels by splitting a parental vessel into two. (C) Bone-marrow-derived endothelial progenitor cells (EPCs) are recruited and contributed to vascular de novo formation. (D) Tumor ECs can be generated from cancer stem cells (CSC) through transdifferentiation and give rise to new blood vessels. (E) Vasculogenic mimicry is the formation of vasculature network by the lining of cancer cells that is independence of EC activity. (F) Vessel co-option is the hijacking of pre-existing tissue blood vessels by tumor to support its rapid growing during expansion and evasion. (Adapted from (Carmeliet & Jain, 2011)

1.5.4. VEGFA, the anti-angiogenic therapy, and modes of resistance to anti-angiogenic therapy

VEGFA is the most extensively-investigated pro-angiogenic mediator in cancer. The VEGF family belongs to the cystine-knot growth-factor superfamily, with eight conserved cysteine residues that form four sulfide bridges in its structure. VEGFA, VEGFB, VEGFC, VEGFD, and placental growth factor (PlGF) are five known members of the VEGF group (Pérez-Gutiérrez & Ferrara, 2023). The secreted homodimers or heterodimers of these proteins bind to specific tyrosine kinase receptors—VEGFR1, VEGFR2, and VEGFR3—on the cell surface. The most potent angiogenic stimulator is VEGFA which exists in six

alternatively spliced isoforms in human (Holmes & Zachary, 2005). VEGFA exerts its main functions through VEGFR2, alternatively known as the kinase insert domain receptor (KDR), activation. $VEGFA_{165}$ is the most produced and biologically significant isoform owing largely to its ability to bind both cell surface- and ECM- expressed heparan sulfate proteoglycans (HSPGs); the presentation of $VEGFA_{165}$ by HSPGs amplifies signaling through VEGFR2. Upon VEGFA-VEGFR2 binding, downstream signal transductions are mediated via the PLCγ-MAPK-ERK and PI3K-AKT-mTOR pathways, consequently promoting EC proliferation, survival, migration, and permeability.

Current strategies for targeting angiogenesis in cancer therapy include several approaches, monoclonal antibodies targeting VEGFA, or VEGR2 such as bevacizumab and ramucirumab; decoy receptors referred to as 'VEGF-trap'—aflibercept; and multi-target TKIs, for example sunitinib, axitinib, and pazopanib, which not only inhibit VEGFRs but also antagonize PDGFRs, KIT, SRC, RET, TIE2, and MET (Ye, 2016). The original rationale for the development of these therapies was to eradicate blood vessel formation and starve malignant cells of nutrients and oxygen. Rather contradictorily, anti-angiogenic agents can transiently repair and advance vessel remodeling, alluded to as "vessel normalization", thereby improving blood perfusion, alleviating interstitial fluid pressure, enhancing drug delivery, and mitigating immunosuppressive TME by facilitating the trafficking of CTLs. This notion originally proposed by Rakesh K. Jain (Jain, 2001) and has been wildly accepted based on ample preclinical and clinical evidence (Martin et al., 2019). Winkler and colleagues used human glioblastoma xenograft model to demonstrate that VEGFR2 antibody treatment generates a "normalization window" characterized by remarkable amelioration of tumor oxygenation, during which radiation therapy is most effective (Winkler et al., 2004). Within this timeframe, the increased trafficking of pericytes to the tumor vasculature network is facilitated by the significant expression of angiopoietin-1 in tumor cells. Additionally, the thickened basement membrane of brain tumor vessels becomes thinner as a result of increasing activity of matrix metalloproteinases, in turn elevating degradation of type IV collagen. A phase 1 clinical trial conducted by Willett et al. examined the pharmacologic effects of bevacizumab on rectal carcinoma vasculature (Willett et al., 2004). By day 12, tumor vessels begin to normalize and resume normal functions as detected by no changes in vessel permeability as well as 18-fluorodeoxyglucose uptake despite the reduction of vascular volume and microvascular

density, the reduced interstitial fluid pressure, and the enhanced pericyte coverage evidenced by the augmented fraction of vessels positive for α-smooth muscle. In recurrent glioblastoma, cediranib—a multi-target TKI—treated patients, only those whom the increased blood perfusion confirmed by magnetic resonance imaging experienced improved survival (Sorensen et al., 2012).

Despite the broad application of anti-VEGF drugs in multiple cancers, for instance, RCC, colorectal cancer, non-small cell lung cancer, and gynecological cancers, patients experience incremental benefit in terms of OS (Ye, 2016). Furthermore, even though anti-angiogenesis is predicated on the prerequisite of tumor neovascularization to meet its heavy demand for oxygen and nutrients, melanoma, pancreatic cancer, and prostate cancer are resistant to anti-angiogenic agents. Several mechanisms of resistance to the inhibition of the VEGF/VEGFR axis have been described thus far (De Palma et al., 2017). The first mechanism involves the upregulation of VEGF-independent pro-angiogenic circuits. A plethora of factors such as growth factors (fibroblast growth factors (FGFs), PDGF family, angiopoietins (ANGPTs), insulin-like growth factor 1 (IGF1), and hepatocyte growth factor (HGF)), chemokines (CXCR2-binding ligands and CXCL12), cytokines (interleukin-1β (IL1β), transforming growth factor-β (TGFβ), and tumor necrosis factor-α (TNFα)), proteases, and ECM glycoproteins can directly or indirectly be involved in EC activation and induction of tumor angiogenesis, thus evading the blockage of VEGF signaling. Second, therapy-mediated increased secretion of granulocyte colony-stimulating factor (G-CSF), CXCL12, IL-8, and chemokine ligand 2 (CCL2) promotes the recruitment of neutrophils/macrophages, and cancer-associated fibroblasts (CAF) that secrete multiple aforementioned proangiogenic growth factors, which successively perpetuate tumor vascularization. Third, in spite of the scarcity of oxygen and nutrients, sustainable tumor growth can be maintained via triggering stress response—for example increasing autophagy, or reprogramming metabolism of cancer cells. In particular, the malignant cells augment the fatty acid uptake and lipid drop accumulation that allow ATP production via fatty acid catabolism. Additionally, tumor cells can activate ‘metabolic symbiosis’, a procedure whereby the cells in hypoxic areas use anaerobic glycolysis to generate energy and release lactate, while the better-oxygenated cell close to tumor blood vessel uptake the excreted lactate for oxidative phosphorylation. The final resistant

mechanism associates with vessel co-option and vasculogenic mimicry that have been mentioned above.

1.6. Aims of the thesis

Although anti-angiogenic drugs including anti-VEGF antibodies, TKIs and anti-HIF2a inhibitors now have become an established part of RCC treatment regimens, the response to these treatments is mostly temporary and ultimately the tumors become resistant. Previous studies have shown that the loss of *PBRM1* in ccRCC is associated with an enhanced angiogenic signature (Hakimi et al., 2019; McDermott et al., 2018). The exact molecular mechanisms, such that how *PBRM1*-loss affects the interaction of ccRCC tumor cells with the tumor microenvironment and to what extent this explains the clinically observed resistance, are still enigmas. The objective of this thesis is to explore alternative, potentially targetable molecular mechanisms—beyond PBRM1 deficiency-enhanced VHL-loss-induced hypoxia response leading to increased VEGFA expression—that drive the proangiogenic phenotype in *PBRM1*-mutated ccRCC. In brief, we employed several pharmacological compounds to disrupt the interaction of PBRM1 with their targets, and explored the resulting changes in the transcriptomic profile of ccRCC cells. The findings were further validated exploiting CRISPR/Cas9-mediated *PBRM1*-knockout ccRCC cells. The clinical significance of these results in patients with or without *PBRM1*-mutated ccRCC tumors was also evaluated. Besides, the impact of *PBRM1*-loss on angiogenesis were investigated by assessing the proliferation, signaling activation, and capillary formation of endothelial cells cultured in supernatant of PBRM1-deficient cancer cells. Ultimately, the anti-tumor potential of targeting the newly-identified angiogenic axis in ccRCC were showcased using an in ovo xenograft model.

2. Material and methods

2.1. Materials

Table 1: Cell lines and primary cells

Cell line/ Primary cell	**Cell type**	**Culture medium**	**Source**
Caki1	human clear cell renal cell carcinoma from metastatic site (skin)	90% RPMI 1640 + 10% FBS + 2 mM L-Glutamine + 1% Pen/Strep (R10+ medium)	DSMZ
786O	human renal cell carcinoma	90% RPMI 1640 + 10% FBS + 2 mM L-Glutamine + 1% Pen/Strep (R10+ medium)	ATCC
OSRC2	human clear cell renal cell carcinoma	90% RPMI 1640 + 10% FBS + 2 mM L-Glutamine + 1% Pen/Strep (R10+ medium)	CLS Cell Lines Service GmbH
KMRC1	human clear cell renal cell carcinoma	90% RPMI 1640 + 10% FBS + 2 mM L-Glutamine + 1% Pen/Strep (R10+ medium)	Japanese Cancer Research Resources Bank
NCI-H1048	human small cell lung cancer	90% DMEM/F-12, GlutaMAX™ Supplement + 10% FBS + 2 mM L-Glutamine + 1% Pen/Strep (R10+ medium)	
HUVECs	human umbilical vein endothelial cells	Endothelial cell proliferation medium (ECPM)	Provitro

Table 2: Cell culture media and supplements

Item	**Source**
Roswell Park Memorial Institute (RPMI) 1640 Medium	Gibco - Life Technologies
Dulbecco's Modified Eagle Medium (DMEM)	Gibco - Life Technologies
Penicillin-Streptomycin (10.000 U/ml - 10000 µg/ml))	Gibco - Life Technologies
UltraPure™ DNase/RNase-Free Distilled Water	Gibco - Life Technologies
L-Glutamine (200 mM)	Gibco - Life Technologies
Fetal bovine serum (FBS)	Gibco - Life Technologies
Dulbecco's phosphate-buffered saline (DPBS)	Gibco - Life Technologies
Endothelial cell proliferation medium, FCS	Provitro
Trypsin-EDTA (0.25%), phenol red	Gibco - Life Technologies
Accutase	Invitrogen
Opti-MEM® I, reduced serum medium, no phenol red	Gibco - Life Technologies
10X Medium 199	Sigma-Aldrich
DMEM/F-12, GlutaMAX™ Supplement	Gibco - Life Technologies
Medium 199, Earle's Salts	Gibco - Life Technologies
Medium 199 10X, Earle's Salts, without L-glutamine and sodium bicarbonate	Sigma-Aldrich

Table 3: Equipment

Item	**Source**
TC20 Automated Cell Counter	Bio-Rad
MDF-1156-PE Cryogenic ULT Ultra Low Chest Freezer -150°C	Sanyo
ChemiDoc MP Imaging System	Bio-Rad Laboratories
Eppendorf Reference ® multichannel pipette 300	Eppendorf
Eppendorf Reference ® pipette (2.5,10,20,100,1000 µl)	Eppendorf
Centrifuge 5810R/5415C/5415R/5430R/5424	Eppendorf
PHCbi MCO-170AIC-PE IncuSafe CO2 Incubator	PHC Group
MSC-Advantage™ Class II Biological Safety Cabinets	Thermo Scientific

HERAfreeze™ HFU T Series -86°C Upright Ultra-Low Temperature Freezers	Thermo Scientific
Inverted Phase Contrast Microscope ECLIPSE TS100 LED	Nikon
Water bath TW20	Julabo GmbH
Platform rocker, PMR-30	Grant-Bio
Upright BX43 microscope	Olympus
Thermomixer comfort	Eppendorf
Heraeus HERAcell 240 incubator	Thermo Scientific
Explorer™ Precision Precision Balance EX2202/E Scale	Ohaus
NanoDrop One/Onec Microvolume UV-Vis Spectrophotometer	Thermo Scientific
Pipette controller, accu-jet® *pro*	Brand
Mini-PROTEAN® Tetra Vertical Electrophoresis Cell (Tank, lid with power cables, electrode assembly, gel casting module, casting stands with gaskets, casting frames, 15-well combs, glass plates, spacer plates with integrated 1.5 mm spacers)	Bio-Rad Laboratories
Mini Trans-Blot Modular system (gel holder cassettes, foam pads, electrode assembly, cooling unit)	Bio-Rad Laboratories
Mini-PROTEAN® Tetra Vertical Electrophoresis Cell	Bio-Rad Laboratories
Power Pac HC Universal Power Supply	Bio-Rad Laboratories
Spark® Multimode Microplate Reader	Tecan
Thermocycler	Biometra
Vortex	Sigma-Aldrich

Table 4: Chemicals and reagents

Item	**Source**
Trypan blue solution 0.4 %	Carl Roth
Ethanol	Carl Roth
2-Propanol	Carl Roth

70% Ethanol	Merck Millipore
PageRuler™ Prestained Protein Ladder	Thermo Scientific
Glycine	Carl Roth
N, N, N‘,N‘-Tetra-acetylethylenediamine (TEMED)	Carl Roth
Bromophenol Blue	Carl Roth
1,4-Dithiothreitol (DTT)	Carl Roth
Ammonium persulphate	Carl Roth
Sodium azide	Merck
Sodium chloride	Carl Roth
Sodium dodecylsulfate (SDS)	Carl Roth
Glycerol	Carl Roth
Tris(hydroxymethyl)-aminomethane (TRIS)	Carl Roth
TRIS hydrochloride	Carl Roth
Tween 20	PanReac AppliChem
Bovine serum albumin (BSA)	Carl Roth
SuperSignal West Pico PLUS Chemiluminescent Substrate	Thermo Scientific
Bacillol AF	Paul Hartmann
ROTIPHORESE®Gel 40 (29:1)	Carl Roth
Ponceau S	Sigma-Aldrich
Milk powder	
ROTI®Histofix (4 % Formaldehyd, pH 7)	Carl Roth
Cellmatrix Type I-A (Collagen, Type I, 3 mg/mL, pH 3.0)	Nitta Gelatin Inc.
Matrigel® Basement Membrane Matrix, Phenol Red-free, LDEV-free	Corning
Methyl cellulose, 4000 centipoises [cpi]	Sigma-Aldrich
CellTiter-Glo® 2.0 Cell Viability Assay	Promega
RIPA buffer (10X)	Cell Signaling
Phenylmethylsulfonyl fluoride (PMSF)	Carl Roth
Restore™ Western Blot Stripping Buffer	Thermo Scientific
RLT buffer	Qiagen

RW1 buffer	Qiagen
RNA Wash buffer	Zymo Research

Table 5: Recombinant proteins, inhibitors, and antibiotics

Secondary antibody	**Source**
Recombinant Human IFNγ	PeproTech
Recombinant Human TNFα	PeproTech
Recombinant Human IL17A	PeproTech
Recombinant Human $VEGF_{165}$	PeproTech
Recombinant Human CXCL1	PeproTech
Recombinant Human CXCL2	PeproTech
Recombinant Human CXCL5	PeproTech
Recombinant Human CXCL6	PeproTech
Recombinant Human CXCL8	PeproTech
SB225002	MedChemExpress
Sunitinib	MedChemExpress
TWS119	MedChemExpress
AR-A014418	MedChemExpress
LY2090314	MedChemExpress
CXCL5 Antibody	R&D
Bevacizumab	Roche
Puromycin	Cayman Chemical

Table 6: Commercial Kits

Kits	**Source**
Infinium Global Screening Array-24 v3.0 Kit	Illumina
Proteome Profiler Human Phospho-Kinase Array Kit	R&D
AllPrep DNA/RNA Micro Kit	Qiagen
Legendplex Human Proinflammatory Chemokine Panel 1	Biolegend

Legendplex Human Proinflammatory Chemokine Panel 2	Biolegend
Pierce™ BCA Protein Assay Kits	Thermo Scientific

Table 7: Expandable items

Item	**Source**
Cell Counting Slides for TC10/TC20 Cell Counter	Bio-rad
Cell culture flasks, with filter (T25, T75)	TPP
Cell culture flasks, with filter (T75, T175)	Sarstedt
Cell culture plates (6, 24, 96 wells/flat bottom)	TPP
Cell culture petri dishes	Sarstedt
PEHA-SOFT nitrile white gloves	Paul Hartmann
Screw top bottle DURAN® clear glasses	DWK Life Sciences
Serological pipettes (2, 5, 10, 25, 50 ml)	Sarstedt
Cell scraper	Sarstedt
Sterile filters (0.45 and 0.22 µm)	Diagonal
Tubes (15 ml, 50 ml)	Sarstedt
SafeSeal reaction tube (0.5, 1.5, 2, 5 ml)	Sarstedt
Amersham™ Protran® Western-Blotting-Membranes, Nitrocellulose, 0.45 µm pore size	Cytiva
Whatman Blotting paper	Whatman
Petri dish, square, with vents	Greiner bio-one
Feather disposable scalpels, figure 10	Pmfmedical
Leukopor	BSN medical
Sterican® 30G x 1/2"	BBraun
Surgical scissor	Carl Roth
Spatula	Carl Roth
Combitips® advanced (1, 2.5, 5, 10 ml)	Eppendorf
Histology cassettes	Kartell LABWARE
Biopsy filter paper	MEDITE Medical GmbH
Biopsy pads	VWR

Zymo-Spin IIICG columns	Zymo Research

Table 8: Buffers

Buffer	**Composition**	**Concentration**
Stacking gel buffer (Tris pH 6.8)	TRIS (121.1 g) fill up to 1 L with distilled water (adjust pH to 6.8 with 32% HCl)	1M
Resolving gel buffer (Tris pH 8.8)	TRIS (121.1 g) fill up to 1 L with distilled water (adjust pH to 8.8 with 32% HCl)	1M
10X SDS-PAGE running buffer	TRIS (30 g) Glycine (144g) SDS (10 g) fill up to 1 L with distilled water	250 mM 1920 mM 1%
10X TRIS-Glycine buffer	TRIS (30 g) Glycine (144 g) fill up to 1 L with distilled water	250 mM 1920 mM
1X Blotting buffer	10X TRIS-Glycine buffer 2-Propanol fill up to 2 L with distilled water	 15%
10X TBS	TRIS (5.6 g) TRIS-HCl (24 g) NaCl (88 g) fill up to 1 L with distilled water	50 mM 150 mM 1500 mM
1X TBST	10X TBS (100 ml) Tween-20 (500 µl) fill up to 1 L with distilled water	
4X Sample loading dye + DTT	SDS (2 g) TRIS-HCl pH 6.5 (5 ml) Glycerol (8 ml)	277 mM 0.2 M 4.3 M

	Bromphenol Blue (100 mg) Warm up to 37°C till SDS dissolves, then add DTT 1 M (10 ml) fill up to 25 mL with distilled water	6 mM 0.4 M
Sterile reconstitution buffer	$NaHCO_3$ (1.1 g) NaOH 1 M (2 mL) HEPES 1 M (10 mL) Ultrapure water (38 mL)	 0.05 N (0.05 M) 200 mM

Table 9: Primary antibodies for western blot

Primary antibody	**Source**
p44/42 MAPK (Erk1/2) Antibody #9102 (Isotype: Rabbit IgG)	Cell Signaling
Phospho-p44/42 MAPK (Erk1/2) (Thr202/Tyr204) mAb #4370 (Isotype: Rabbit IgG, clone: D13.14.4E)	Cell Signaling
Akt (pan) mAb #2920 (Isotype: Mouse IgG1, clone: 40D4)	Cell Signaling
Phospho-Akt (Ser473) mAb #4060 (Isotype: Rabbit IgG, clone: D9E)	Cell Signaling
Stat3 mAb #30835 (Isotype: Rabbit IgG, clone: D1B2J)	Cell Signaling
Phospho-Stat3 (Tyr705) XP® mAb #9145 (Isotype: Rabbit IgG, clone: D3A7)	Cell Signaling
c-Jun mAb #9165 (Isotype: Rabbit IgG, clone: 60A8)	Cell Signaling
Phospho-GSK-3β (Ser9) XP® mAb #5558 (Isotype: Rabbit IgG, clone: D85E12)	Cell Signaling
Phospho- GSK-3α/β (Ser21/Ser9) mAb #9331 (Isotype: Rabbit IgG, clone: D85E12)	Cell Signaling
Phospho-c-Jun (Ser63) mAb #2361	Cell Signaling

(Isotype: Rabbit IgG)	
GSK-3α/β mAb #5676 (Isotype: Rabbit IgG, clone: D75D3)	Cell Signaling
GAPDH mAb #2118 (Isotype: Rabbit, clone: 14C10)	Cell Signaling
β-actin mAb # A2228 (Isotype: Rabbit, clone: AC-74)	Sigma-Aldrich

Table 10: Secondary antibodies for western blot

Secondary antibody	**Source**
Peroxidase AffiniPure™ Goat Anti-Rabbit IgG (H+L) #111-035-003	Jackson Immunoresearch
Peroxidase AffiniPure™ Goat Anti-Mouse IgG + IgM (H+L) #115-035-044	Jackson Immunoresearch

Table 11: Software

Software	**Source**
R version 4.3.2/R studio version 2023.09.1+494	
LEGENDplex™ Data Analysis Software Suite	Biolegend
GraphPad Prism version 10.0	GraphPad Software Inc
ImageJ2 version 2.14.0/1.54f	
Image Lab version 6.1	BioRad

2.2. Methods

2.2.1. Cell culture

Adherent cancer cell lines were cultured in RPMI/DMEM medium supplemented with 10% heat-inactivated FBS, 2 mM L-Glutamine, and 1% Pen/Strep in a humidified incubator with 5% CO_2 at 37°C. Every three days, the cell flask was rinsed with DPBS and incubated with 1 mL of 0.25% trypsin-EDTA for 5 min to detach the cells. Next, 4 mL of R10+/D10+ medium was added to neutralize the trypsin solution. The cell suspension was centrifuged

at 300g for 5 min at RT. A part of the cell pellet was resuspended in prewarmed fresh medium and transferred into a new tissue culture flask.

HUVECs were cultured in endothelial cell proliferation medium (ECPM+) containing company-provided supplements in a humidified incubator with 5% CO_2 at 37°C. The flask was coated with 0.1% gelatin in DPBS for at least 15 min at 37°C, then the gelatin was removed. When the cell confluence reached 80%, the cell flask was rinsed with DPBS and incubated with 1 mL of accutase for 5 min to detach the cells. Next, 4 mL of ECPM+ was added to neutralize the accutase solution. The cell suspension was centrifuged at 200g for 5 min at RT. A part of the cell pellet was resuspended in prewarmed fresh medium and transferred into a new gelatin-coated culture flask.

To prepare 0.1% gelatin, 0.15 g gelatin was mixed with 150 mL DPBS, and was warmed up in a water bath to 50°C until obtaining clear solution. The solution was sterilely filtered using a 0.45 µm pore-size filter before use. DPBS-gelatin can be stored for up to 6 months at 4°C.

2.2.2. ccRCC conditioned-media collection, HUVEC proliferation and HUVEC stimulation

1 million 786O cells or 1.5 million Caki1 cells were plated in T75 flask overnight to allow cell attachment. The old media was removed and RPMI with glutamine and Pen/Strep (no FBS) or M199 with 10% FBS and Pen/Strep was added; the former was used for HUVEC stimulation, while the latter was used for HUVEC proliferation. Cells were incubated for 48 h. Culture supernatants were collected and filtered using a 0.45 µm pore-size filter, then frozen at −20°C until needed.

To perform ccRCC supernatant stimulation, HUVECs were seeded at 200,000 cells per well in 6-well plate and allowed to grow to roughly 85% confluence (usually within 3 to 4 days). HUVECs were starved in the endothelial cell proliferation base medium supplemented with the tested agents, SB225002 0.5 µM, CXCL5 antibody 5 µg/mL, sunitinib 100 nM, for 4 h and then stimulated with ccRCC CM containing the corresponding drugs for 20 min. As a negative control, cells were kept in ECPM base medium without the addition of drugs.

To conduct HUVEC proliferation, 2000 HUVEC cells were seeded in each well/96-well flat-bottom plate. The day after, the medium was discarded and replaced with ccRCC CM

serially diluted in fresh M199 base medium without or with the addition of SB225002 1 μM in technical duplicates. A similar experimental setup was used for HUVEC proliferation in undiluted ccRCC CM supplemented without or with either SB225002 1 μM, and/or sunitinib 0.1 μM, and/or bevacizumab 100 μg/mL, or VEGFA 25 ng/mL. After 3-day incubation, 50 μL CellTiter-Glo® 2.0 Reagent was added to each well. The plate was shaken for 2 min on a shaker and incubated for 10 min at RT in the dark. The plate was loaded to a microplate reader and the luminescent signal was recorded.

2.2.3. Enzyme-linked Immunosorbent Assay (ELISA)

100,000 786O cells and 130,000 Caki1 cells were plated per well in 12-well plate overnight to allow cell attachment. The old media was removed and RPMI with glutamine and Pen/Strep (no FBS) was added without or with either 250 U/mL IFNγ, or 250 U/mL TNFα, or 100 ng/mL IL17A. Cells were incubated for 48 h. Culture supernatants were collected and filtered using a 0.45 μm pore-size filter, then frozen at −20°C until needed.

To measure the concentrations of soluble CXCL6 that were secreted by ccRCC cells, we used the human CXCL6 ELISA kit from R&D following manufacturer's guidelines Absorbance was measured at 450 nm as the detection wavelength and 540 nm as the reference wavelength for the assay using TECAN microplate reader. The intensity of the color is proportional to the amount of CXCL6 present in the well. The absolute concentration of CXCL6 was calculated from the standard curve, which was generated using data reduction method of sigmoidal, 4 parameter logistic in GraphPad Prism.

2.2.4. Multiplex ELISA for soluble-factor measurement

To measure the concentrations of soluble chemokines that were secreted by ccRCC cells, we used Legendplex (Biolegend), a multiplex flow-cytometry-based immunoassay. The kits were stabilized at RT for 30 min before starting experiment. The assay buffer, wash buffer, serial-diluted standards, and mixed beads were prepared according to the manufacture's instruction. 10 μL assay buffer and 10 μL standard (from C7 to C0) were added in standard well in a V-bottom 96 well plate. In sample well, 15 μL assay buffer and 5 μL supernatant were pipetted to achieve the dilution of 1:2. 10 μL mixed beads were vortex for one minute before adding to each well. The plate was sealed and covered with aluminum foil to protect from light, and was shaken at 800 rpm overnight at 4°C. Next day,

200 µL of wash buffer was added per well and the plate was centrifuged at 1050 g for 5 min. After the centrifugation, the blue bead pellet can be seen. The fluid was discarded in 1 continuous and forceful motion, then the beads were resuspended by tapping against the plate edge with a pen. 10 µL detection antibodies were pipetted per well. The plate was sealed and covered with aluminum foil, and was shaken at 800 rpm for 1 h at RT. Subsequently, 10 µL SA-PE was added per well without any washing. The plate was again shaken at 800 rpm for 30 min at RT. The plate was washed 2 times with 200 µL wash buffer per well. Finally, 150 µL wash buffer was added per well, then the plate was sealed, wrapped in aluminum foil, and stored at 4°C until acquisition. Samples were read in the Cytek Aurora. 3000 beads per sample were acquired. The analysis was performed using the LEGENDplex™ Data Analysis Software Suite.

2.2.5. Western blotting

Cells were washed 1 time with DPBS and 60 µL of RIPA buffer supplemented with 1 nM PMSF in EtOH per well in 6-well plate. Cell lysate was gently harvested using cell scarper and centrifuged for 10 min at 14,000g at 4°C. The clear supernatant was transferred into new tubes.

Protein concentration was measured using BCA Protein Assay kit. 3.33 µL of cell lysate was diluted in 63.3 µL RIPA buffer, and 30 µL of the diluted lysate was pipetted into a well/96-well plate. The standards were prepared in triplicates according to manufacture ’s protocol. The working solution was prepared by diluting 1 part of BCA reagent B in 50 parts of BCA reagent A. 200 µL of working solution was added to each well (containing either standard or sample). The plate was sealed with a plastic film and incubated at 37°C in 1 h. The absorbance was measured at 562 nm wave length in a microplate reader.

Protein amount loaded per lane was calculated to have 10 to 25 µg protein in the final volume of 26 µl containing loading dye. Next, proteins were denatured at 95°C for 5 min. Protein ladder and samples were loaded on a 10% SDS PAGE gel. First gels were run at 100 V for 15 min, and then voltage was increased to 140 V for 75 min. A wet blotting system and blotting buffer containing 15% (v/v) isopropanol were used. Proteins were transferred onto a 0.45 µm pore size nitrocellulose membrane at 100 V for 1.5 h.

Ponceau S staining was performed to check for bubbles or any blotting problems. Membranes were then blocked in 5% (w/v) milk powder in TBST for 1 h at RT, and washed

1 time with TBST before primary antibodies were added. Primary antibody was diluted in 5% (w/v) BSA and 0.02% (w/v) sodium azide. The membranes were incubated overnight at 4°C. Next day, the membranes were washed 2 times for 5 min each with TBST, following by the addition of secondary antibody diluted (1:5000 dilution) in 5% (w/v) milk powder in TBST. After 1 h incubation at RT, the membranes were washed 1 time with TBST and 1 time with TBS. Chemiluminescent substrate was applied to the membrane for 1 minute and the chemiluminescent signals were capture using ChemiDoc MP Imaging System. Signal transduction protein and its corresponding phosphorylated form were detected in 2 different membranes; if the detection was performed on the same membrane, the phosphorylated form was detected first, then the membrane was stripped and with stripping buffer and re-probed with primary antibody binding specifically to total form. Data analysis was performed using Image Lab software.

2.2.6. Spheroid sprouting assay

At day 1, HUVECs were harvested and counted. Each spheroid contained 500 HUVECs and each collagen gel (500 µL) should have at least 48 spheroids. To prepare 4 spheroid-embedded gels, 100,000 HUVECs were resuspended in methocel-ECPM solution with 2,5% FCS, made by mixing 1mL methocel stock solution with 2.75 ml ECPM basal medium and 1.25 ml ECPM+ (20% methocel stock solution, 55% ECPM basal, 25% ECPM+). Hanging drops were generated by pipetting 25 µL of this mixture per drop on a 12 cm square petri dish lid using multi-channel pipette and attentively turning over plastic lid. The dishes were incubated overnight at 37°C in the incubator.

The next day, the spheroids were checked for evenly rounded and uniform formation under microscope. The spheroids were collected with 3.5 mL 10% FBS in PBS for each petri dish with 10 mL pipette and transferred them into the 15 mL tubes. The plate can be washed 1 time with 5 mL 10% FBS in PBS. The spheroids were centrifuged at 100g for 5 min at 25°C. The supernatant was aspirated and the pellet was gently overlay with 1 mL FBS-methocel solution (20% FBS, 80% methocel stock solution). Meanwhile, the following ice-cold reagents—Cellmatrix Type I-A, M199 10X medium, and sterile reconstitution buffer—were mixed in this specific order at an 8:1:0.25 ratio to make up the neutralized collagen solution. Then 1 mL of this collagen solution was fast and carefully combined to avoid bubbles with the 1 ml spheroid containing methocel solution prepared previously.

Homogenous mixing of all components was indispensable for a clear matrix formation and for the homogenous distribution of the spheroids inside the gels. In a prewarmed 24-well plate, 500 µL of the methocel-spheroid-collagen mixture was dispensed in each well. The plate was immediately placed in the incubator for rapid polymerization to impede the sinking of the spheroids to the bottom of the wells. After 30-minute incubation, the collagen gels were overlaid with 125 µl ccRCC CM or ECPM base medium supplemented with 25 ng/mL VEGFA. After 24h incubation, 500 µL PFA 10% was added to stop the assay. The plates can be stored for up to 4 weeks at 4°C.

For quantitative analysis, 6 spheroids were randomly picked for each tested condition and the pictures were taken in phase-contrast microscope at 10X magnification. The pictures were analyzed using NeuronJ, a plug-in of ImageJ (Yetkin-Arik et al., 2019) to quantify the cumulative sprout length, defined as the total length of all the sprouts stemming from 1 spheroid, and the number of sprouts.

To prepare methocel stock solution, 1.5 g methyl cellulose powder was autoclaved in a 250 ml glass bottle containing a clean magnetic fish. The autoclaved methyl cellulose was dissolved in 62.5 mL preheated ECPM basal medium (60°C) for 20 min using the magnetic stirrer. An equal volume of ECPM basal medium (at RT) was added to the clear solution and centrifuged at 2000g for 1 h at RT. The finished solution can be stored up to 1 year at 4°C.

To collect the ccRCC CM for sprouting assay, 50,000 ccRCC cells were plated per well in 12-well plate overnight. Next day, the old medium was removed and RPMI base medium was added. The cells were incubated at 37°C for 6 h and the medium was collected and stored at -20°C.

2.2.7. Chicken chorioallantoic membrane (CAM) assay and drug treatment

Lohmann brown eggs from Lohmann Deutschland hatchery were carefully dry wiped with paper towels to remove any dirt, feathers and excrement from the eggshells. The survival rate of the chicken embryos can be considerably reduced by wiping the eggs with 70% ethanol or any other cleaning solutions, even distilled autoclaved water. The eggs were placed horizontally in the incubator at 37.8°C, and 60% humidity. Day 0 of chicken embryonic development (ED) is defined as the first day of egg incubation.

At ED7, the eggs were opened under laminar airflow. The eggs were placed in the plastic rack with bigger tip (containing air sac) facing upwards. A hole of 2 cm^2 was introduced on the eggshell at this bigger tip with a sterile sharp-pointed surgical scissors, which were cleaned regularly in between with bacillol. Beneath the egg shell is a shell membrane. This membrane was damped with 500 µl DPBS, then was carefully removed using a tweezers to expose the CAM underneath. The interrupted blood vessels indicated dead embryos. All non-fertilized eggs or dead embryos were removed. The window was covered with parafilm to prevent the embryos from drying and dying in the incubator.

At ED8, tumor cells were harvested and pelleted. The required amount of cancer cells per egg was 2 to 3 million embedded in 25 µl Matrigel. Due to the high rate of xenograft rejection and embryo premature death, at least 6 eggs per condition were included for each experiment. The total amount of needed cells was calculated; the cells was mixed with the appropriate volume of Matrigel in 15ml tube and was kept on melting ice. Under the laminar airflow, the parafilm was discarded. The CAM area was gently scratched using a sterile 30 gauge cannula near the 'Y bifurcation' of blood vessels. Small hemorrhages were expected. The tumor Matrigel mixture were seeded by pipetting directly onto the scratched area. The eggs were labeled with important information including egg number, cell line, and treatment. Parafilm was used to seal the egg window. The eggs were immediately put back to the incubator to allow Matrigel polymerization. 48h post-engraftment, a 10 mm silicon ring encircled tumor was added, and the embryos were topically treated with 100 µl of CXCL5 antibody 20 µg/mL or SB225002 20 µM or sunitinib 10 µM or combination of these reagents or DPBS as negative control. Cancer cells were pretreated with the aforementioned drugs before engraftment at ED8, then they received the same treatment at ED10.

The experiment was terminated at ED14. The egg window was enlarged and pictures of tumors were taken at 2X zoom factor using a stereo microscope. Next, the tumor and surrounded CAM were excised attentively avoiding the detachment of the tumor from the CAM beneath. Tumor's width, length, and thickness were measured using a caliper. The harvested tissues were wrapped in wet filter paper and placed inside a histology cassette filled with biopsy pad. The tumor cassettes were put in a labeled container with 4% paraformaldehyde overnight for fixing. Next day, the cassettes were washed 3 times with distilled water, and stored in 70% EtOH for later immunohistochemistry staining.

The volumes of the excised tumors were estimated using the following formula:
V = 4/3 x π x ((width/2) x (length/2) x (thickness/2)).

2.2.8. Human phospho-kinase array

After HUVECs were stimulated with Caki1 Px459 supernatant (refer methods section 2.2.2), HUVECs were lysed with RIPA buffer and protein concentration was determined with BCA kit (refer methods section 2.2.5). HUVECs starved in ECPM basal medium was included as negative control. Phosphorylation status of multiple signal transduction proteins were determined using Proteome Profiler Human Phospho-Kinase Array Kit followed the instruction manual. Chemiluminescent signal was detected in ChemiDoc MP Imaging System under signal accumulation mode. The pictures were taken every 60 sec in 10 min. Protein Array Analyzer plug-in of ImageJ was employed for data analysis. The average intensity (pixel density) of duplicate dots was recorded and normalized to the mean intensity of reference dots. The relative changes in phosphorylated signals were decided between Caki1-treated and untreated HUVECs.

2.2.9. Clinical cohort

For N = 399 clear cell renal cell carcinoma from TCGA (TCGA-KIRC), *PBRM1* mutations, mRNA expression data (RNASeqV2, RSEM normalized values) of *CXCL1, CXCL2, CXCL3, CXCL5, CXCL6, PPBP,* and *CXCL8,* as well as clinical information were queried and downloaded from cBioPortal (https://www.cbioportal.org).

2.2.10. Bulk 3’mRNA sequencing

After 48-h treatment, kidney cancer cells were washed one time with PBS and 350 µl Qiagen RLT buffer plus 350 µl 70% EtOH were added to each well in 6-well plate. The mixture was loaded onto Zymo-Spin IIICG columns and centrifuged for 1 min at 10,000 rpm. The flow through liquid was discarded and 350 µl Qiagen RW1 buffer was added. Centrifugation was repeated and the flow through was discarded. 500 µl Zymo RNA Wash buffer was added and centrifuged 2 times for 1 min at 10,000 rpm to completely dry the columns. RNA-free water was pipetted on columns, incubated for 1 min, then centrifuged for 1 min at 10,000 rpm. The RNA samples were stored at -80°C.

Size distribution and the integrity of RNA library was determined by the RNA Screen Tape analysis prior to 3´mRNA-Seq library preparation utilizing the forward QuantSeq 3´mRNA-Seq Library Prep Kit for Illumina according to the manufacturer's protocol by the NGS Core Facility at the University Hospital Bonn. The pooled libraries were loaded in the Illumina HiSeq2500 platform for 100 base-pairs, single ended sequencing. The coverage was 10 million reads on average. Computational analyses were performed using the R/Bioconductor computing environment. Full genomic sequences for Homo sapiens from the R package BSgenome.Hsapiens.UCSC.hg38 (Team-TBD, 2023) was employed to build reference genome using 'buildindex' function from the RSubread package (Liao et al., 2013). FASTQ files were aligned to previously indexing hg38 reference using 'align' function from the same package. The package can quantifiy gene expression at the level of either exons, exon junctions or genes. The alignment procedure was executed without trimming and with 'uniquely mapped reads' argument set to false, allowing for mismatches in the initial cycles and multiple location mapping. The 'featureCounts' function (Liao et al., 2014) was used with 'useMetaFeatures' argument set to true to get count matrices at gene level using genomic annotations GRCh38 from the Genome Reference Consortium release 108.

For differential gene expression (DEG) analysis, package DESeq2 was utilized (Love et al., 2014). DESeq2 normalized raw counts using size factors to adjust for differences in library sizes and library composition, following by fitting generalized linear model for each gene, and performing Wald-test for statistical significance. Only genes with at least 10 reads in total were included in the analysis. P-value for each gene was corrected for multiple testing using Benjamini & Hochberg (B&H) method (false discovery rate, FDR). Genes with adjusted p values <0.05 were considered differentially expressed.

To get mRNA expression values for a particular gene, gene count matrices were processed in one of two ways. Specifically, the 'filterByExpr' function of the edgeR package (Robinson et al., 2010) was first applied on the count matrices to remove genes with low counts. Then 'voom' function of the limma package (Ritchie et al., 2015) were employed to generate $\log_2$ values of read counts per million ($\log_2$ CPM) by normalizing and transforming the raw count data. On the other hand, the count data was first processed by DESeq2 as described above, followed by 'regularized log' transformation ('rlog' function from the same package) to obtain the $\log_2$ values of mRNA expression.

Volcano plots were acquired using the R package EnhancedVolcano (Blighe et al., 2023). Heatmaps were generated using the R package ComplexHeatmap (Gu et al., 2016). The other plots were created using the R package ggplot2 (Wickham, 2016) and statistical significances were calculated using the R packages ggsignif (Ahlmann-Eltze & Patil, 2022) and ggpubr (Kassambara, 2023). Gene set enrichment analysis (GSEA) were computed for the Hallmark gene sets from the Molecular Signatures Database (MSigDB version 7.5.1) (Subramanian et al., 2005) using the R/Bioconductor package clusterProfiler (Yu et al., 2012). 'clusterProfiler' was also used for genome wide annotation of human genes.

2.2.11. Statistical analysis

Statistical analysis was performed using R (Version 4.3.0), R Studio (Version 2023.03.1 1 446), and GraphPad Prism (Version 9.4.0). Continuous variables were summarized by their medians, interquartile ranges (IQR), and ranges. Categorical variables were summarized by their percentages. Statistical tests were used including parametric two-tailed student's t-test, parametric one-way Analysis of variance (ANOVA), parametric two-way ANOVA, mixed-effects analysis, Kruskal-Wallis Test, Wilcoxon rank-sum test and log-rank test with different multiple comparison tests (Dunnett or Šidák) to obtain adjusted p-values if needed. Significance level of $p < 0.05$ was used to determine statistical significance. Statistical tests are specified in corresponding legends of the figures.

The prognostic value of *CXCL5* mRNA expression for ccRCC patient outcomes was assessed by comparing PFS, disease-specific survival (DSS), and OS between *CXCL5*-high and *CXCL5*-low tumors stratified by the median of *CXCL5* expression. To evaluate the survival distribution of ccRCC patients according to the *CXCL5* level of the tumors, univariable Kaplan-Meier methodology were performed, and significance was determined using the log-rank test, which were performed using the R package survival and survminer (Kassambara et al., 2021; Therneau, 2024; Therneau & Grambsch, 2013). Multivariate Cox regression analyses were conducted to compare the prognostic value of *CXCL5* transcriptional expression with baseline patient characteristics (age, sex), the presence of *PBRM1* mutation, and the American Joint Committee on Cancer (AJCC) staging in relation to PFS and OS. Adjusted hazard ratios (HR) with their 95% confidence intervals were described.

3. Results

3.1. Pharmacologically targeted multiple subunits of the mammalian SWItch/Sucrose Non-Fermentable (SWI/SNF) complexes

SWI/SNF complexes function as chromatin remodelers, which are evolutionary conserved across *Saccharomyces cerevisiae, Drosophila melanogaster,* and *Homo sapiens* (Tang et al., 2010). Combinatorial assemblies of 15 subunits compose three distinct forms of SWI/SNF complexes, BRG1-associated factors (BAFs), Polybromo-associated BAFs (PBAFs), and non-canonical BAFs (ncBAFs) (**Figure 3.1.A**). These three entities are distinct not only in terms of composition but also in terms of localization on chromatin and functions (Michel et al., 2018). Mutations in one or several subunits of the SWI/SNF complexes are collectively found in nearly 20% across multitudes of cancer types (Shain & Pollack, 2013). There are five components in SWI/SNF complexes which possess modules that can interact with acetylated lysine residues on histone, namely bromodomains (**Figure 3.1.B**). Specifically, SMARCA2 (also known as hBRM—human Brahma, or BAF190B, or SNF2L2) and SMARCA4 (also known as BRG1—Brahma-related Gene 1, or BAF190A), which function as helicases and ATPases providing energy for whole complexes, are core members that exist in all three SWI/SNF complexes. While BRD9 is a component of ncBAFs, its paralog BRD7 and PBRM1 constitute parts of PBAFs. Here, we used multiple pharmacological compounds to disrupt the binding of the SWI/SNF bromodomains, with the focus on PBRM1, to theirs targets and investigated changes in the transcriptomic profile of ccRCC cells.

All compounds used in this part were provided by Prof. Dr. Stefan Knapp (Institute of Pharmaceutical Chemistry, Goethe University, Frankfurt, Germany) (**Figure 3.2**). Detailed characteristics of the pan-SMARCA/PBRM1 inhibitors and their pharmacological activities on murine adipocytes were published previously (Wanior et al., 2020); MW96, MW99, MW264—negative control (**Figure 3.2.A**), DP23, and DP28 (**Figure 3.2.B**) in our study corresponded to compounds 22, 23, 35, R-28, and 32 in Wanior's article. All previously mentioned chemical probes inactivated SMARCA2/4 and the 5th bromodomain of PBRM1 (PB1(5)), while DP23 and DP28 auxiliary repressed the 2nd and 3rd bromodomains of PBRM1 (PB1(2,3)). dBRD9, a BRD9 chemical degrader or proteolysis targeting chimera (PROTAC) (**Figure 3.2.C**), was thoroughly studied by Remillard and colleagues

(Remillard et al., 2017). Structures, pharmacokinetics and survival benefits in AML mouse models of the BRD7/9 inhibitors (BI-7273, BI-9564, and BI-6354—negative control (**Figure 3.2.D**)) were previously described by Martin et al. (Martin et al., 2016).

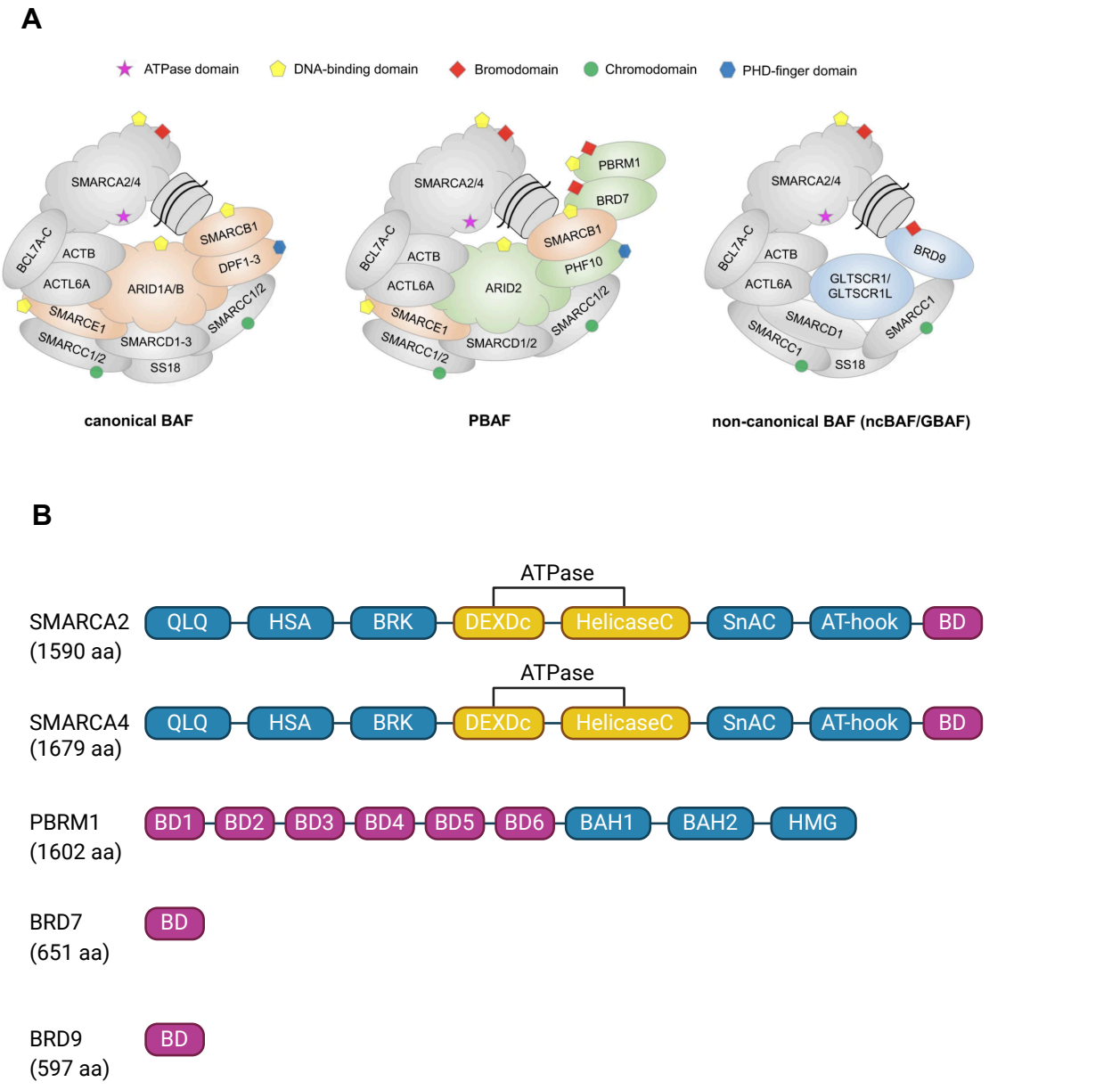

Figure 3.1: Schematic structures of mammalian SWI/SNF complexes and protein domains of SWI/SNF subunits possessing bromodomains. (A) The mammalian SWI/SNF complexes are found in three non-redundant forms. (B) SMARCA2/4 and BRD7/9 have only one bromodomain in their structure, while PBRM1 possesses 6 bromodomains. BAF, BRG1/BRM-associated factor; BAH, bromo-adjacent homology; BD, bromodomain; BRK, Brahma and Kismet domain; DEXDc, DEAD-like helicases superfamily domain; HAS, helicase SANT-associated domain; HelicaseC, helicase superfamily c-terminal domain; HMG, high-mobility group; QLQ, QLQ protein interaction domain; SnAC, SNF2 ATP-coupling. Adapted from (Sadek et al., 2022; Wanior et al., 2021; Zaware & Zhou, 2019).

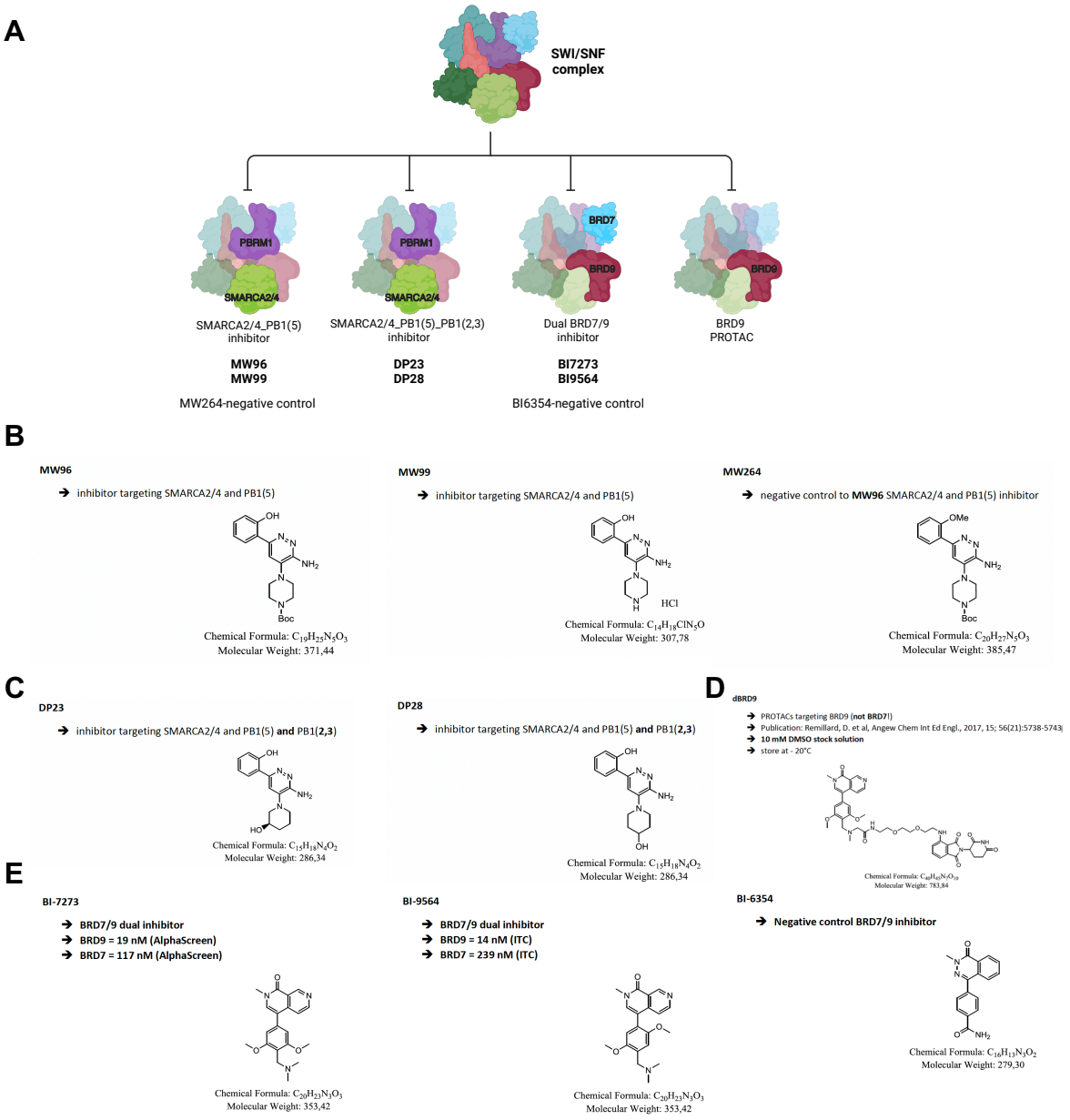

Figure 3.2: Chemical structures of agents that suppress diverse SWI/SNF bromodomains including SMARCA2/4, PBRM1, BRD7, and BRD9 with their corresponding negative controls. (A) Schematic representation of mammalian SWI/SNF complexes illustrating bromodomain-contained subunits that are inhibited by four corresponding drug groups. (B) SMARCA2/4_PB1(5) inhibitors and matched vehicle control. (C) SMARCA2/4_PB(5)_PB1(2,3) inhibitors. (D) PROTAC targeting BRD9. (E) Dual BRD7/9 inhibitors and matched vehicle control.

Caki-1 cells were incubated with the aforementioned agents in serial dilutions: 1 µM, 5 µM, and 10 µM for 48 h. Of note, *VHL, PBRM1* and *HIF1A* are intact in Caki1 (Raval et al., 2005; Tsherniak et al., 2017). The experiment was done by PD. Dr. Niklas Klümper. As a first step towards understanding cellular responses to the disruption of bromodomain binding activity in ccRCC cells, we performed 3'-RNA sequencing on vehicle and drug-treated Caki1 cells, then conducted clustering and pairwise comparisons for differential gene expressions (DEGs), which the data was subdivided into the following four conditions: 1/SMARCA2/4_PB1(5) inhibitor, 2/SMARCA2/4_PB1(5)_PB1(2,3) inhibitor, 3/Dual BRD7/9 inhibitor, 4/BRD9 degrader**.** This transcriptomic-based screening approach using pharmacological inhibition compounds in human cell culture model is cost-effective, time-efficient, and feasible to identify the downstream consequences concerning PBRM1 inactivation. Cell cultures treated with two disparate agents from the same drug-class clustered together, revealing a close genetic similarity within their group except for the BRD9 PROTAC (**Figure 3.3.A**). For pan-SMARCA2/4 and PBRM1 groups, control samples were discriminated from treated samples on the first principal component (PC1) of principal component analysis (PCA) (**Figure 3.3.B**). In contrast, there was no clear separation between untreated/vehicle and treated with BRD7/9 inhibitor or BRD9 degrader.

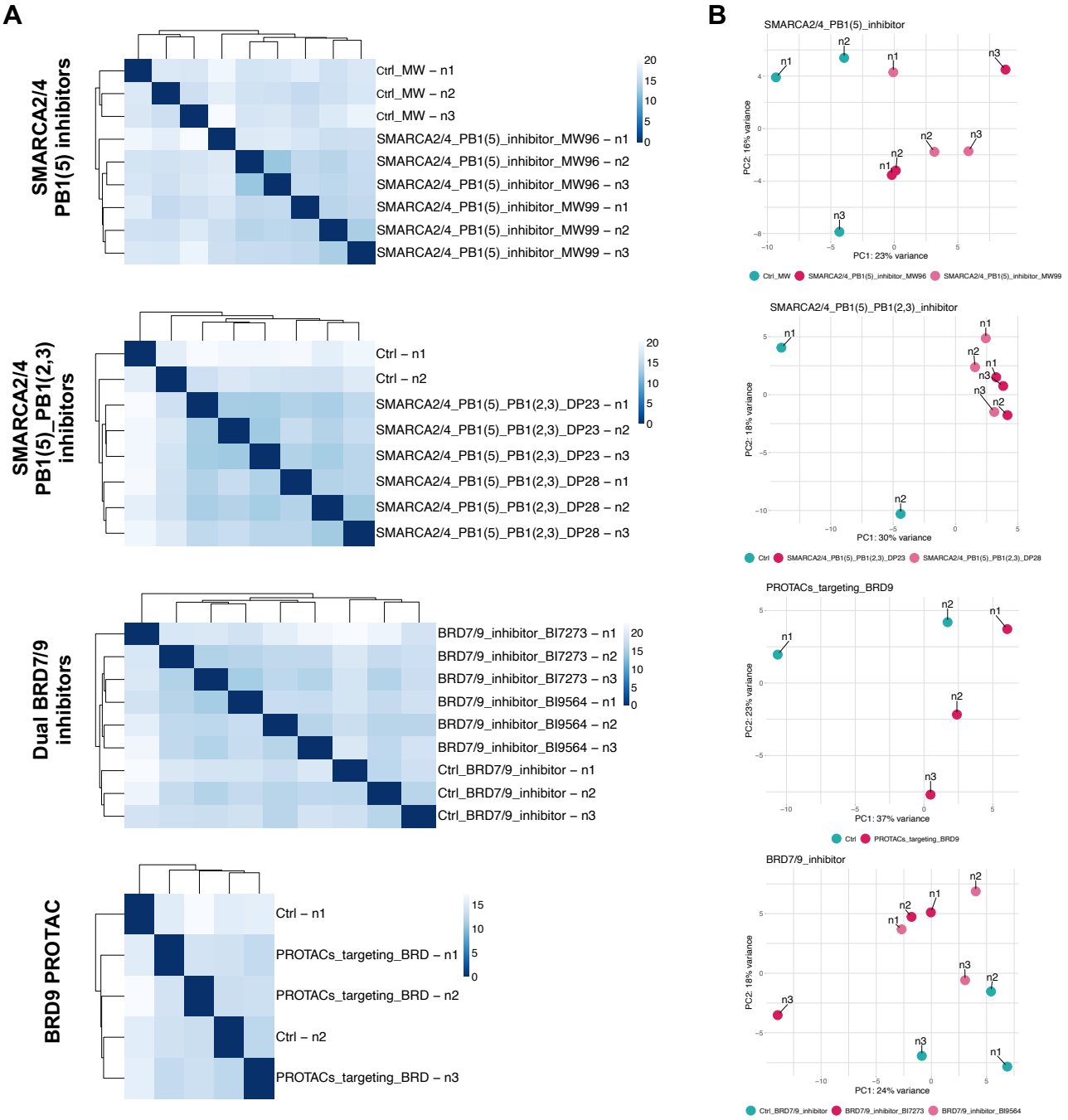

Figure 3.3: Caki1 cells treated with the various drugs targeting different bromodomains of mammalian SWI/SNF complexes at different concentrations exhibits consistency in mRNA expression profiles within their drug class, and the predominant source of variations is between the tested drugs that inactivated different SWI/SNF subunits and vehicle controls. (A) Clustering heatmaps were generated by calculating the Euclidean distances between samples in four different drug classes. (B) Principal component analysis (PCA) plots demonstrate the extent of intra-group homogeneity and the prominent source of data variability. The results from DESeq2 analysis followed by rlog transformation were used to draw these plots. Three samples per inhibitor, which represented cells treated with the same drugs at three different concentrations, were included in the analysis.

Caki1 cells treated with negative compounds (negative controls of SMARCA2/4_PB1(5) and dual BRD7/9 inhibitors) showed no differences in comparison with DMSO-treated cells (**Figure 3.4.A**). The expression of 91 and 54 genes were significantly (adjusted p-value < 0.05 after Benjamini-Hochberg (BH) correction) dysregulated in response to inactivation of SMARCA2/4 and PB1(5) by MW96 and MW99, respectively, compared to their corresponding control (**Figure 3.4.B**). The largest effect on gene expressions, 476 and 263 genes, was from DP23 and DP28 treatments respectively (**Figure 3.4.C**). In regards to BRD9 and/or BRD7 inhibitors, the number of significantly DEGs were as follows: 119 genes for BI-72373, 31 genes for BI-9564, and 12 genes for dBRD9 (**Figure 3.4.D-E**). Hierarchical clustering of genes that had p-adjusted values <0.05 and $|\log_2 FC|>0.5$ showed a high similarity of gene expression profiles between agents from the same drug class (between MW96 and MW99, and between DP23 and DP28) (**Figure 3.5.A-B**). The significantly altered genes in SMARCA2/4_PB1(5) group included genes involved in RNA synthesis (*C15orf18, C1orf109*) and the regulation of gene expression (*HMGA2, FOS*—proto-oncogene, *TFAP2A, HES1, NR2F2, SETPB1, AKR1C1, AKR1C2, AKR1C3*—aldo-keto reductase superfamily). The greatest degree of differential expression was noted in SMARCA2/4_PB1(5) PB1(2,3) group (**Figure 3.5.B**) with differently expressed genes coding for transcription factors (*IER2, ELF3*), histones (H4C3, H4C15), and signaling proteins (RHOC, GPRC5A, SRC—proto-oncogene). Few genes were differentially expressed when comparing BI-9654 to the control, and dBRD9 to the control groups (**Figure 3.5.C-D**).

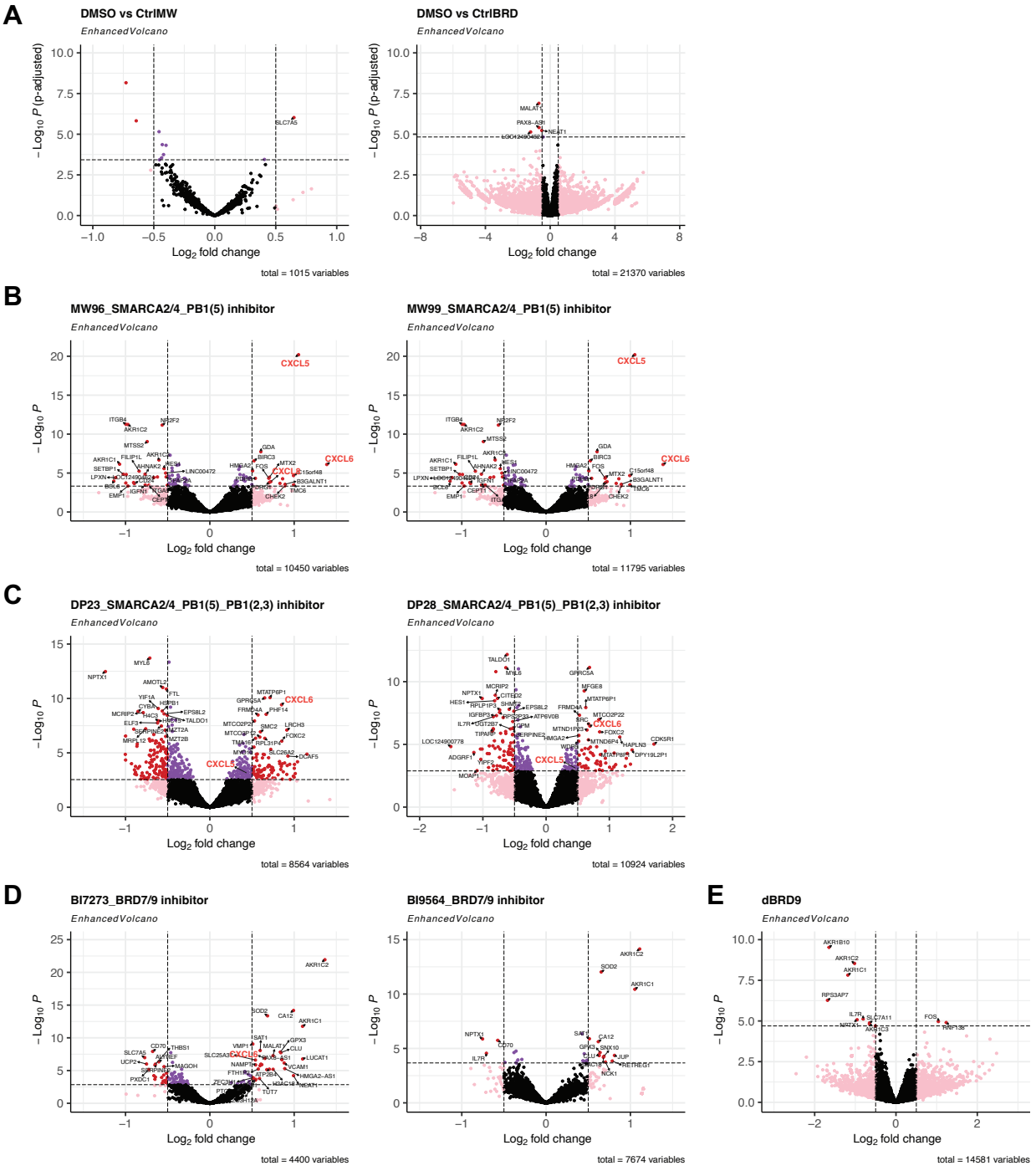

Figure 3.4: Gene expression changes upon acute (48 hours) suppression of different SWI/SNF bromodomains in Caki1 cells. (A-E) Volcano plots depict the DEGs between the specific inhibitor and its corresponding control. The vertical and horizontal dashed lines exhibit p-adjusted values = 0.05 and $\log_2$ fold change of -0.5 and 0.5. The purple dots and red dots represent genes with statistically significant alterations within and above $\log_2$ fold change of -0.5 and 0.5, respectively.

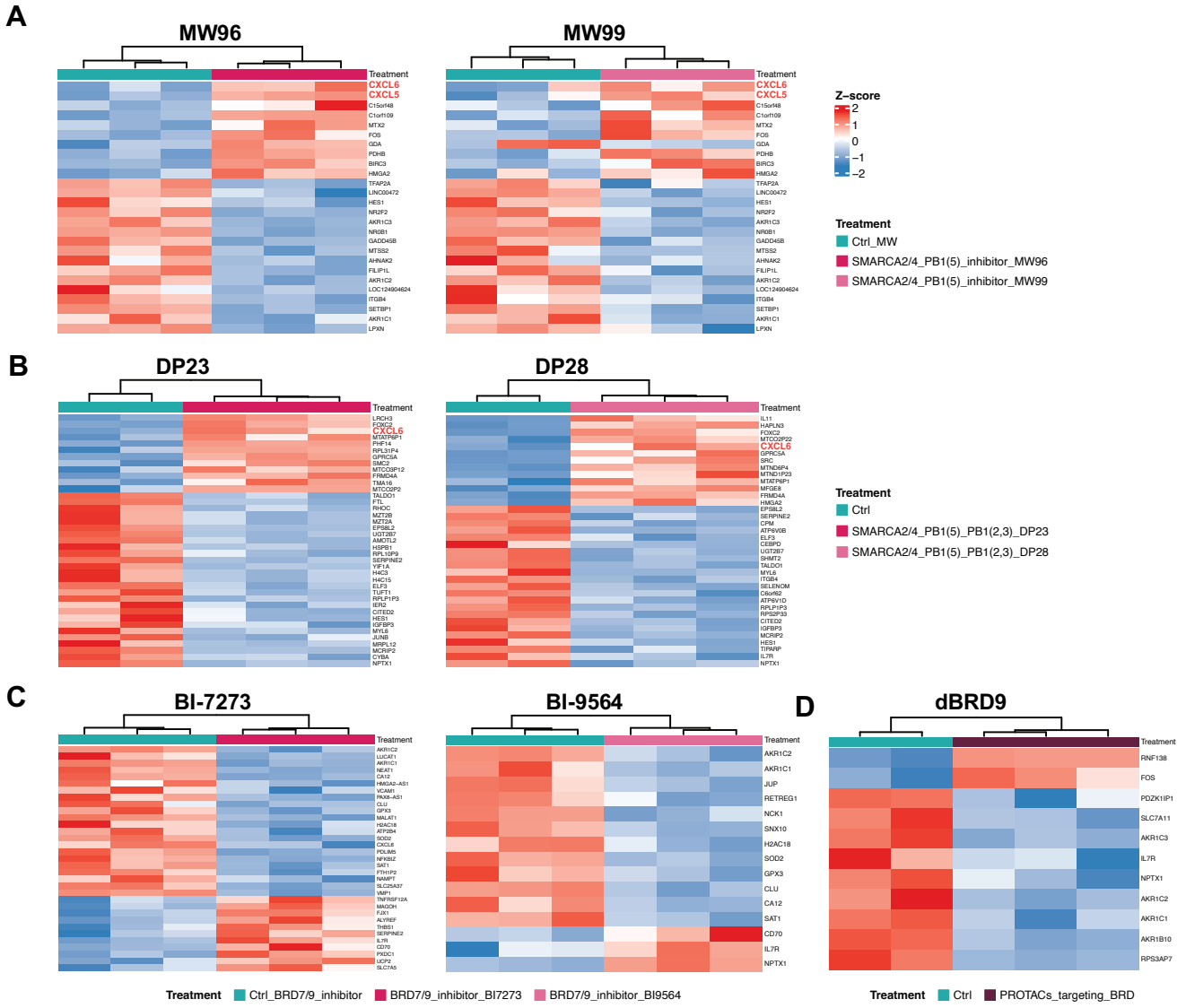

Figure 3.5: Top 50 significantly dysregulated genes in response to the pharmacological inhibition of the SWI/SNF bromodomains. Heatmaps of DEGs demonstrate hierarchical clustering results of the comparisons between bromodomain-inactivated drugs and vehicle controls, which rlog gene expression values of genes with p-adjusted values (FDR) <0.05 and $\log_2$FC > 0.5 were centered and scaled to get z-score. Z-scores are colored according to upregulation (red) or downregulation (blue).

Interestingly, *CXCL5* and *CXCL6* were uniformly increased gene expression in groups treated with the pan-SMARCA/PBRM1 inhibitors, but not with the BRD7 and/or BRD9 inhibitors, as shown in **Table 12** and **Figure 3.5**. Both CXCL5 and CXCL6 bind to the same CXCR2 receptor and belong to chemokine superfamily that plays a predominant role in mediating leukocyte recruitment to the inflammation sites as well as secondary lymphoid organs. In addition to the original chemotaxis function, all CXCR2 ligands—CXCL1, CXCL2, CXCL3, CXCL5, CXCL6, CXCL7, and CXCL8—possess angiogenic properties that can modulate the migration of human lung microvascular endothelial cells (HMVEC-L) and induce neovascularization in the corneal micropocket assay (Addison et al., 2000). Thus, we carefully examined the mRNA expression levels of all chemokines binding to CXCR2 in our sequencing dataset. Because the gene expression profiles of DMSO-treated and negative control MW groups were approximately the same (Figure 3.4A), we combined these two groups in performing statistical test to increase statistical power. As shown in **Figure 3.6**, *PPBP* (encoded CXCL7) mRNA was not detected, and *CXCL5* was significantly upregulated in groups in which the activity of pan-SMARCA/PBRM1 was disrupted, but not in the BRD9 and/or BRD7 treated groups. Inhibition of PBRM1 also leads to the upregulation of *CXCL1* and *CXCL8*, but this did not hold true for all the compounds in the pan-SMARCA/PBRM1 inhibitor groups.

Table 12: Inhibition of SMARCA2/4 and PBRM1 induced differentially expression of *CXCL5* and *CXCL6* in Caki1 cells

	CXCL5		***CXCL6***	
	log_2 FC	P-adjusted	log_2 FC	P-adjusted
SMARCA2/4_PB1(5)				
MW96	1.0522166	< 0.00001	1.3873594	< 0.001
MW99	1.0522166	< 0.00001	1.3873594	< 0.001
SMARCA2/4_PB1(5)_ PB1(2,3)				
DP23	0.4390678757	0.02373	0.8508951773	< 0.00001
DP28	0.449205748	< 0.001	0.693614372	< 0.00001

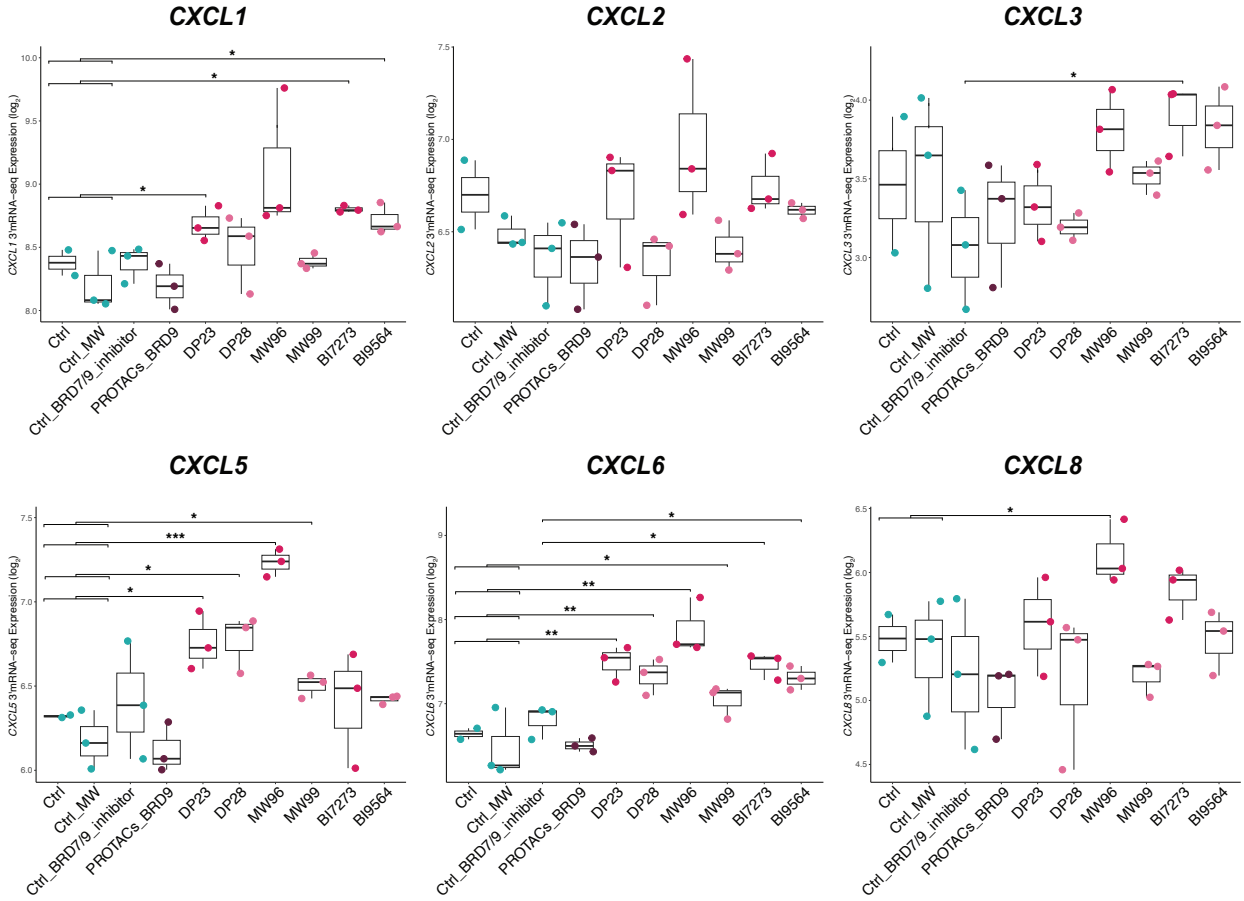

Figure 3.6: Pro-angiogenic chemokine profiles at the transcriptomic level of Caki1 cells when incubated for 48 h with various inhibitors that specifically inactivated disparate bromodomains of the SWI/SNF complexes. The depicted mRNA expression values are log_2 values of read counts per million (log_2 CPM) resulted from the normalization and transformation of raw count data using 'voom' function of the 'limma' package. Regarding the boxplots, the upper and lower hinges represent the 75th and 25th percentiles, respectively and the middle line denotes median. The whiskers extend in both directions until reaching the max or min value. Data were analyzed by two-sided t-test using 'stat_signif' function of the 'ggsignif' package in R and *p < 0.05, **p < 0.01, and NS. not significant represent statistical significances.

3.2. The association between *PBRM1*-loss-of-function and *CXCL5* in TCGA-KIRC dataset

Given our results of RNA sequencing and the aforementioned relationship between *PBRM1* mutations and angiogenesis, we investigated the correlation between the expression of pro-angiogenic CXCR2-binding chemokines and the *PBRM1*-mutated status in ccRCC tumors. Therefore, the TCGA-KIRC kidney renal clear cell carcinoma dataset of *PBRM1* mutations, mRNA expression levels of *CXCL1, CXCL2, CXCL3, CXCL5, CXCL6, PPBP,* and *CXCL8,* as well as clinical information was downloaded from cBioPortal. Mutations of *PBRM1* were identified in 143 (35.8%) patients out of 399 patients. Transcriptional expressions of *CXCL1, CXCL2, CXCL3,* and *CXCL5* were significantly elevated in *PBRM1*-loss tumors (**Figure 3.7**). In contrast to the observation from our RNA-seq data, there was no difference in *CXCL6* mRNA levels between mutated and non-mutated *PBRM1* groups.

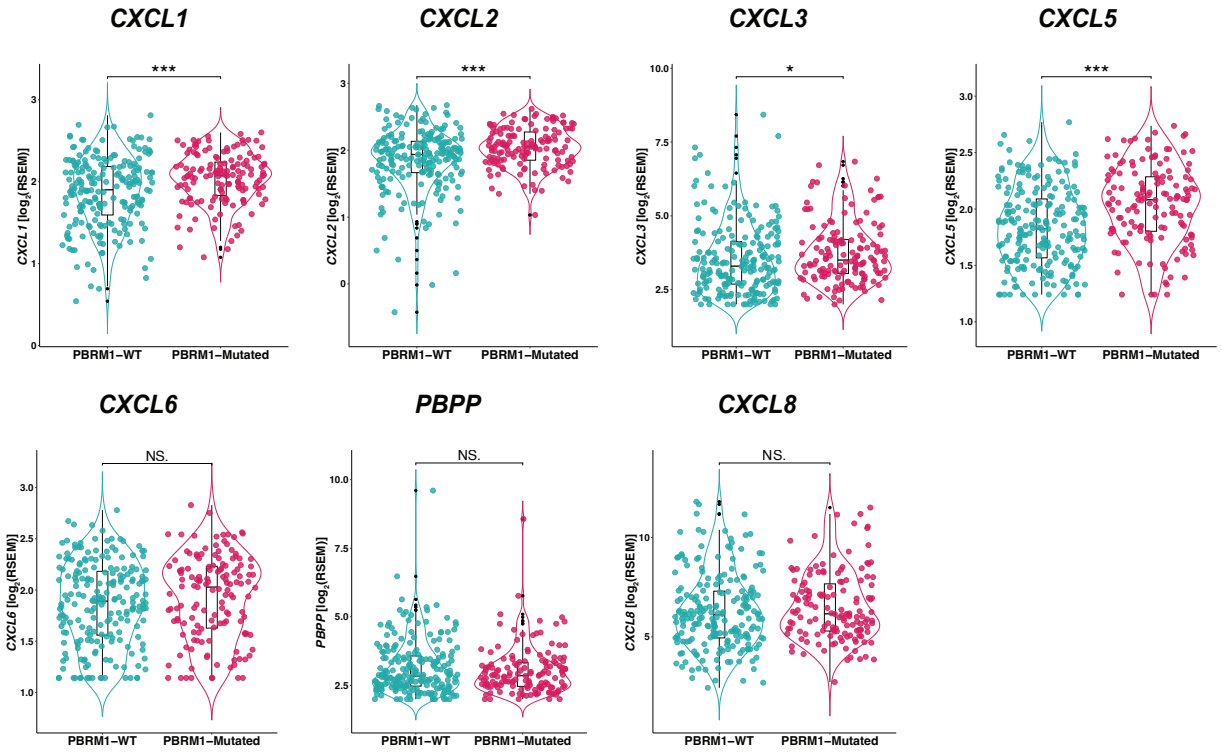

Figure 3.7: mRNA expression profile of CXCR2-binding chemokines in relation to *PBRM1* mutation status. The depicted mRNA expression values are RSEM-normalized $\log_2$ values of 399 ccRCC patients stratified based on *PBRM1* mutation status. In regards to boxplots, the upper and lower hinges represent the 75th and 25th percentiles, respectively and the middle line denotes the median. The whiskers extend in both directions until reaching the max or min value. * denotes $p < 0.05$, *** denotes $p < 0.001$, and NS. (not significant) denotes $p > 0.05$ as determined by Wilcoxon rank-sum test using 'stat_signif' function of the 'ggsignif' package in R.

3.3. *PBRM1*-KO cell lines were hypersensitive to various pro-inflammatory signals in TME

To begin to study the influence of *PBRM1* depletion on the expression of CXCR2-activating chemokines in ccRCC, we established an unbiased in vitro model using conventional CRISPR-Cas9 mediated knock-out (KO) to introduce loss-of-function *PBRM1* mutations in Caki1 cell line, which is a well-established cell line for ccRCC research as these cells were able to form clear cell tumors in immune-incompetent mice model (Brodaczewska et al., 2016). Two sgRNA pairs, henceforth called PBRM1_1 and PBRM1_2, were used to circumvent potential off-target effects. ccRCC cells were transfected with Px459 plasmid that encodes a Cas9 endonuclease, a *PBRM1* sgRNA, and a puromycin resistance cassette for selection. The *PBRM1*-KO cell line was established by PD. Dr. Niklas Klümper. The ccRCC cells were exposed to IFNγ, TNFα, and IL17A, which were among the most abundant cytokines in RCC TME (Lee et al., 2022), and subsequently subjected to bulk RNA sequencing; cell-cultured supernatant were also harvested for ELISA and multiplex bead-based immunoassay.

Successful KO of *PBRM1* in Caki1 cells was validated using RNA-seq and Western blot (WB) (**Figure 3.8.A-B**). In RNA-seq analysis, *PBRM1*-KO cells generated by two different sgRNA were clustered together regardless of treatment (IFNγ or TNFα), indicating a close genetic similarity between PBRM1_1 and PBRM1_2 defective cells (**Figure 3.8.C**). In PCA, there was a clear separation between *PBRM1* KO vs. WT on PC1 and PBRM1_1 vs. PBRM1_2 on PC2 (**Figure 3.8.D**). The number of significantly upregulated genes (log_2 FC > 0 and p-adjusted < 0.05) due to *PBRM1* deletion in normal cultured condition or in response to either IFNγ or TNFα was as follows: 1607, 1360, and 1167 genes (**Figure 3.8.E**). Expression of 1396, 991, and 1025 genes was significantly downregulated (log_2 FC > 0 and p-adjusted < 0.05) in response to inactivation of *PBRM1* compared to *PBRM1*-WT in the absence or presence of either IFNγ or TNFα, respectively. As shown in Venn diagrams (**Figure 3.8.F**), a significant number of DEGs (628 commonly up-regulated and 411 commonly down-regulated due to *PBRM1* abrogation) were shared among the untreated, and treated with either IFNγ or TNFα conditions. In all three aforementioned treatments, the top upregulated genes were *SLC16A9* (Monocarboxylate transporter 9), *ALDH1A3* (Aldehyde dehydrogenase 1 family, member A3), *NMU* (Neuromedin U), *MELTF* (Melanotransferrin), *IGFBP7* (Insulin Like Growth Factor Binding Protein 7),

FGFR1 (Fibroblast Growth Factor Receptor 1), and *TSPAN5* (Tetraspanin 5) (**Figure 3.8.G**). The top downregulated genes were *PDLIM1* (DZ and LIM domain protein 1), *VAMP8* (Vesicle-associated membrane protein 8), *CHST11* (Carbohydrate sulfotransferase 11), *ADRB2* (β_2 adrenoreceptor), and *DENND2A* (DENN Domain-Containing Protein 2A).

Importantly, consistent with the RNA-seq result of pharmacological inhibition of PBRM1 in previous section, *CXCL5* transcripts were at least five-fold higher in *PBRM1*-KO cells relative to *PBRM1*-WT cells, regardless of stimulation. We further examined closely the transcriptional expression of all CXCR2-binding chemokines (**Figure 3.9.A**). Transcripts of *PPBP* was undetectable in this experiment which is similar to the RNA-seq result of biochemical inactivation of PBRM1 activity. Under normal cultured condition, *PBRM1*-KO generally increased the mRNA expression of all CXCR2 ligands, although only *CXCL5* and *CXCL8* reached statistical significance. Furthermore, except for *CXCL2*, transcription of other CXCR2 ligands was suppressed in both *PBRM1*-KO and WT cells in response to IFNγ treatment. In contrast, TNFα treatment dramatically increased the expression of all CXCR2-activating chemokines not only in *PBRM1*-loss cells but also in control cells, while the observed pattern of PBRM1-deficient cells expressing higher mRNA levels of these chemokines was still preserved.

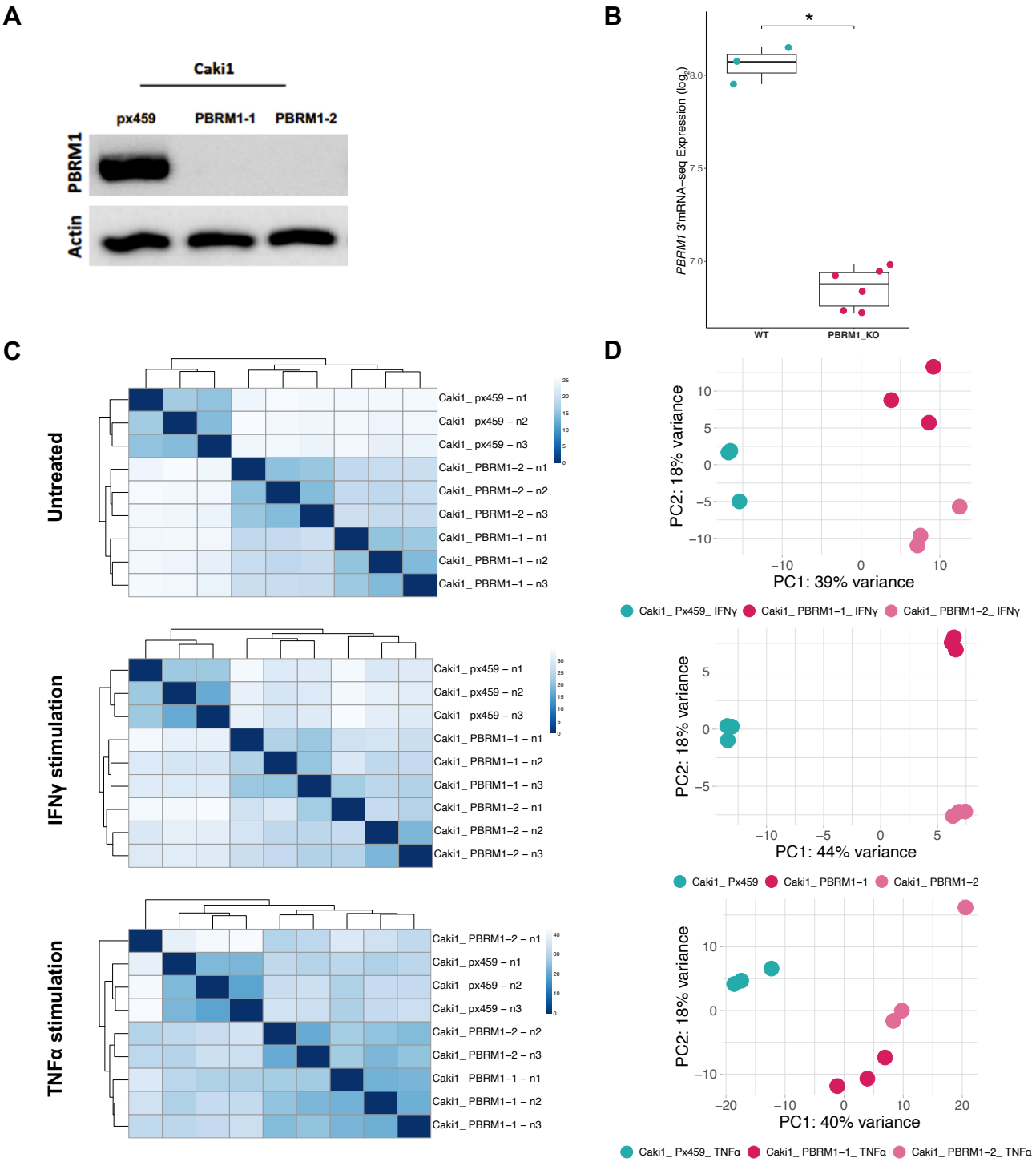
A
Caki1
px459
PBRM1-1
PBRM1-2
PBRM1
Actin
B
*
PBRM1 3'mRNA-seq Expression (log2)
8.0
7.5
7.0
WT
PBRM1_KO
C
Untreated
Caki1_ px459 – n1
Caki1_ px459 – n2
Caki1_ px459 – n3
Caki1_ PBRM1–2 – n1
Caki1_ PBRM1–2 – n2
Caki1_ PBRM1–2 – n3
Caki1_ PBRM1–1 – n1
Caki1_ PBRM1–1 – n2
Caki1_ PBRM1–1 – n3
IFNγ stimulation
Caki1_ px459 – n1
Caki1_ px459 – n2
Caki1_ px459 – n3
Caki1_ PBRM1–1 – n1
Caki1_ PBRM1–1 – n2
Caki1_ PBRM1–1 – n3
Caki1_ PBRM1–2 – n1
Caki1_ PBRM1–2 – n2
Caki1_ PBRM1–2 – n3
TNFα stimulation
Caki1_ PBRM1–2 – n1
Caki1_ px459 – n1
Caki1_ px459 – n2
Caki1_ px459 – n3
Caki1_ PBRM1–2 – n2
Caki1_ PBRM1–2 – n3
Caki1_ PBRM1–1 – n1
Caki1_ PBRM1–1 – n2
Caki1_ PBRM1–1 – n3
D
PC2: 18% variance
PC1: 39% variance
Caki1_ Px459_ IFNγ
Caki1_ PBRM1–1_ IFNγ
Caki1_ PBRM1–2_ IFNγ
PC2: 18% variance
PC1: 44% variance
Caki1_ Px459
Caki1_ PBRM1–1
Caki1_ PBRM1–2
PC2: 18% variance
PC1: 40% variance
Caki1_ Px459_ TNFα
Caki1_ PBRM1–1_ TNFα
Caki1_ PBRM1–2_ TNFα

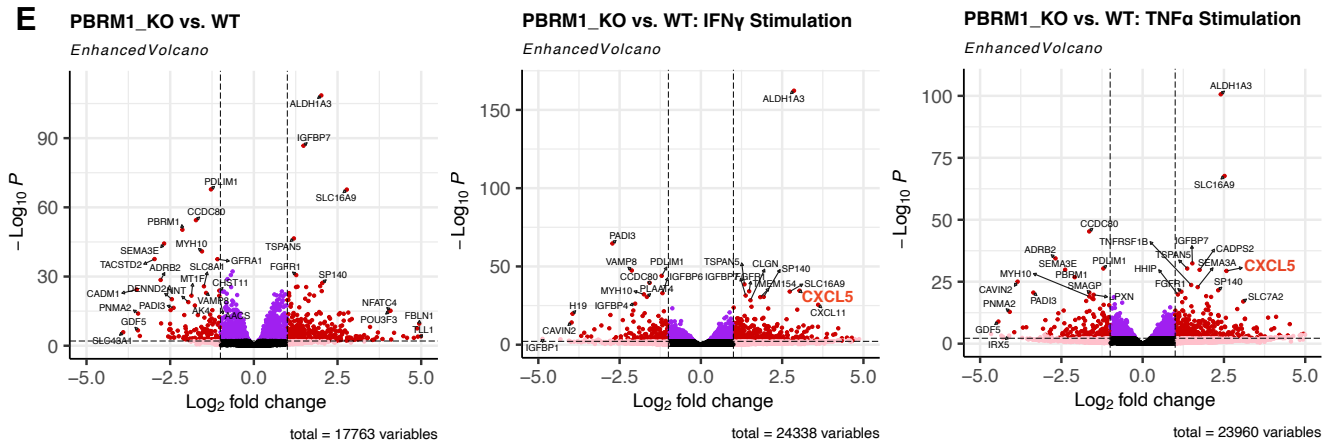
E
PBRM1_KO vs. WT
EnhancedVolcano
PBRM1_KO vs. WT: IFNγ Stimulation
EnhancedVolcano
PBRM1_KO vs. WT: TNFα Stimulation
EnhancedVolcano
−Log10 P
Log2 fold change
total = 17763 variables
total = 24338 variables
total = 23960 variables

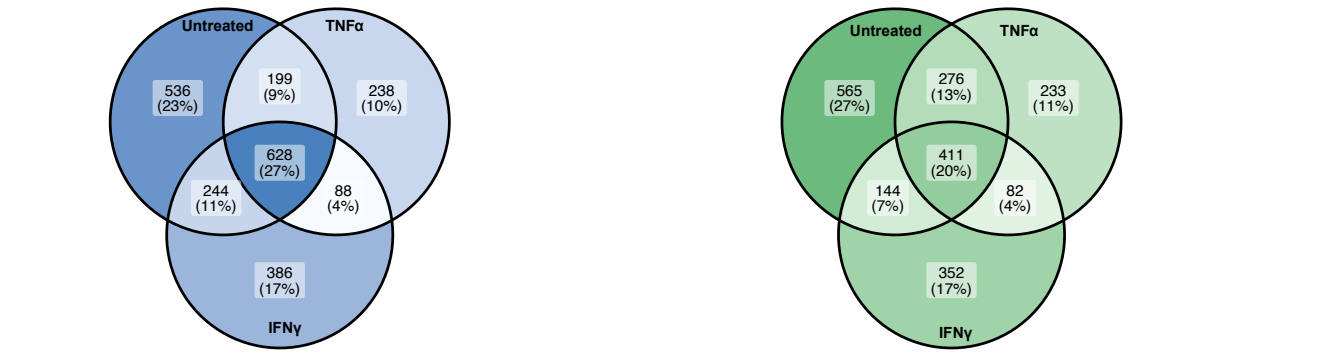
F
Untreated
TNFα
IFNγ
536 (23%)
199 (9%)
238 (10%)
628 (27%)
244 (11%)
88 (4%)
386 (17%)
565 (27%)
276 (13%)
233 (11%)
411 (20%)
144 (7%)
82 (4%)
352 (17%)

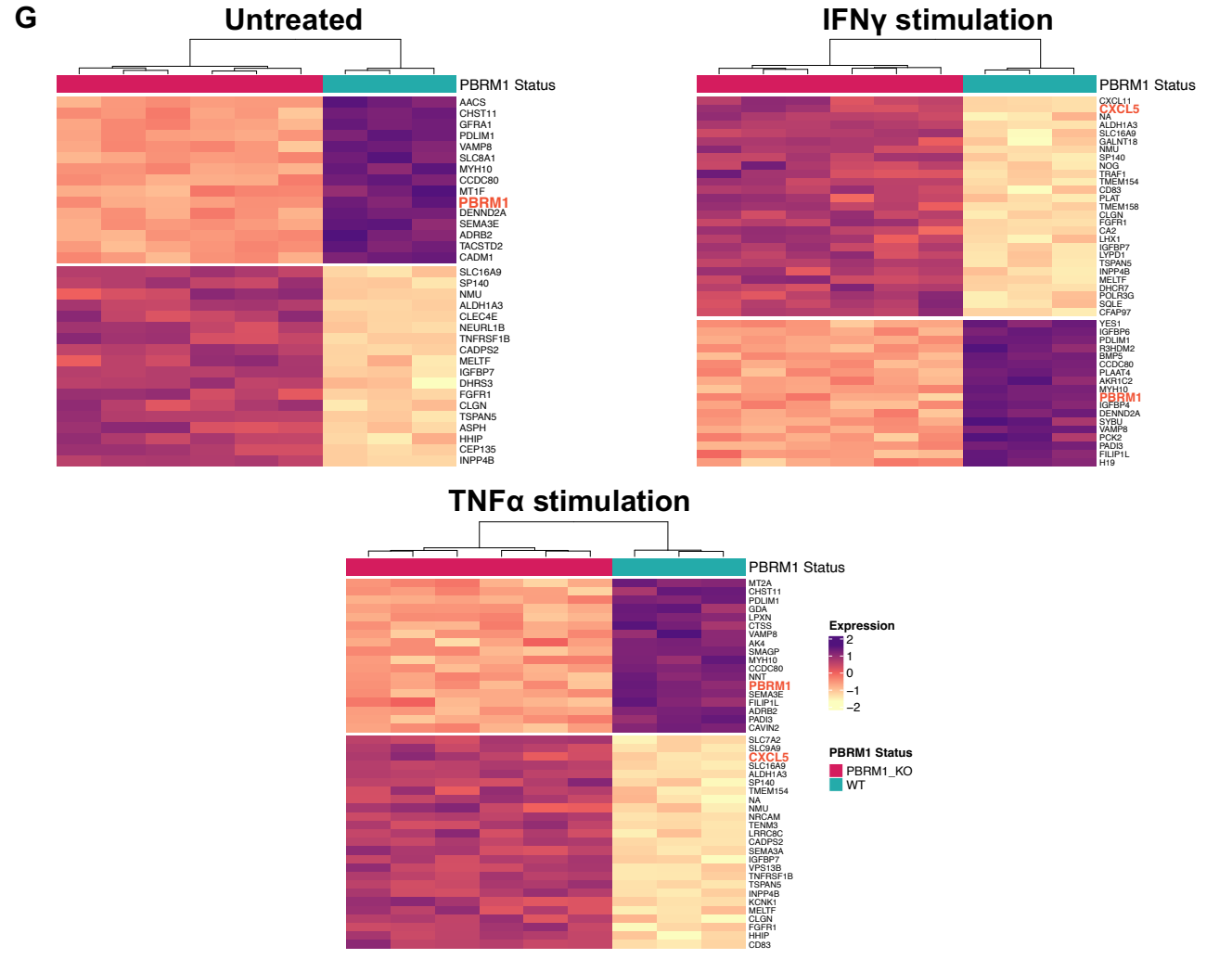
G
Untreated
IFNγ stimulation
TNFα stimulation
PBRM1 Status
Expression
PBRM1_KO
WT

Figure 3.8: Differential Gene Expression analysis of *PBRM1* KO vs. WT Caki1 cells in response to pro-inflammatory signals. *PBRM1*-KO ccRCC cells were generated using CRISPR-Cas9 and two different sgRNA (PBRM1_1 and PBRM1_2). Mock cells were transfected with Px459 backbone only. *PBRM1*-KO Caki1 cells were confirmed at the protein level through Western blot (A) and at the mRNA level via RNA-seq (B). (C) Clustering heatmaps were generated by calculating the Euclidean distances between *PBRM1*- KO and WT samples which were unstimulated or stimulated with 250 U/mL IFNγ or 250 U/mL TNFα. (D) PCA plots using the results from DESeq2 analysis followed by rlog transformation exhibit the extent of intra-group homogeneity and the prominent source of data variability. (E) Volcano plots of all DEGs between *PBRM1*-KO and *PBRM1*-WT cells. The vertical and horizontal dashed lines exhibit p-adjusted value = 0.05 and $\log_2$ FC = 0.5. The purple dots and red dots represent genes with statistically significant alterations within and above $\log_2$ FC of -0.5 and 0.5, respectively. (F) Venn diagrams showing the overlaps of mRNAs that are significantly activated (left, blue) or suppressed (right, green) (FDR < 0.05) by *PBRM1* depletion in three cultured conditions: unstimulated or stimulated with either IFNγ or TNFα. (G) Heatmaps of top 50 DEGs demonstrate hierarchical clustering results of the comparisons between *PBRM1*-KO and *PBRM1*-WT, which rlog gene expression values of genes with FDR <0.05 and $\log_2$FC >1 or <1 were centered and scaled to get z-score. Z-scores are colored according to upregulation (red) or downregulation (blue).

To corroborate what we observed in Caki1 cells can be generalized for ccRCC, we performed *PBRM1* knock-out using CRISPR/Cas9 in 786O cells, which is a ccRCC cell line that contains loss-of-function mutations in *VHL* and *HIF1A*. The abolishment of *PBRM1* expression in 786O cells were validated utilizing WB (**Figure 3.9.B**). A fade band of PBRM1 in PBRM1_2 cells was worthy of note, which can be explained by polyclonal knock-out approach leading to the existence of *PBRM1* WT or heterozygous-deleted cells in the PBRM1_2 population. Next, to confirm whether there is a positive correlation between the protein levels and the observed elevated mRNA levels of CXCR2 ligands in *PBRM1*-KO cells as well as the transcriptional hyperactivation of these chemokines following TNFα and IL17A treatments, we quantified secreted CXCL chemokines in ccRCC supernatant using the LEGENDplex human proinflammatory chemokine panel 1 and 2, and the R&D human CXCL6 ELISA kit. There was high concordance between transcript levels and protein amounts of CXCR2 ligands in ccRCC cells. Particularly, *PBRM1*-KO cells of both Caki1 and 786O had significantly higher production of CXCL1, CXCL5, and CXCL6 (only for Caki1) at baseline compared to *PBRM1*-intact cells (**Figure 3.9.C**). Similarly, CXCL2 and CXCL8 were more highly secreted at baseline by PBRM1_2 but not PBRM1_1 cells than the Px459 control cells in both Caki1 and 786O. Both TNFα and IL17A induced the release of pro-angiogenic chemokines, with the more robust induction of these chemokines production still detected in *PBRM1*-loss Caki1 and 786O cells. For example, secretion of CXCL5 was increased 24-fold and 32-fold in Caki1 Px459 cells after TNFα and IL17A stimulation, respectively; and the Caki1 PBRM1_1 cells released twice as much CXCL5 as the control cells in response to IL17A. Generally, IL17A

was more potent than TNFα in stimulating the secretion of CXCR2-binding chemokines by ccRCC cells. Of note, there was a discrepancy in the amount of CXCR2 ligands secreted by Caki1 vs. 786O, which 786O cells produced more CXCL1, CXCL5, and CXCL8 at baseline as well as following the exposure to TNFα and IL17A. As hypoxia-regulated expression of CXCL chemokines has been extensively reported (Korbecki et al., 2021), as well as pVHL and HIF1A are undetectable in 786O, the disparity between two cell lines might be attributed to hypoxia signaling.

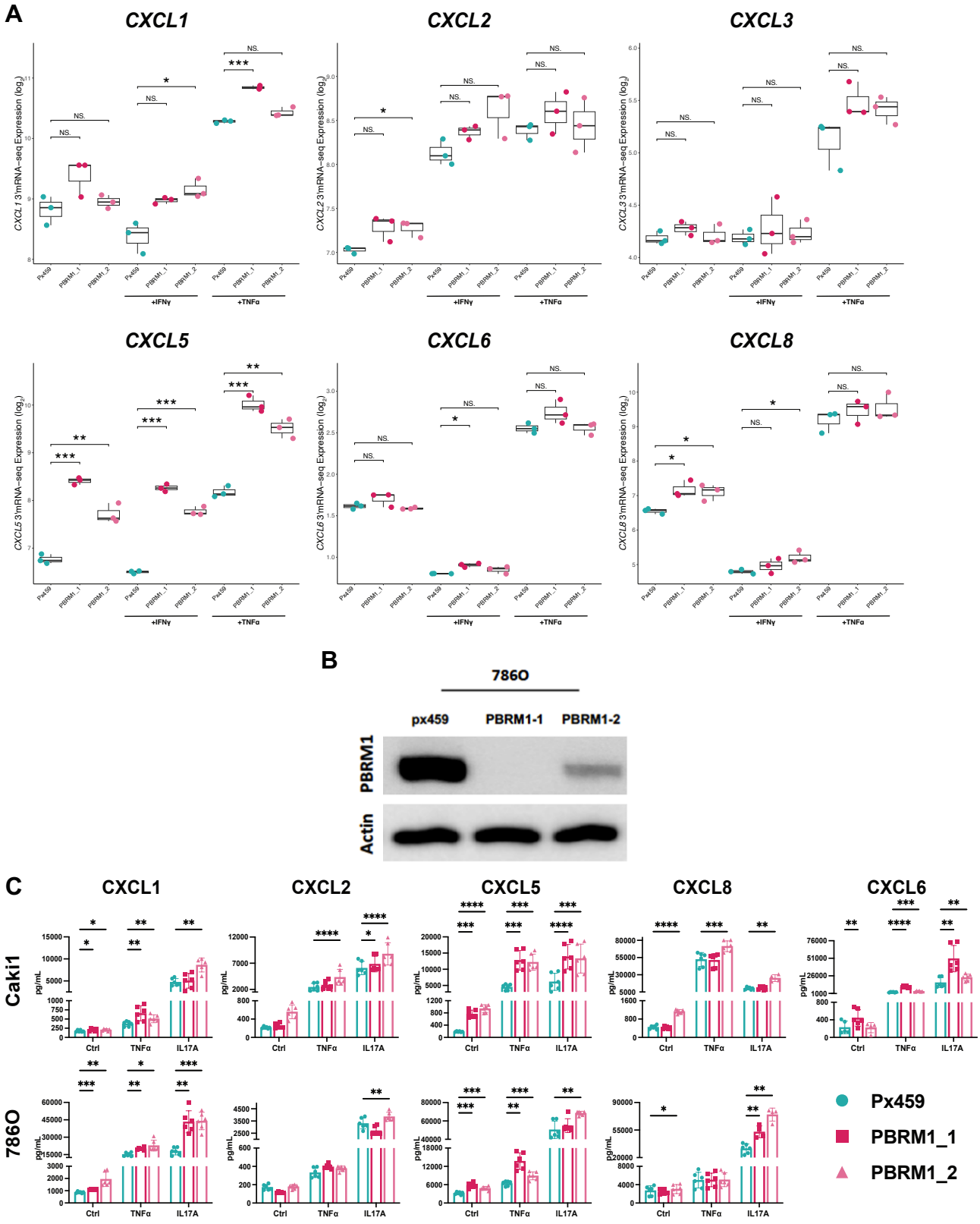
A
CXCL1
CXCL2
CXCL3
CXCL5
CXCL6
CXCL8
B
786O
px459
PBRM1-1
PBRM1-2
PBRM1
Actin
C
CXCL1
CXCL2
CXCL5
CXCL8
CXCL6
Caki1
786O
Ctrl
TNFα
IL17A
Px459
PBRM1_1
PBRM1_2

Figure 3.9: PBRM1-KO cells are hypersensitive to pro-inflammatory signals. (A) Caki1 cells were untreated or treated with human recombinant 250 U/mL IFNγ or 250 U/mL TNFα and transcriptomic changes of CXCR2-binding ligands were evaluated by RNA-seq (Each dot depicts log2-transformed value). A two-sample t-test was performed for statistical significance, *p < 0.05, **p < 0.01, ***p < 0.001. (B) *PBRM1*-KO 786O cells were confirmed at the protein level through Western blot. (C) Profile of CXCR2-activating chemokines secreted by Caki1 and 786O cells. ccRCC cells were exposed to either 250 U/mL TNFα or 100 ng/mL IL-17A and incubated for 48 hours. Graphs demonstrate mean protein concentration ± SD from three independent experiments. Data were analyzed by two-way ANOVA/mixed-effects analysis plus Dunnett's multiple comparison test and statistical significances are depicted: *p < 0.05, **p < 0.01, ***p < 0.001, ****p < 0.0001.

3.4. The prognostic significance of *CXCL5* expression in TCGA-KIRC dataset

As we observed that *CXCL5* was significantly released by *PBRM1*-deficient ccRCC cells, we asked whether *CXCL5* level can predict the prognosis of ccRCC tumors. We dichotomized the TCGA-KIRC data into *CXCL5* high and low groups using the median of *CXCL5* mRNA expression. Clinical characteristics at baseline of this cohort were detailed in **Table 13**. Remarkably, *PBRM1*-mutated samples accounted for up to half of the *CXCL5*-high population, whereas *PBRM1*-mutated samples constituted less than one-third of *CXCL5*-low samples (Chi square p < 0.001). Interestingly, male patients were twice as likely to have high levels of *CXCL5* mRNA than female patients, while there was approximately an equal number of male and female patients in *CXCL5*-low group (Chi square p < 0.001). *CXCL5*-high expression was associated with shortened PFS, DSS, and OS (**Figure 3.10**), with 85% 12-month survival rate and a median OS of 65 months (95% CI, 53 to NR) compared with 95% 12-month survival and median OS not reached (95% CI, 93 to NR) for *CXCL5*-low tumors. In multivariable Cox regression co-adjusted for age, sex, *PBRM1* mutation status, and the AJCC staging, *CXCL5*-high expression led to an 81% risk augmentation for death compared with *CXCL5*-low tumors (hazard ratio, 1.81 [95% CI, 1.23 to 2.67], p = 0.002; **Table 14**).

Table 13: Baseline characteristics of the TCGA-KIRC cohort

Characteristic	***CXCL5* High**, n = 200[1]	***CXCL5* Low**, n = 199[1]	**p-value**[2]
***PBRM1* Mutation**			**<0.001**
No mutation	108 (54%)	148 (74%)	
Mutated	92 (46%)	51 (26%)	
Age			0.2
Median (IQR)	61 (52, 72)	59 (52, 68)	
Range	33, 90	32, 88	
Sex			**<0.001**
Female	50 (25%)	97 (49%)	
Male	150 (75%)	102 (51%)	
AJCC staging			0.2
STAGE I	94 (47%)	105 (53%)	
STAGE II	18 (9.0%)	26 (13%)	
STAGE III	51 (26%)	41 (21%)	
STAGE IV	37 (19%)	27 (14%)	

[1]n (%)

[2]Pearson's Chi-squared test; Wilcoxon rank sum test

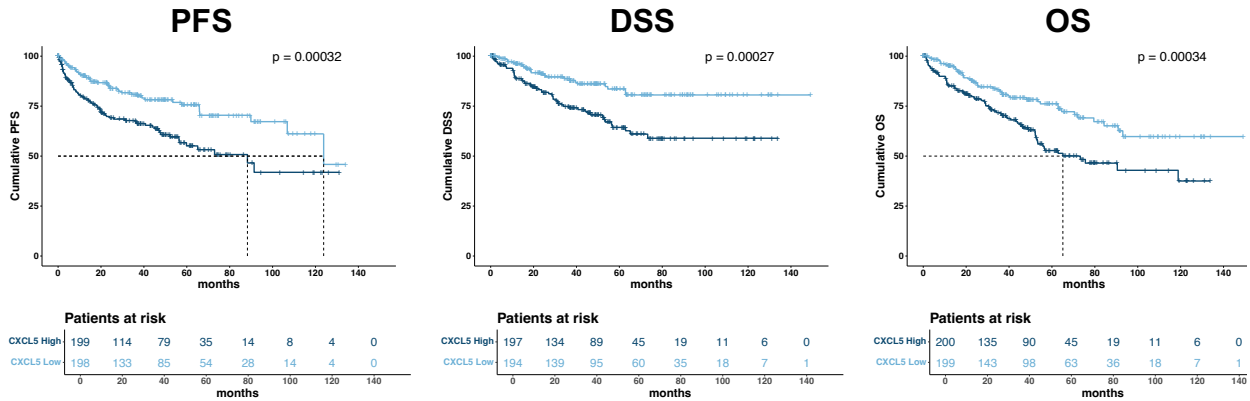

Figure 3.10: The clinical significance of *CXCL5* expression on patient survival in the TCGA-KIRC. Kaplan–Meier analyses demonstrate the impact of *CXCL5* mRNA level (relative to the median) on PFS, DSS, and OS among patients. Two-sided log-rank test was performed to compare between *CXCL5* high/low groups.

Table 14: Multivariate Cox regression analysis for the TCGA-KIRC cohort

	Progression Free Survival				Overall Survival			
Characteristic	**N**	**HR[1]**	**95% CI[1]**	**p-value**	**N**	**HR[1]**	**95% CI[1]**	**p-value**
***CXCL5* mRNA**				**0.002**				**0.002**
CXCL5 Low	198	—	—		199	—	—	
CXCL5 High	199	1.85	1.24, 2.77		200	1.81	1.23, 2.67	
***PBRM1* Mutation**				0.93				0.11
No mutation	254	—	—		256	—	—	
Mutated	143	0.98	0.67, 1.45		143	0.73	0.50, 1.08	
Age	397	1.01	0.99, 1.03	0.22	399	1.05	1.03, 1.07	**<0.001**
Sex				0.38				0.81
Female	146	—	—		147	—	—	
Male	251	1.21	0.79, 1.84		252	1.05	0.71, 1.54	
AJCC staging				**<0.001**				**<0.001**
STAGE I	199	—	—		199	—	—	
STAGE II	44	3.24	1.49, 7.04		44	1.31	0.59, 2.92	
STAGE III	92	5.40	2.98, 9.79		92	2.48	1.49, 4.13	
STAGE IV	62	23.9	13.5, 42.1		64	9.27	5.77, 14.9	

[1]HR = Hazard Ratio, CI = Confidence Interval

3.5. The influence of *PBRM1*-KO cell lines on the proliferation, signaling activation, and capillary formation of endothelial cells.

Tumor angiogenesis is an inexorable consequence of growing tumors owing to their insatiable need for nutrients and oxygen. Cancer cells can modulate endothelial cell activities through several mechanisms, involving soluble factor and vesicle secretion, as well as direct contact via gap junctions and adhesion receptors (Bruno Miguel et al., 2016), which successively advance endothelial cell proliferation, migration, and vessel formation. The most common target of clinical-use anti-angiogenic drugs for cancer treatment is VEGF/VEGFR axis (Liu et al., 2023). Although the contributing role of CXCR2-binding chemokines in tumor angiogenesis has been reported in a variety of cancer types (Gerber et al., 2009; Keeley et al., 2010), the therapeutic potential of these chemokines has often been overlooked and underrepresented in current scientific studies.

As we observed the upregulation of different CXCR2-binding chemokines in *PBRM1*-loss cells regardless of stimulation, we asked to what magnitude these chemokines exert influence on proangiogenic phenotype of PBRM1-mutant ccRCC tumors. We thus used human umbilical vein endothelial cells (HUVECs) and conditioned-media (CM) from Caki1 and 786O to investigate the crosstalk between cancer cells and endothelial cells.

HUVECs were cultured in CM of ccRCC cells at increasing percentages for 3 days. In both Caki1 and 786O, the higher the amount of the supernatant was added, the better HUVECs proliferated (**Figure 3.11.A**). Importantly, *PBRM1*-KO supernatant significantly promoted HUVECs viability compared to *PBRM1*-WT as measured by the CellTiter Glo assay. Furthermore, the HUVEC-survival-support effect of ccRCC CM was intensified by supplementing 25 ng/mL VEGFA or was abrogated in the presence of 1 μM CXCR2 inhibitor or 0.1 μM sunitinib or 100 μg/mL bevacizumab (**Figure 3.11.B**). Consistently, the combination of CXCR2 inhibitor and sunitinib or bevacizumab exerted an additive effect on HUVEC viability. Of note, the addition of recombinant human *CXCL5* to 786O CM but not Caki1 CM enhanced the proliferation of HUVECs.

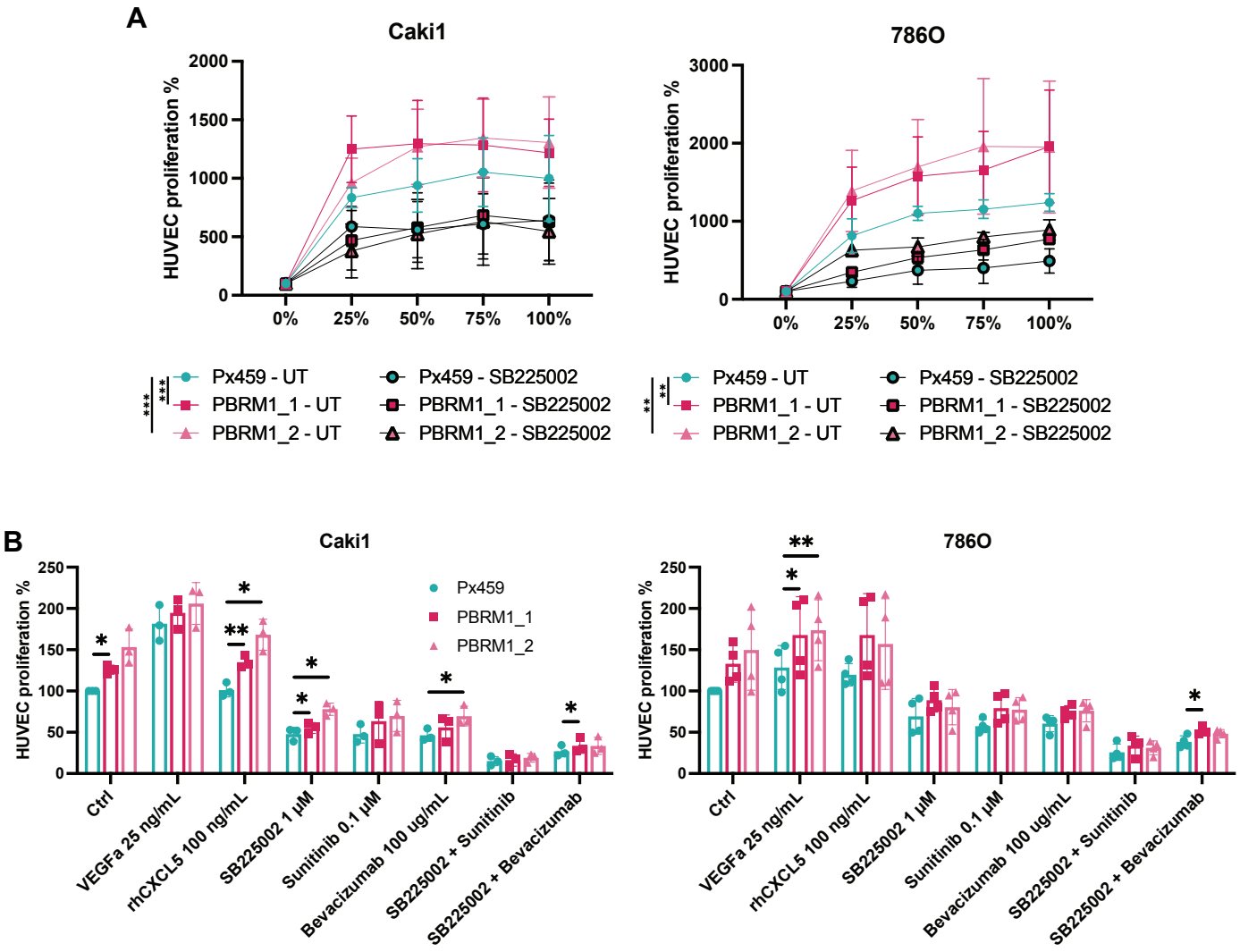

Figure 3.11: PBRM1-KO ccRCC cells are superior to PBRM1-WT in sustaining HUVEC survival and targeting CXCR2/CXCL5 axis results in a reduction of HUVEC viability. (A) HUVECs proliferation curves of HUVECs cultured in ccRCC-cell CM at different dilution percentages for 3 days. Data are presented as mean ± s.d. **p < 0.01, ***p < 0.001; two-way ANOVA with Šidák multiple comparison test. (B) HUVECs proliferated in 100% ccRCC-cell CM with the addition of recombinant human (rh) VEGFA or rhCXCL5 or CXCR2 inhibitor (SB225002) or anti-VEGF/TKI agents or combination of both. Statistical significance was calculated by two-sided unpaired t-test is showed *p < 0.05, **p < 0.01. Data were normalized to HUVECs cultured in basal media (0% dilution).

To investigate the signaling pathway by which ccRCC CM supported the HUVEC viability in CXCR2-dependent manner, we used R&D Systems Proteome Profiler Human Phospho-Kinase Arrays on untreated and Caki1-supernatant-treated HUVECs to have a holistic overview of kinase activation. As shown in **Figure 3.12.A**, HUVECs incubated with Caki1 supernatant exhibited enhanced phosphorylation of some kinases and kinase targets in comparison with the HUVECs in basal media, including 1.3-fold higher glycogen

synthase kinase-3 (GSK-3α/β) (phosphorylation sites—serine 21/29 (S21/S9)), 2.7-fold higher signal transducer and activator of transcription 3 (STAT3) at tyrosine 705 (Y705), and 1.5-fold higher cJUN at serine 63 (S63).

Next, we used WB to independently corroborate the phospho-kinase assay findings. The ccRCC supernatant was diluted in half with basal media to obtain WB signals that were visible to identify the different effects of *PBRM1*-KO and WT ccRCC supernatant and applied on HUVECs, which were starved for 4 h in basal media, for 20 min. We also checked the phosphorylation levels of extracellular signal-regulated kinases 1/2 (ERK1/2) as this is centrally phosphorylated and activated with the activation of CXCLs/CXCR2 (Cheng et al., 2019). In unstimulated HUVECs, phosphorylated-STAT3 was undetectable, while weak signals of phosphorylated c-JUN, GSK-3β, and ERK1/2 were observed (**Figure 3.12.B**). Consistent with phospho-kinase data, the phosphorylation of STAT3, c-JUN, GSK-3β, and ERK1/2 was elevated in response to secreted factors from both Caki1 and 786O.

We further investigated whether there were differences in the phosphorylated protein levels of HUVECs that were stimulated with *PBRM1*-KO and WT supernatant in CXCR2-dependent mode. In both Caki1 and 786O, higher induction of phosphorylated GSK-3β was detected in HUVECs treated with *PBRM1*-KO CM compared to *PBRM1*-WT CM (**Figure 3.12.B-E**), whereas the differences of phospho-STAT3 and phospho-ERK1/2 levels were inconsistent between *PBRM1*-KO and *PBRM1*-WT due to the biological discrepancies between PBRM1_1 and PBRM1_2 cells (**Figure 3.12.B, C and E**). Furthermore, the addition of CXCR2 inhibitor in the presences of ccRCC CM (both Caki1 and 786O) partially reduced the phosphorylated levels of STAT3 and ERK1/2 in HUVECs; conversely, sunitinib relative to CXCR2 inhibitor had no impact on STAT3 phosphorylation levels and less impact on ERK1/2 phosphorylation levels. Notably, supplement of CXCR2 inhibitor and sunitinib in *PBRM1*-KO Caki1 or 786O CM moderately blocked the phosphorylation of GSK-3β in HUVECs. The CM-induced S9 phosphorylation of GSK-3β was reduced by treatment with the selective GSK-3β inhibitors, either TWS119 (0.5 μM) or AR-A014418 (10 μM), or the GSK-3α/β inhibitor LY2090314 (0.5 μM) (**Figure 3.12.D**), which is counterintuitive since GSK-3 activity is repressed through the phosphorylation of S9 in GSK-3β. Indeed, our result is in line with findings from Zhang et al., which they observed the reduction of phosphorylated GSK-3β at both S9 and Y216 (enhanced GSK-

3 activity) sites when non-SCLC cell line was exposed to the same GSK-3β inhibitors (Zhang et al., 2017). The inhibition of GSK-3β phosphorylation by the GSK-3β inhibitors was paralleled by a decrease in the phosphorylation of ERK1/2. Among three inhibitors, only AR-A014418 significantly altered the total level of GSK-3α/β and ERK1/2 protein expression. We finally utilized various human recombinant CXCR2 ligands to verify that GSK-3β is one of downstream signaling of CXCR2 activation (**Figure 3.12.F**).

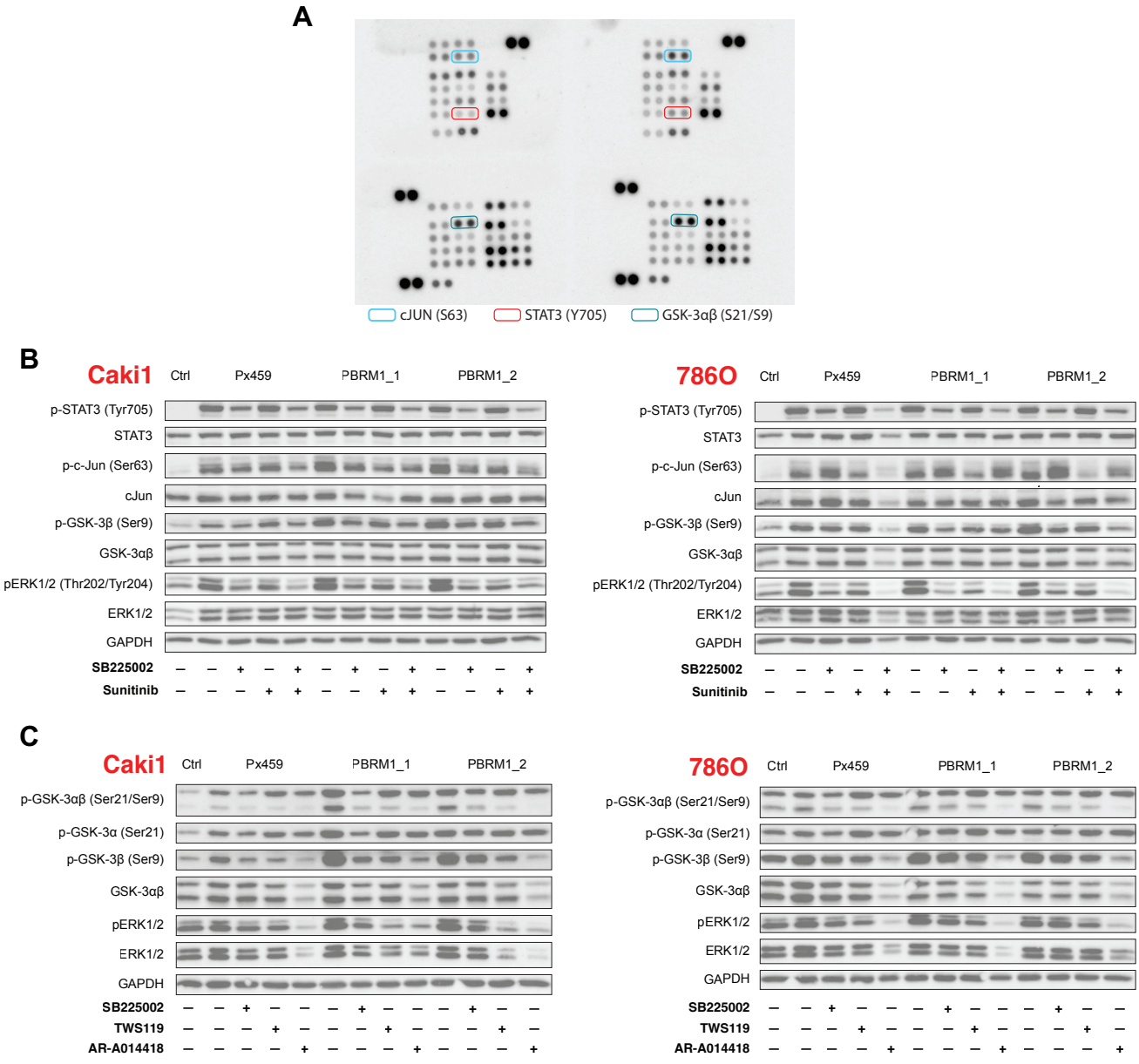

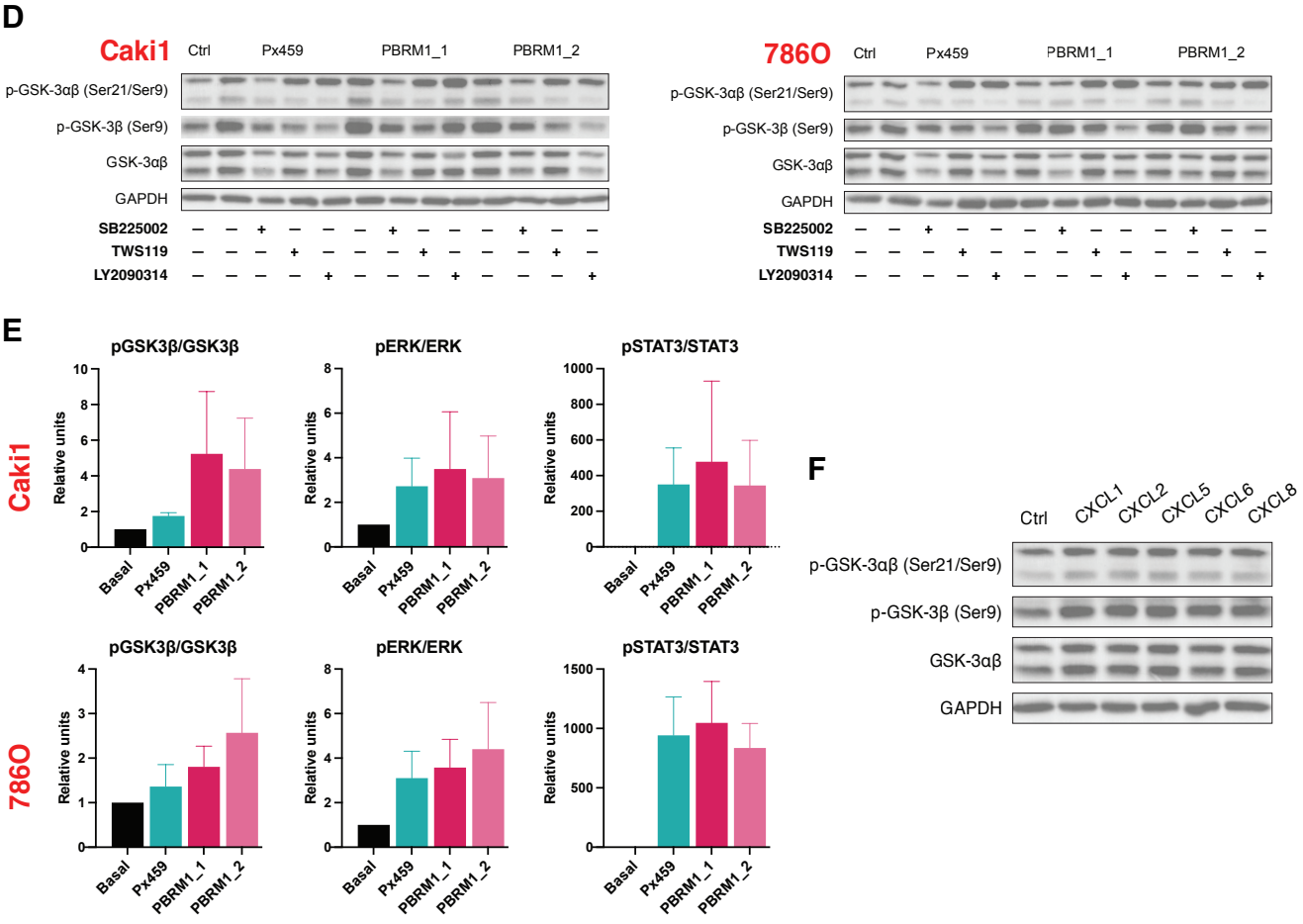

Figure 3.12: Activation of different signaling pathways in HUVECs in response to secreted factors in ccRCC CM in a CXCR2-sensitive mean. (A) Phospho-kinase array analysis of HUVECs starved for 4 h and stimulated for 20 min without or with Caki1 supernatant. (B) Western blot analysis of HUVECs starved for 4 h and pre-treated without or with either 0.5 μM SB225002 (CXCR2 inhibitor) or 100 nM sunitinib or combination of both, then stimulated with 1:2 dilution of ccRCC CM in the presence of corresponding drugs for 20 min. (C) Immunoblots of HUVECs starved for 4 h and pre-treated without or with either 0.5 μM SB225002 or the selective GSK-3β inhibitors, either TWS119 (0.5 μM) or AR-A014418 (10 μM), then incubated with 1:2 dilution of ccRCC supernatant in the presence of coressponding drugs for 20 min. (D) WB analysis of HUVECs starved for 4 h and pre-treated without or with either 0.5 μM SB225002 or 0.5 μM TWS119 or 0.5 μM LY2090314 (GSK-3αβ inhibitor), then stimulated with 1:2 dilution of ccRCC CM in the presence of corresponding drugs for 20 min. (E) Phosphorylation levels of GSK3β, ERK1/2, and STAT3 normalized to their corresponding total protein levels are shown in the histograms (data of at least three independent experiments). (F) Immunoblots of HUVECs starved for 4 h and stimulated with various human recombinant CXCR2-activating chemokines for 20 min.

To examine the involvement of CXCR2 ligands in ccRCC CM in angiogenic sprouting, we employed a three-dimensional model in which HUVECs spheroids were embedded in collagen matrix and stimulated with basal media containing angiogenic factors or supernatant from cancer cells (**Figure 3.13.A**). The capillary-like structures projected from HUVEC spheroids were observed in the presence of 25 ng/mL recombinant VEGFA which served as a positive control (**Figure 3.13.B**). Of note, HUVEC sprouting capacity varied according to passage number, with high passage number correlating with increased capillary-like formation. This is in complete agreement with previous findings from Heiss and colleagues (Heiss et al., 2015). Indeed, *PBRM1*-KO supernatant from both Caki1 and 786O elicited pronounced sprouting of HUVECs in terms of the number of sprouts per spheroid as well as the cumulative length of those sprouts in comparison to *PBRM1*-WT supernatant (**Figure 3.13.C** and **Figure 3.14.A**). The supernatant-induced sprouting effect was conspicuously negated with the addition of either 0.5 μM CXCR2 inhibitor or 5 μg/mL CXCL5 Ab (**Figure 3.13.C** and **Figure 3.14.B**). CXCR2 inhibitor was superior to CXCL5 Ab in suppressing sprouting capacity of HUVEC-treated with Caki1 CM, whereas the anti-angiogenic effect of CXCL5 Ab, relative to CXCR2 inhibitor, was more robust in HUVECs stimulated with 786O supernatant.

To sum up, we showed that HUVEC proliferation and angiogenic function were sustained by CXCR2-activating chemokines secreted by ccRCC cells. The influence of ccRCC cells on endothelial cells via paracrine communication can be attributed to the GSK3β signaling, which in turn can be curbed by CXCR2 blockage (or CXCL5 blocking Ab with respect to sprouting capability). Remarkably, *PBRM1*-loss in ccRCC amplified CXCR2-ligand pro-angiogenic cascade, which provides a broader mechanistic understanding of high angiogenic signature in PBRM1-deficient ccRCC tumors.

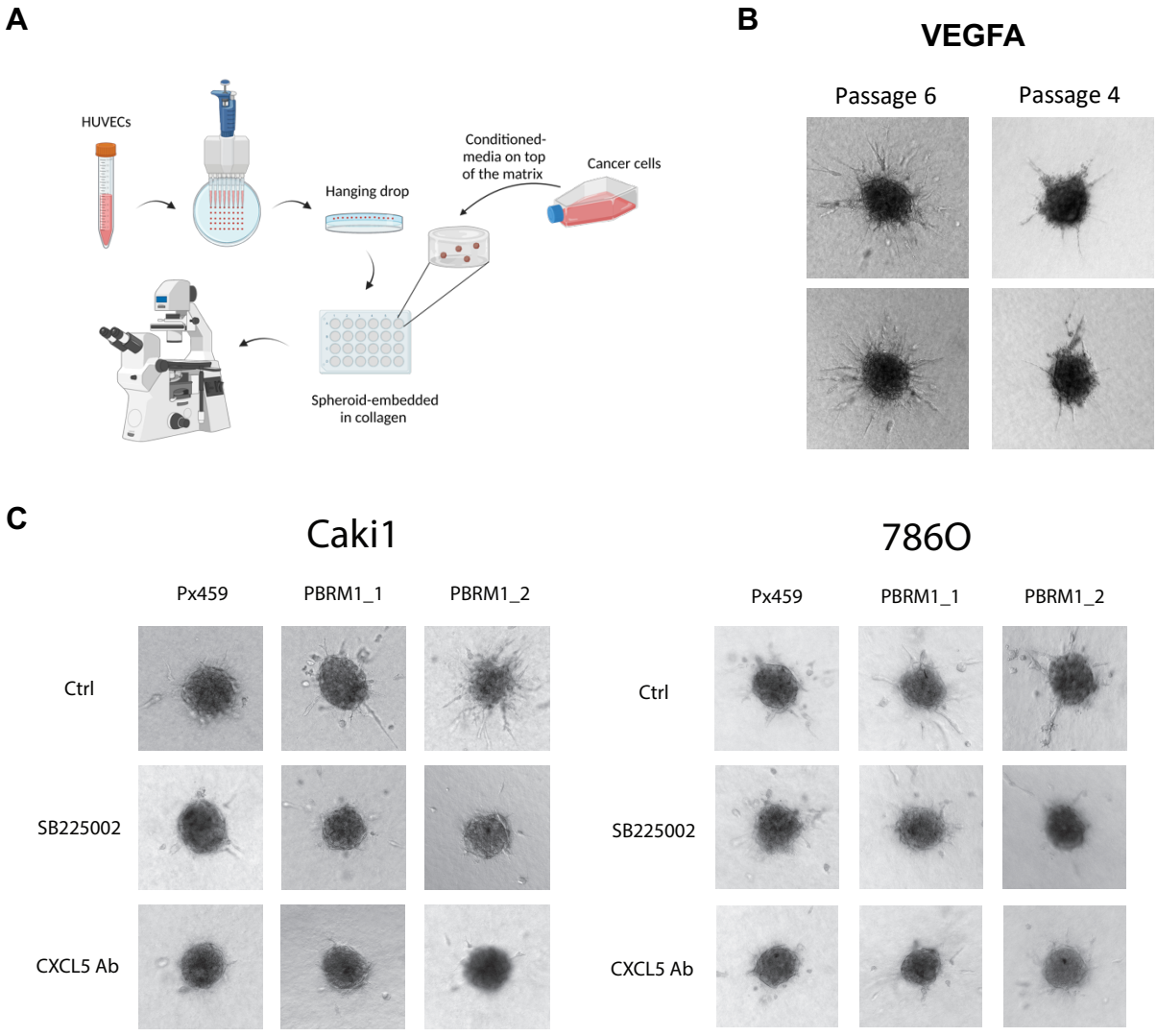

Figure 3.13: In vitro 3D spheroid assay recapitulates vessel formation. (A) Workflow of the HUVEC spheroid sprouting assay. (B) Representative pictures of sprouts formed by HUVEC-spheroids in the presence of 25 ng/mL human recombinant VEGFA which served as positive control. (C) Phase-contrast images at 10X magnification of induced-sprouting spheroids by ccRCC-cell CM without or with either 0.5 µM CXCR2 inhibitor or 5 µg/mL CXCL5 blocking antibodies.

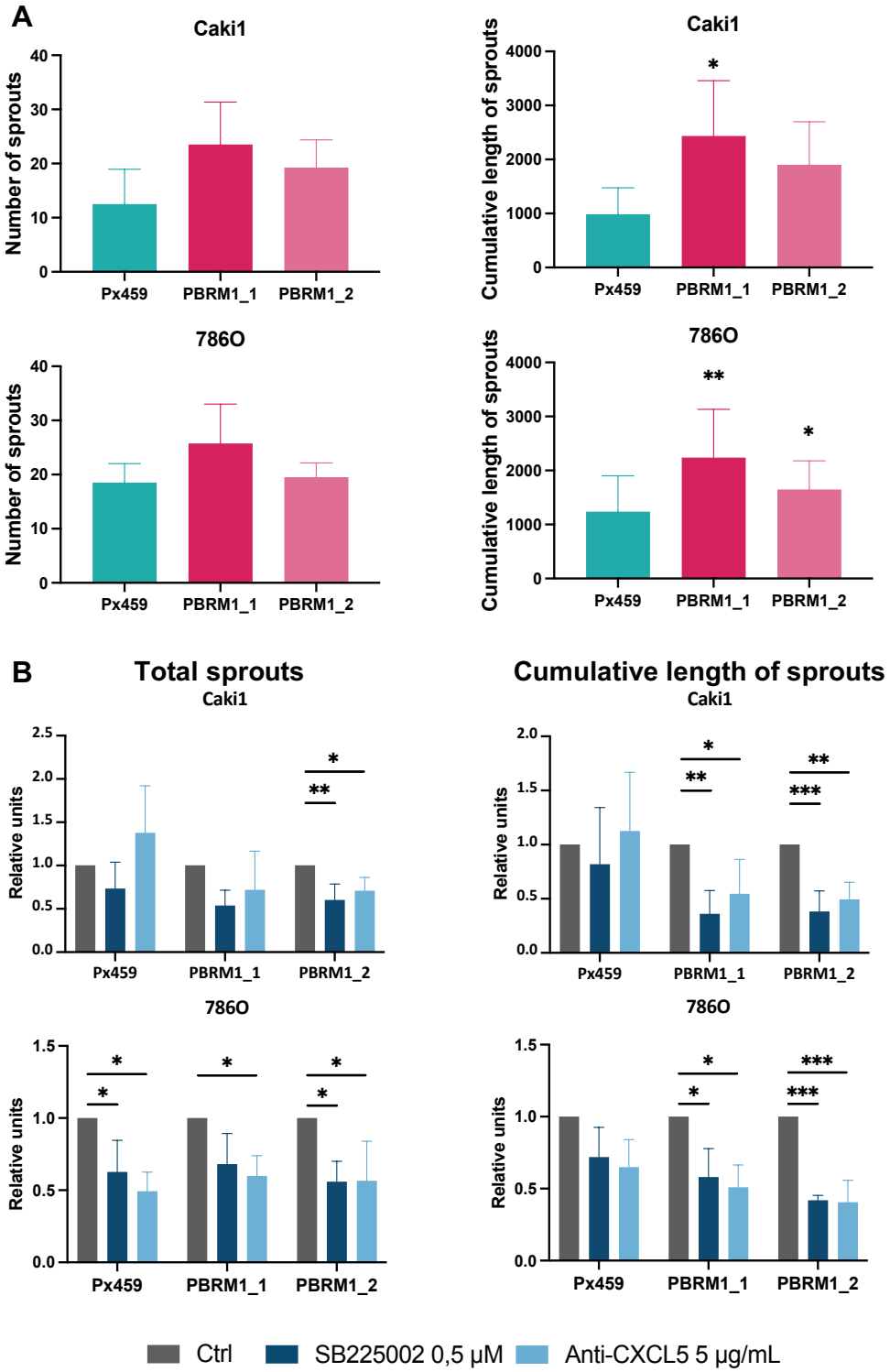

Figure 3.14: Quantitative analysis of 3D sprouting assay is demonstrated in the total number of sprouts and cumulative sprout length. (A) Results of the analysis show the pro-angiogenic effect of ccRCC CM on spheroid sprouting. (B) Anti CXCR2-CXCL5 axis counters the effect of PBRM1-KO cells on HUVECs' angiogenic capability. Bar graphs show combined data of three independent experiments, n = 6 spheroids for each experiment. Relative units represent data which were normalized to the control of that replicate and analyzed by one-way ANOVA plus Šidák's post-test. Statistical significance is showed *p < 0.05, **p < 0.01, ***p < 0.001.

3.6. The inoculation of ccRCC tumors on chicken chorioallantoic membrane (CAM) assay

To examine the extent to which the obstruction of the CXCR2/CXCL5 pathway can dampen the growth of ccRCC, we employed CAM assay for our in vivo tumor proliferation (**Figure 3.15.A**). Accordingly, we incorporated two other ccRCC cell lines, OSRC2 and KMRC1, which are in the top three ccRCC cell lines with highest gene expression of *CXCL5* in DepMap database (https://depmap.org/portal/). Besides, we also included NCI-H1048, a small cell lung cancer cell line (SCLC) that does not secrete CXCL5, to investigate whether the tumor growth on CAM is CXCL5 dependent. Our CAM assay protocol was established based on the improved protocol from Kunz and colleagues (Kunz et al., 2019). In this article, the authors compared the usages of different reagents, materials as well as handling techniques to ameliorate embryo survival as well as tumor take rates. With respect to our experiment, at from embryonic day (ED) 8, 2 to 3 million cancer cells were submerged in matrices with normal level of growth factors. The cell suspension was directly implanted on CAM membrane that was lightly lacerated using a cannula. Ethical approval was not required in our case since we concluded our experiment at ED14.

All ccRCC and SCLC cell lines grew noticeably at a macroscopic level (**Figure 3.15.B**). The tumors were encircled by a wide vascularization area. With the same number of cells transplanted on the CAM, the biggest tumor was formed by OSCR2 (26.6 ± 8.7 $mm^{3)}$ in comparison with Caki1 (16.8 ± 3.9 mm^3), 786O (11.1 ± 7.1 $mm^{3)}$, and KMRC1 (13.5 ± 7.3 $mm^{3)}$. All 4 ccRCC cell lines exposed to either CXCL5 Ab or CXCR2 inhibitor for 4 days formed statistically significant smaller tumors than those received DPBS as control (**Figure 3.15.B and C**). The tumor volume of Caki1 decreased from 16.8 ± 3.9 mm^3 to 3.9 ± 3.9 mm^3 and 2.5 ± 2.2 mm^3 when treated with CXCL5 Ab and CXCR2 inhibitor, respectively. Regarding 786O, 2-fold and 6.8-fold reduction of tumor size was observed in CXCL5 Ab and CXCR2 inhibitor -treated cells compared to untreated cells. In contrast, tumor formation of NCI-H1048 was not affected by the addition of CXCL5 Ab (Control: 27.0 ± 15.2 mm^3 vs. CXCL5 Ab: 30.5 ± 3.6 mm^3). Besides, the density of capillary network surrounded drug-treated ccRCC tumors was decreased and more tortuous vessels were formed. Treatment of tumors with sunitinib or sunitinib combined with either CXCL5 Ab or CXCR2 inhibitor significantly impaired ccRCC tumor growth when compared to control.

In conclusion, the therapeutic potential of CXCL5/CXCR2 signaling pathway disruption in ccRCC was demonstrated in the CAM assay, underscoring that targeting CXCL5/CXCR2 axis is a promising approach for ccRCC treatment.

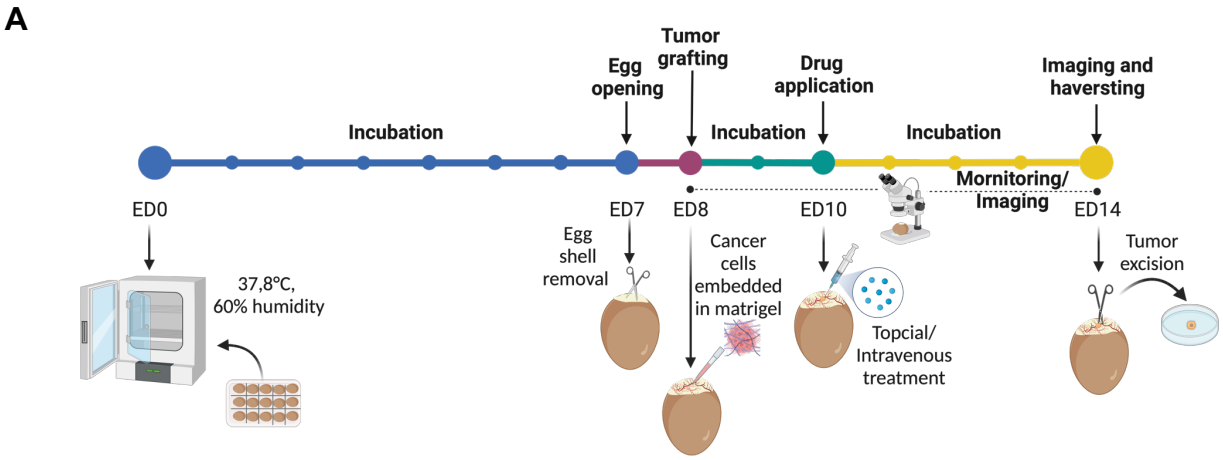
A
Egg opening
Tumor grafting
Drug application
Imaging and haversting
Incubation
Incubation
Incubation
Mornitoring/ Imaging
ED0
ED7
ED8
ED10
ED14
37,8°C, 60% humidity
Egg shell removal
Cancer cells embedded in matrigel
Topcial/ Intravenous treatment
Tumor excision

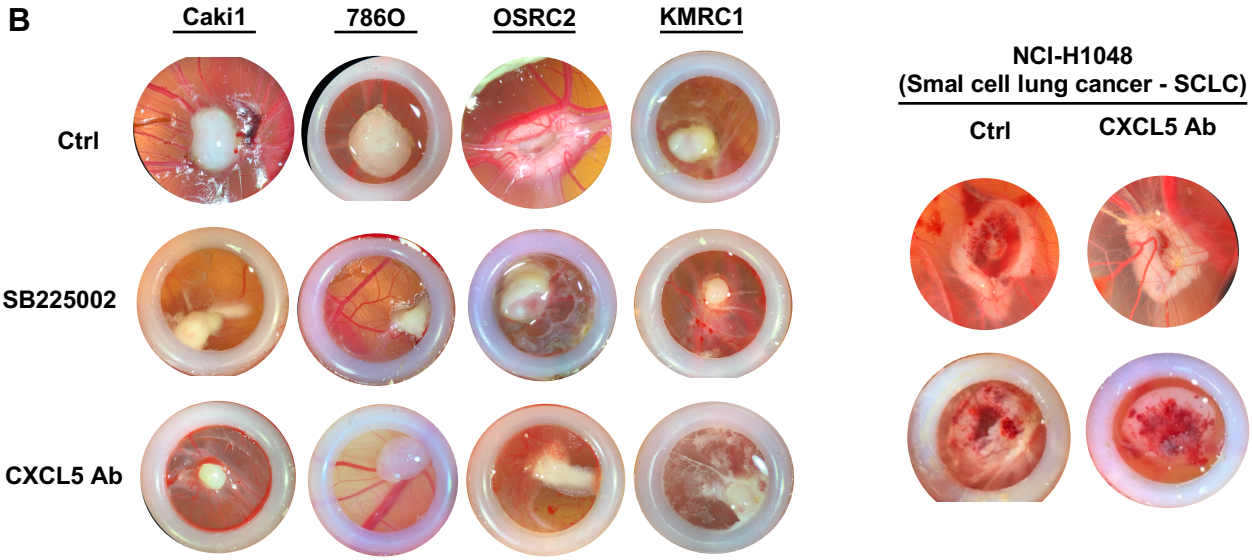
B
Caki1
786O
OSRC2
KMRC1
Ctrl
SB225002
CXCL5 Ab
NCI-H1048
(Smal cell lung cancer - SCLC)
Ctrl
CXCL5 Ab

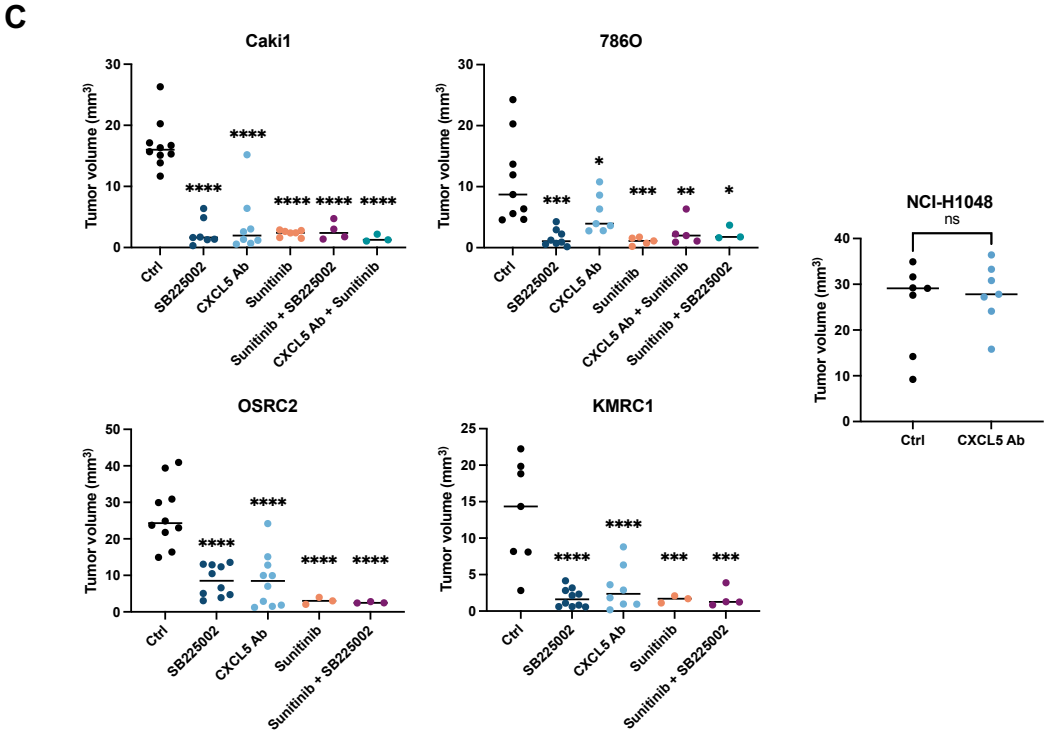
C
Caki1
786O
OSRC2
KMRC1
NCI-H1048
Tumor volume (mm3)
ns
Ctrl
SB225002
CXCL5 Ab
Sunitinib
Sunitinib + SB225002
CXCL5 Ab + Sunitinib

Figure 3.15: Disrupting CXCL5/CXCR2 axis suppresses ccRCC tumor growth on CAM assay. (A) Workflow of CAM assay experiment, which was adapted from (Sarogni et al., 2021), from embryonic day of development (ED) 0 to ED14. 7 days since the first day of incubation (ED7), part of egg shell and shell membrane are cut off to reveal the CAM. 2 to 3 million cells are engrafted the next day. 48-h post-engraftment, testing agents are implemented directly on top of the tumors. The experiment is terminated at ED14 to circumvent the ethical restriction of animal testing. (B) Representative macroscopic images of ccRCC tumors at day 6 post-implantation in in ovo xenograft CAM assay at 2X zoom factor. The inner diameter of white silicon ring is 7 mm. NCI-H1048 cell line was employed as a negative control for the specific therapeutic effects of anti-CXCL5 on ccRCC. (C) SB225002 (CXCR2 inhibitor), CXCL5 blocking antibodies and sunitinib—a standard first-line treatment for metastatic RCC—can considerably attenuate tumor progression. At least 3 eggs per condition from 2 to 3 experiments were included for statistical testing. Lines indicate the median of each group. Two-sided unpaired t-test was conducted for NCI-H1048. Statistical analyses in all ccRCC cell lines were performed with one-way ANOVA plus Dunnett's multiple comparison test. *$p < 0.05$, **$p < 0.01$, ***$p < 0.001$, ****$p < 0.0001$, ns. not significant.

4. Discussion

The discovery of elevated expression of *CXCL5* and *CXCL6* in PBRM1-pharmacologically inhibited cells and the subsequent observations of enhanced secretion of CXCL1, CXCL2, CXCL5, and CXCL8 (all CXCR2 ligands) in *PBRM1*-deleted ccRCC cells add a new dimension to our understanding of the role of *PBRM1* loss in ccRCC, specifically in terms of tumor angiogenesis. This section aims to situate our results within the broader context of current knowledge, highlighting similarities, discrepancies, and the novel insights that our study contributes.

4.1. *PBRM1* acts as a tumor suppressor gene

PBRM1 has been identified as a key tumor suppressor (following the classical two-hit model) in ccRCC. *PBRM1* loss is observed in approximately 40% of ccRCC cases, making it the second most frequently mutated gene after *VHL*. Previous studies have extensively documented the role of PBRM1 in regulating gene expression, cell cycle progression, and genome stability. PBRM1 manifests its tumor suppressor activity in breast cancer via inducing p21 expression, subsequently cell cycle arrest at the G1 phase (Xia et al., 2008). In a non-malignant breast cell line received TGFβ treatment or γ-irradiation, PBRM1 binding to the p21 promoter is crucial for p21 upregulation and G1 arrest. PBRM1-depleted primary fibroblasts have shown increased survival and delayed senescence, which is ascribed to PBRM1's contributing role in p53-mediated replicative senescence (Burrows et al., 2010). *PBRM1*-knockdown ccRCC cell lines exhibited transformed phenotypes as evidenced by enhanced soft-agar growth and migration (Varela et al., 2011). Later, Gao and colleagues used two pVHL-deficient ccRCC cell lines, A704 (without detectable PBRM1) and CRISPR-mediated-KO *PBRM1* 786O, to show that the combined loss of *VHL* and *PBRM1* significantly activates the transcription of HIF-dependent/hypoxia-dependent genes, thereby intensifying the pseudohypoxia response (Gao et al., 2017). The abrogation of PBRM1 in 786O cells accelerates tumor progression as these cells form significantly enlarged tumors in immune-deficient mice, which can be rescued by the re-expression of PBRM1. Furthermore, there has been evidence to suggest the involvement of PBRM1 in preserving genome and chromosomal integrity. Brownlee et al. showed through knocking down *PBRM1* with siRNA in mouse embryonic

stem cells, human fibroblasts, and an osteosarcoma cell line, or expressing *PBRM1* cancer-associated missense mutations in yeast that PBRM1 is crucial for maintaining centromeric sister chromatid cohesion and lack of PBRM1 culminates in chromosomal instability (Brownlee et al., 2014). PBRM1 is also essential for transcriptional silencing and subsequent DNA repair in a fraction of DNA double-strand breaks (DSBs) (Kakarougkas et al., 2014). This process is dependent on ATM kinase-mediated phosphorylation of PBRM1 and may involve PBRM1 supporting the enrichment of H2AK119 mono-ubiquitination that allows for mounting polycomb repressive machinery for transcriptional repression around DBSs. Consistently, Postel-Vinay lab reported the synthetic lethal effect of poly-(ADP-Ribose) polymerase inhibitors (PARPi)—DNA repair inhibitors—and PBRM1-deficiency in ccRCC, osteosarcoma, and NSCLC cell lines as well as in ccRCC xenograft model (Chabanon et al., 2021). Particularly, as *PBRM1*-loss ccRCC cells are more vulnerable to replication stress and DNA damage, this ramification is magnified by PARPi treatment. The accrual of R-loops and micronuclei, owing to replication stress, provokes type I IFN response with the activation of the cyclic GMP-AMP synthase/stimulator of IFN genes (cGAS/STING) pathway, and ultimately cell death. In contrast, Espana-Agusti et al. demonstrated that PBRM1 inactivation induces a global modulation of H3K9me3, consequently negating potential replication stress triggered by *VHL* loss and promoting cell division and proliferation that drives ccRCC tumorigenesis (Espana-Agusti et al., 2017). Another synthetic lethal target in PBRM1-mutant cancer cells is enhancer of zeste homolog 2 (EZH2). The addition of EZH2 inhibitor on PBRM1-deficient cells culminates in reduced trimethylation, which is catalyzed by EZH2, of H3K27 as well as increased apoptotic activity in these cells (Huang et al., 2020; Kim et al., 2015). Altogether, distinct genetic backgrounds might affect the downstream consequences of *PBRM1* deletion in cancer cells.

PBRM1 suppression has been linked to NF-κB and IFN signaling. In *VHL*-null ccRCC cells, the composition of the PBAF complex is altered following *PBRM1* loss, such that BRD7 disengages from SMARCA4, while ARID2-SMARCA4 binding is preserved (Yao et al., 2023). This is in line with another study which reported that PBAF complex assembly starts with the incorporation of ARID2 to the BAF core module, and the incomplete-PBAF complex can persist after *PBRM1* loss (Mashtalir et al., 2018). The partial-PBAF complexes anomalously reposition to distal enhancer sites from promoter proximal

regions and enhance activation of NF-κB complexes. The authors showed through RNA-sequencing that among PBRM1-deficient cells, inflammation-related gene sets, including TNFα signaling via NF-κB, IFNγ response, and IL6 via STAT3, are significantly enriched compared to controls. PBRM1 deficiency sensitizes tumour cells to NF-κB inhibitor, thereby delaying tumor growth in a xenograft model. On the other hand, Pan and colleagues first showed the depletion of *Arid2* in the B16F10 mouse melanoma cell line causes a reciprocal decline in PBRM1 and BRD7 protein abundance, while *Pbrm1* KO does not affect the protein levels of ARID2 or BRD7 (Pan et al., 2018). GSEA was used to confirm that the expression signature of IFNγ and IFNα response is positively associated with *Pbrm1*-inactivation due to the decrease of PBRM1 occupancy at promoters or enhancers of IFNγ-targeted genes detected by ATAC-seq (assay for transposase-accessible chromatin using sequencing). Additionally, Clark and co-workers holistically compared genomic, transcriptomic, and proteomic profiles between non-treated ccRCC tumors and matched adjacent normal renal tissues and observed that *PBRM1* alterations suppress the oxidative phosphorylation pathway but enhance mitogen-activated protein kinase (MAPK) signaling, focal adhesion, as well as G2-to-M cell cycle transition (Clark et al., 2019).

4.2. *PBRM1* loss induces increased expression of CXCR2-binding chemokines, thereby contributing to the pro-angiogenic phenotype of ccRCC

The positive correlation between PBRM1-deficiency and angiogenesis has been extensively reported. First, in the IMmotion150 cohort, mutated-*PBRM1* is significantly enriched in tumors that abundantly express angiogenesis-related genes (*VEGFA*, *KDR*, *ESM1*, *PECAM1*, *ANGPTL4*, and *CD34)* (McDermott et al., 2018). This association is further corroborated by the COMPARZ phase 3 trial, which compared pazopanib to sunitinib in ccRCC patients (Hakimi et al., 2019). Immunohistochemical staining of two aforementioned cohorts demonstrated that CD31-positive cells are more abundant in *PBRM1*-mutated tumors, suggesting an increase in angiogenic activity in these tumors (Hakimi et al., 2020). Moreover, an unsupervised analysis of the 10% most variably expressed genes in the RNA sequencing dataset from the IMmotion151 clinical trial identifies 7 ccRCC clusters (Motzer, et al., 2020). In particular, clusters 1 and 2 are characterized by being angiogenesis-rich, immune-poor, and having high prevalence of

PBRM1 mutations (50% of tumor samples). On the contrary, a lower mutation rate of *PBRM1* (30%) coincides with less angiogenic activity in sarcomatoid RCC tumors. In this study, patients with tumors belonging to clusters 1 and 2 experienced the most PFS benefit (PFS: ~13-15 months) compared to the other 5 clusters in both atezolizumab plus bevacizumab- and sunitinib- treated arms. The same group further validated profiles of these 7 biological subtypes and their predictive roles in the JAVELIN Renal 101 trial, which evaluated the efficacy of avelumab + axitinib versus sunitinib (Saliby et al., 2024). Specifically, *PBRM1* mutations are enriched in angiogenic cluster 1 and 2, but ORR to sunitinib is higher than the combination of avelumab and axitinib across all molecular subtypes. Moreover, the ongoing phase 2 OPTIC RCC clinical trial with two treatment arms evaluates the benefits of these molecular clusters as predictive biomarkers, which nivolumab/cabozantinib group comprises patients with cluster 1 and 2 tumor profiles and ipilimumab/nivolumab group includes patients with cluster 4 and 5 tumor profiles (Chen et al., 2023). In addition, a large-scale proteogenomic analysis of 110 ccRCC patients from the Clinical Proteomic Tumor Analysis Consortium (CPTAC) showed that the highest *PBRM1* mutation rate is detected in VEGF immune desert subtype (among four immune-based ccrRCC tumor subgroups stratified by cell type enrichment in TME) with the most abundance of EC signature and a positive correlation with patient survival (Clark et al., 2019). Although a plausible contribution of *PBRM1* loss to angiogenesis in ccRCC is the increased transcription activity of HIF-target genes, including *VEGFA*, in the *VHL*-deletion background (Gao et al., 2017), there is still no tangible result in terms of functional assay to verify the causal relationship between *PBRM1* loss and angiogenesis.

In this study, we sought to assess whether PBRM1 inactivation by pharmacological inhibition triggers alterations in transcriptomic profile that are associated with tumor pro-angiogenic activity. We found that in response to pan-SMARCA2/4-PBRM1 bromodomain inhibitors but not BDR7/9 inhibitor or degrader, *CXCL5* and *CXCL6* were among the top upregulated genes for different inhibitors. We corroborated this finding using the TCGA-KIRC data. *CXCL1*, *CXCL2*, *CXCL3*, and *CXCL5* were significantly expressed in ccRCC tumors harbored *PBRM1* mutations compared with the non-mutated *PBRM1* tumors. To confirm the increased expression of CXCR2-binding chemokines is specific to PBRM1 but not SMARCA2/4 inhibition, we employed the CRISPR-Cas9 technology for *PBRM1* gene disruption in Caki1 and 786O ccRCC cell lines. We identified ccRCC cells deficient

in *PBRM1* secreted larger amounts of CXCR2-activating chemokines, including CXCL1, CXCL2, CXCL5, CXCL6 (only for Caki1), and CXCL8, which are necessary for the proliferation and sprouting capability of ECs compared to controls. The production of these cytokines was magnified by TNFα and IL17A stimulation in both *PBRM1*-mutated and WT cells, while PBRM1-deficient cells still surpassed PBRM1-proficient cells in releasing CXCR2 ligands.

4.3. *PBRM1* loss reprograms the TME through paracrine effects

Previous research has suggested that *PBRM1* loss modulates the TME by regulating the expression of various chemokines, although the specific pathways involved have remained ambiguous. For instance, the addition of IFNγ significantly stimulates the secretion of CXCL9 and CXCL10—major chemokines for promoting tumor infiltration of effector T cells—as well as surface expression of PD-L1 in *PBRM1*-defect not *PBRM1*-proficient tumor cells, which might explain the clinical observations that loss-of-function mutations in *PBRM1* are associated with better survival upon anti-PD-(L)1 therapy in ccRCC patients (Braun et al., 2019; Miao et al., 2018). Contentiously, Liu et al. demonstrated that PBRM1 deficiency cells in response to IFNγ treatment attenuate the JAK1/STAT1/IRF-1 signaling pathway, consequently the reduction of CXCL9 secretion and the recruitment of effector T cells (Liu et al., 2020). The authors further analyzed transcriptional profiles of patients from three RCC cohorts, including TCGA-KIRC, IMmotion150, and International Cancer Genome Consortium (ICGC), to demonstrate that gene sets which are depleted in PBRM1-mutant tumors are associated with a highly immunogenic TME. They also found that *Pbrm1* defects result in ICB resistance following anti-PD-1 and anti-CTLA-4 therapy in mice, consistent with reports that RCC patients, from IMmotion150 and MSKCC IMPACT cohorts, with mutated-*PBRM1* experienced shortened survival following ICB therapy. In addition, *PBRM1*-loss-induced upregulation of chemokine ligand 5 (CCL5) fosters ccRCC tumor infiltration by mast cells in vitro (Liu et al., 2020). It is worth highlighting that the deficiency of *Arid1a*—a subunit of canonical SWI/SNF complex—in castration-resistant prostate cancer (CRPC) murine Myc-CaP cells are more responsive to TNFα in mouse model, which in turn triggers the activation of NF-κB pathway resulting in the significant release of CXCL2 and CXCL3 in peripheral blood and prostate tumors (Li et al., 2022). Furthermore, the intratumoral levels of ARID1A

positively correlate with recurrence-free survival of prostate cancer patients, but inversely associate with the intratumoral concentration of CXCL2 and CXCL3.

The hyper-induction of CXCR2-activating chemokines by IL17A and TNFα has been described previously. TNFα is secreted by various cell types in the TME, including tumor-associated myeloid cells, CD4+ T cells, cancer-associated fibroblasts, and tumor cells (de Visser & Joyce, 2023), while IL17A is released predominantly by T helper 17 cells, and to a lesser extent by γδ T cells, NK cells, NK T cells, mast cells, granulocytes, IL17A-producing $CD8^+$ T cells—Tc17 cells, innate lymphoid cells, and cancer cells (Mills, 2023). Analysis of 46 RCC tumor cultured supernatants and 33 plasma samples showed that IL17A and TNFα are among the top pro-inflammatory cytokines expressed by tumor cells and in circulatory system (Lee et al., 2022). Autocrine TNFα production by IGROV-1 human breast cancer cell line provokes the secretion of CCL2, CXCL12, VEGF, IL6, and MIF (macrophage migration-inhibitory factor), while the knockdown of TNFα in IGROV-1 cells dampens the release of these pro-inflammatory agents, as well as tumor growth, and tumor angiogenesis in a xenograft mouse model (Kulbe et al., 2007). IL17A can act synergistically with TNFα to induce the secretion of CXCL1, CXCL2, and CXCL5 by alveolar epithelial type II cells, thereby supporting sustained inundation of neutrophils in the lung in mouse model (Liu et al., 2011). Interestingly, these cells secrete CXCL5 in a polarized fashion, which CXCL5 is apically or both apically and basolaterally released when IL17A and TNFα are added apically or basolaterally respectively, implying that neutrophils are recruited to the specific site of initial injury to induce wound healing (including neoangiogenesis). Costimulation of IL17A and TNFα on ECs triggers the same ramifications: the increased production of CXCL1, CXCL2, and CXCL5 and the sustained neutrophil transendothelial migration in vitro (Griffin et al., 2012).

4.4. CXCR2-activating chemokines and their pro-tumorigenic properties

Chemokines, a family of small bioactive substances with a molecular weight of 7-12 kDa, are chemotactic cytokines, because they were originally recognized for their ability to induce the trafficking of leukocytes (Hughes & Nibbs, 2018). Chemokines are subdivided into four groups based on the position of the conserved cysteines closest to the N-terminus, including CXC, CC, C, and CX_3C, which ‘X’ designate any amino acid. In human, there are 17 ligands for CXC chemokine family, denoted as CXCL, that bind overlappingly

to 8 CXC chemokine receptors, designated as CXCR. CXCR1-8 (except CXCR7) are all members of the rhodopsin-like seven-transmembrane G protein-coupled receptor family. CXCR7 is an atypical chemokine receptor which acts as a scavenger. Depending on the existence of glutamic acid-leucine-arginine (ELR motif) preceding the first cysteine residue, CXC chemokines can be further classified into two subtypes—ELR^+ or ELR^- CXC chemokines. ELR^+ CXC chemokine subfamily comprises CXC ligand 1 (CXCL1) (growth-related oncogene-α—GROα), CXCL2 (GROβ), CXCL3 (GROγ), CXCL5 (epithelial neutrophil-activating peptide-78—ENA78), CXCL6 (granulocyte chemotactic protein-2—GCP2), CXCL7 (neutrophil-activating peptide-2—NAP2), and CXCL8 (interleukin-8—IL-8). ELR^- CXC chemokine subfamily consists of CXCL4 (platelet factor-4—PF4), CXCL9 (monokine induced by IFNγ—MIG), CXCL10 (IFNγ-inducible protein-10—IP10), CXCL11 (IFNγ-inducible T-cell a chemoattractant—I-TAC), CXCL12 (stromal derived factor-1—SDF1), CXCL13 (B-cell chemoattractant-1—BCA1), and CXCL14 (breast and kidney-expressed chemokine—BRAK). ELR^+ CXC members are primarily involved in neutrophil migration and are potent inducers of angiogenesis, whereas ELR^- CXC chemokines exert their chemoattractant effects mainly on lymphocytes and are generally angiostatic (except CXCL12) (Mehrad et al., 2007; Mukaida et al., 2014). While all angiogenic chemokines bind to CXCR2, CXCL6 and CXCL8 are two known ligands of CXCR1. Both receptors are detected on both immune and non-immune cells, for example neutrophils, macrophages, epithelial and endothelial cells. Although ECs express CXCR1 and CXCR2 simultaneously, CXCR2 is primarily responsible for angiogenesis owing to the fact that endothelial chemotaxis is not impaired in the presence of both CXCL8 and CXCR1 Ab (Addison et al., 2000).

The CXCLs/CXCR2 signaling pathways actively participate in tumor progression, stemness, metastasis, angiogenesis, and modification of the immune landscape by controlling the infiltration of different immune cell subsets into tumours, which in turn determines the sensitivity to chemo- and immuno- therapies. Van Coillie and co-workers showed that tumors formed by CXCL6-overexpressed human Bowes melanoma cells in mouse model are highly infiltrated by neutrophils and are extensively vascularized (Van Coillie et al., 2001). In a preclinical mouse model of lung cancer, elevated CXCL1, and CXCL2/3 expression has been detected and CXCR2 is primarily expressed by intratumoral ECs (Keane et al., 2004). Genetical ablation of *Cxcr2* improves OS of the

mice by triggering tumor necrosis and impeding intratumoral neovascularization which is confirmed by decreasing number of blood vessel and number of von Willebrand Factor-positive cells. In several skin and intestine mouse models, CXCR2 is activated by CXCL1, CXCL2, CXCL5, and/or CXCL7 secreted by stromal and tumor cells, which drives the intratumoral accumulation of pro-tumorigenic neutrophils (Jamieson et al., 2012). Deletion of *Cxcr2* substantially inhibits inflammation-driven and spontaneous tumor formation, along with the reduction of intratumoral microvessel density. Exposure of either paclitaxel or doxorubicin to aggressive MDA-MB-231 and MDA-MET breast cancer cells results in the surge of CXCL1 and CXCL8 secretion and the upregulation of CXCR2 gene expression (Sharma et al., 2013). *Cxcr2*-silencing in murine CI66 mammary adenocarcinoma cells attenuates paclitaxel-resistance as well as metastatic rates to the lung. CXCR2 signalling has been shown to confer pancreatic cancer cells with resistance to immunotherapy (Steele et al., 2016). In the KPC pancreatic mouse models, *Cxcl1*, *Cxcl2*, and *Cxcl5* are transcriptionally upregulated in tumor cells, while *Cxcr2* is significantly expressed by Ly6G-positive stromal cells, including neutrophils and myeloid-derived suppressor cells (MDSCs). The virtual abolition of metastasis, the diminution of tumor-infiltrated neutrophils, and the enhanced infiltration of CD3-positive T cells in this model are achieved by either homozygous deletion of *Cxcr2* or elimination of Ly6G-positive cell using Ly6G Ab. Given that pancreatic tumor in the KPC model is intrinsically refractory to anti-PD-1/CTLA4 therapies, the combination of PD-1 Ab and CXCR2 inhibitor substantially sustains the survival of KPC mice, accompanied by the intratumoral expansion of $CD4^+$ and $CD8^+$ T cells but the intratumoral contraction of inhibitory regulatory T cell population. In line with this, inhibition of CXCR2 signaling using AZ10397767 enhances PD-1 Ab antitumour activity in an in vivo non-alcoholic steatohepatitis hepatocellular carcinoma (Leslie et al., 2022). The authors reported that $CD8^+$ T cell recruitment is a prerequisite for the efficacy of CXCR2 inhibitor plus anti-PD-1 therapy, and the administration of this combination leads to the repolarization of tumor-associated neutrophils (TANs) from pro-tumor to anti-tumor phenotype.

4.5. CXCR2-binding chemokines are secreted by ccRCC cells to support the vasculature formation and the recruitment of myeloid cells

Our data not only support other studies linking CXCR2-activating ligands and tumor angiogenesis but also provide additional evidence for the high-angiogenic phenotype in *PBRM1*-mutated ccRCC tumors induced by the CXCL5-CXCR2 axis. The secretome of PBRM1-deficient ccRCC cell substantially perpetuates the proliferation of HUVECs in CXCLs/CXCR2-dependent manner, as the addition of CXCR2 inhibitor suppressed this paracrine effect. Importantly, the tumor-suppressive potency of CXCR2 inhibitor is comparable to sunitinib, a current standard of care for mRCC, which highlights its potential for clinical translation.

Previously, CXCL1, CXCL3, CXCL5, and CXCL8 are found to be elevated in the plasma of mRCC patients relative to healthy controls and are expressed within tumor tissues as detected by immunohistochemical staining (Mestas et al., 2005). The murine syngeneic renal adenocarcinoma (Renca) model is employed to show the positive correlation between RCC tumor size and the combined levels of CXCL1 and CXCL2 within tumors. In agreement with this, complete abrogation of *Cxcr2* in mice delays Renca tumor growth, contemporaneously with the depletion of tumor-associated ECs, the decreased concentration of intratumoral CXCL1 and CXCL2, and the augmentation of tumor necrosis. Recently, Giuliano et al. showed that chronic exposure of 786O cell lines to sunitinib significantly induces the transcriptional expression of *IL6*, *CXCL2*, *CXCL5*, and *CXCL8*, which is mediated by the activation of the MAPK-p38, and subsequently the NF-κB pathway (Giuliano et al., 2019). The authors further used the TCGA-KIRC and their independent sunitinib-treated RCC cohorts to exhibit that patients with low *CXCL5* mRNA levels had better prognosis in terms of DFS, PFS, and OS. The same group developed an in-house selective CXCR2 inhibitor, which demonstrated its antitumor effects in RCC both in vitro and in vivo (Montemagno et al., 2024). Particularly, the CXCR2 inhibitor synergized with ICBs to promote tumor regression in Renca mouse model. The CXCR2-inhibitor-treated tumors showed decrease of vessel density as well as changes of TME cellular components: diminish of immuosuppressive cells—M2-like tumor-associated macrophages (TAMs) and TANs, but elevation of cells mediated-antitumor activities, such as M1-like TAMs, activated dendritic cells, activated NK cells, and activated $CD4^+$ T cells, consistent with previous observations in rhabdomyosarcoma (Highfill et al., 2014). CXCL5

and CXCL8 have been shown to instigate MDSC chemotaxis to RCC parenchyma, and PMN-MDSC in the periphery of patients with RCC also correlated with increasing tumor grade (Najjar et al., 2017). Furthermore, neutrophils along with MDSC can additionally contribute to tumor angiogenesis through their secretion of various angiogenic factors (Tazzyman et al., 2009; Vetsika et al., 2019). Besides, some research groups capitalized on the abundance of CXCR2-activating chemokines in the TME of solid tumor; they genetically introduced CXCR2 to NK cells and chimeric antigen receptors (CAR) T cells to improve the homing of these cells towards tumor sites, thereby inducing more robust antitumor activity (Jin et al., 2019; Kremer et al., 2017).

4.6. GSK-3β signaling in HUVEC is highly activated by the secretome of *PBRM1*-deleted ccRCC cells in CXCR2-dependent manner

Here, we showed that CXCR2 signaling in the ECs is dramatically activated in *PBRM1*-mutated ccRCC and is angiogenic promoting through GSK-3β signaling pathway. The CXCL5/CXCR2/GSK-3β axis has been reported to instigate the epithelial-mesenchymal transition in nasopharyngeal carcinoma and colorectal cancer cells (Qiu et al., 2018; Zhao et al., 2015). There have been to our knowledge no reports showing the contributing role of CXCLs/CXCR2/GSK-3β signaling cascade in tumor angiogenesis.

GSK3 is a serine/threonine protein kinase involved in diverse cellular processes, including glycogen metabolism, protein synthesis, cell proliferation, and survival. In mammals, GSK3 exists in two distinct and functional-redundant isoforms: GSK-3α and GSK-3β. While GSK3β is constitutively activated through the phosphorylation at tyrosine 216 (Y216) site to act as negative modulator, phosphorylation at S9 site by other kinases, including ribosomal S6 kinases (p90RSK and p70S6K), protein kinase A (PKA), and AKT, culminates in the inhibition of GSK-3β activity (Bhat et al., 2000; McCubrey et al., 2017). Growing evidence supports the suppressive role of GSK3β in the regulation of angiogenesis, influencing both EC behavior and vascular growth through various signaling pathways. Kim and colleagues employed HUVECs overexpressing S9-nonphosphorylatable constitutively active GSK-3β to demonstrate that the activation of GSK3β restrains HUVEC migration towards proangiogenic factors such as VEGF and basic FGF, and suppresses the formation of capillaries in in vivo Matrigel plug assay (Kim et al., 2002). Conversely, the overexpression of catalytically inactive GSK-3β in HUVECs

leads to the suppression of GSK-3β signaling, thereby promoting EC survival and enhancing angiogenic processes. In glioma, the phosphorylation state at S9 of GSK-3β is correlated with glioma progression (Zhao et al., 2015). Glioma tumors formed by overexpressing GSK3β human glioma cells are significantly smaller as well as are less vascularized than control tumors in xenograft mouse models**.** This effect is mediated through the inhibition of pathways involving mTOR and HIF1α, which are crucial for VEGF expression and subsequent angiogenic response.

4.7. CXCR2-binding chemokines derived from ccRCC cells stimulate sprouting angiogenesis

The 3D spheroid sprouting assay was instrumental in demonstrating the functional ramifications of ccRCC-derived CXCR2-binding ligands on ECs. In particular, the human ECs first grow in spheroid form, which are then sandwiched between layers of collagen matrix. The capillaries originating from the spheroids are formed after the addition of pro-angiogenic factors. This assay better mimics in vivo angiogenesis than the widely-used tube formation assay. While standard 2D cultures fail to maintain the differentiated phenotype of ECs, ECs at the surface of the spheroids maintain the quiescent state seen in vivo, strongly connect to each other for direct cell-cell signaling, and significantly express differentiated marker CD34 following the exposure to pro-angiogenic factors given that CD34 is an important inducer of angiogenesis (Korff & Augustin, 1998; Siemerink et al., 2012). Furthermore, in vivo sprouting requires the degradation of surrounding matrix by EC upon pro-angiogenic stimulation, thus allowing EC invasion. This process is fully replicated in the spheroid sprouting assay. Additionally, not only ECs are able to form capillary-like architectures but also fibroblasts, prostate carcinoma and glioblastoma cells can form cord-like structures in 2D Matrigel assay (Staton et al., 2009). We showed that angiogenic sprouting in the 3D artificial system was more pronounced in HUVEC-spheroids which were incubated for 24 hours with supernatant from *PBRM1*-loss cells than the control cells. The proangiogenic effects of *PBRM1*-loss tumors were remarkably offset by the disruption of CXCL5/CXCR2 signaling in comparison to PBRM1-WT tumors. In congruence with our findings, Liu and colleagues elucidated that supernatant from *PBRM1*-knockdown in ccRCC cells boosts the tube formation by HUVECs, implying increased angiogenic activity (Liu et al., 2020).

4.8. The inhibition of CXCR2 suppresses tumor growth in ovo in CXCR2-sensitive manner

Innumerable animals, such as rats, pigs, horses, rabbits, dogs, non-human primates, and especially mice, involve in preclinical drug testing. Though these animal models remain the primary tool for mimicking tumor development in human, examining drug-target expression, and monitoring the pharmacokinetic and pharmacodynamic of testing agents, they suffer from the cumbersome administrative and maintaining tasks of animal housing units, high costs, complicated animal-handling, as well as lengthy experimental time due to considerable time for tumor development. Additionally, all animal experimentation requires ethical approval of animal testing and can only be performed by researchers who are licensed for animal testing (FELASA certificate here in Europe) which imposes further restraints on experiment accessibility. In light of the aforementioned limitations and the 3R principle (Replacement, Reduction and Refinement) to constrain animal suffering, CAM assay has emerged as an alternative in vivo methodology to investigate multiple aspects of cancer—tumor growth, angiogenesis, and metastasis—as well as a platform for drug screening and testing (Fischer et al., 2022; Schneider-Stock & Ribatti, 2021). The fusion of the chorion and the allantois forms the double layer membrane, namely the CAM, which is enriched with vasculature network and surrounds chick embryo (Marshall et al., 2020). The chick innate immune system, comprising embryonic macrophages and heterophils (mammalian neutrophil-like cells), begins to develop from ED3, and continues to form until ED16, whilst the time frame for adaptive immune system to develop is from ED10 to ED18 (Chu et al., 2022). This immature immune system before ED18 culminates in high biocompatibility for high rate of tumor engraftment. It is noteworthy that the chick embryo does not have the capability to experience pain prior to ED14; consequently, ethical approval is not necessarily required provided that the CAM assay is concluded at ED14 (Miebach et al., 2022). Several potential drawbacks should be taken into account for this model including the discrepancy in metabolism and immune system between avian and mammalian species, the tumor and stromal cell interaction, and the scarcity of antibodies, cytokines, and growth factors that are specific to chicken cells and tissues (Schneider-Stock & Ribatti, 2021). Despite the difference in in ovo growth rate, all four ccRCC cell lines used in this study formed tumors on the CAM of chicken embryos in CXCL5/CXCR2-dependent manner after 6 days of implantation. Previously, Fergelot and co-wokers

reported the successful engraftment and tumor growth of 786O cells but not RCC4 and Caki2 cells on CAM (Fergelot et al., 2013). They further used microarray to detect differentially expressed genes between day 3 and day 7 post-engraftment. Interestingly, *CXCL1*, *CXCL2*, *CXCL3*, and *CXCL8* are significantly upregulated at day 7, which might explain the observed accumulation of chicken leukocyte-like heterophiles in the tumor stroma. Our findings are supported by another study identifying the therapeutic potential of SB225002, the CXCR2 inhibitor used in the current study, in suppressing 786O tumor growth and vessel formation in a nude mice model (Grépin et al., 2014). Of note, not only does CXCR2 antagonist arrest angiogenesis, it also alleviates immunosuppression in the TME by reducing the accumulation of tumour-associated leukocytes and macrophages (Li et al., 2016; Wu et al., 2015). Given that TAMs are one of the most populous cell types in the RCC TME (Chevrier et al., 2017), this approach may augment the efficacy of ICBs in RCC therapy.

The experimental findings raised in the above discussion signify the potential significance of the CXCLs/CXCR2 axis in ccRCC treatment, particularly in enhancing the efficacy of existing therapies and addressing issues related to TKI- and immuno- therapy resistance. Indeed, several clinical trials are currently investigating the efficacy of CXCR2 inhibitors in combination with various treatment modalities across different cancer types. For example, in a phase 2 basket trial (NCT03473925), the CXCR2 antagonist navarixin was administered alongside pembrolizumab to patients with advanced or metastatic microsatellite-stable colorectal cancer (MSS CRC), CRPC, or NSCLC (Armstrong et al., 2024). The combination efficacy was strikingly low with 0-5% ORR across three tumor entities, culminating in the premature termination of this trial. The authors of this trial as well as Lazennec and colleagues suggested some explanations regarding the lack of efficacy of CXCR2 antagonist, including functional variety of CXCR2 signaling in different cell types, functional redundancy between CXCR1 and CXCR2, rapid internalization of CXCR2 upon ligand binding, and phenotypic diversity of neutrophils and MDSCs in the TME (Lazennec et al., 2024). On the other hand, the tolerability and efficacy of CXCR2 inhibitor AZD5069 combined with enzalutamide, an androgen receptor inhibitor, are being investigated in metastatic CRPC patients who previously received a median six lines of therapy (NCT03177187) (Guo et al., 2023). In the preliminary analysis, 5/21 evaluable patients achieved partial response to AZD5069 + enzalutamide, which resulted also in

decreased circulating neutrophil levels and reduced infiltration of immunosuppressive myeloid cells. The combination was tolerable as no dose-limiting toxicity (DLT) and no permanent ceasing of medication were reported. The depletion of peripheral blood neutrophils as well as intratumoral-inflitrated MDSCs upon AZD5069 treatment suggests the mechanism of action of this drug. Another ongoing phase 1/2 clinical trial evaluates the safety and therapeutic benefit of AZD5069 plus durvalumab (anti-PD-L1 Ab) in advanced hepatocellular carcinoma (Evans et al., 2023). Biomarker studies are included to determine the mechanism of action of the drug and patient response. To sum up, while some trials have faced challenges regarding efficacy, they provide valuable insights into safety profiles and mechanisms that could inform future research directions. Forthcoming investigation will be crucial for determining optimal treatment strategies that leverage the CXCLs/CXCR2 pathway for improved patient outcomes.

In conclusion, in the context of ccRCC, the role of CXCR2 ligands in angiogenesis has been less explored. However, ccRCC is known for its highly vascular nature, driven largely by the dysregulation of the HIF pathway due to *VHL* loss in roughly 90% of ccRCC cases. CXCR2-mediated paracrine signaling between ccRCC cells and ECs sustained EC proliferation and sprouting angiogenesis which were intensified by the loss of *PBRM1*, as demonstrated in our study, suggests that CXCR2-binding chemokines may act synergistically with the HIF pathway to exaggerate angiogenesis. In the in ovo xenograft CAM assay, we showed the delayed growth of ccRCC tumor by the application of CXCR2 antagonist. As only 30-50% of ccRCC patients experience partial or complete response from anti-VEGF/TKI monotherapies, our study provides the framework for new opportunities in RCC drug development focusing on the CXCLs/CXCR2 axis and employing *PBRM1* mutations as predictive biomarker.

5. Abstract

Immune checkpoint blockade (ICB) and anti-angiogenic tyrosine kinase inhibitors (TKI) have substantially improved the outcomes of metastatic clear cell renal cell carcinoma (ccRCC). Nevertheless, the anti-angiogenic TKIs targeting the VEGF/ VEGFR axis result only in temporary antitumor response, and most ccRCCs become ultimately TKI-resistant. Mutations of polybromo-1 (*PBRM1*) occur in about one-third of ccRCC. It is well known that *PBRM1*-mutated tumors are highly vascularized. This project aims to dissect the molecular mechanism driving the proangiogenic phenotype of *PBRM1*-mutated ccRCC. In an unbiased approach, pharmacological inhibition of PBRM1 in ccRCC cell line leads to strong upregulation of the CXCR2 ligands *CXCL5* and *CXCL6*. Accordingly, our TCGA in silico analysis revealed that *PBRM1*-mutant ccRCC exhibited enhanced *CXCL1*, *CXCL2*, *CXCL3*, and *CXCL5* expression; furthermore, patients who had high CXCL5 mRNA expression are associated with worse prognosis in TCGA-KIRC. We established CRISPR-Cas9 induced polyclonal *PBRM1*-knockouts in the ccRCC cell lines 786O and Caki1. We also identified elevated secretion of CXCL1, CXCL2, CXCL5, CXCL6, and CXCL8, all CXCR2-activating chemokines in *PBRM1*-loss cell lines. Exposing the cells to pro-inflammatory cytokines (TNFα, and IL-17A) leads to hyper-induction of these chemokines. *PBRM1*-KO conditioned-media (CM) significantly promoted HUVECs viability and culminated in the enhanced phosphorylation of GSK-3β compared to *PBRM1*-wild-type CM. The addition of CXCR2 blockade to ccRCC not only suppressed the inhibition of GSK3β signaling, but also the proliferation of HUVECs. The association between PBRM1-deficiency and an enhanced tumor angiogenesis was recapitulated using the spheroid sprouting assay, a three-dimensional (3D) in vitro angiogenic model. Augmented angiogenic sprouting was detected in HUVEC-spheroids which were incubated with supernatant from *PBRM1*-loss cells. CXCL5 was identified as one of the drivers of the pro-angiogenic phenotype of *PBRM1*-mutated tumors. Of note, enhanced sprouting capacity of the supernatant of *PBRM1*-KO ccRCC cell lines can be selectively suppressed by CXCR2 inhibitor and CXLC5 blocking antibody. The therapeutic potential of CXCL5/CXCR2 signaling pathway disruption in ccRCC were shown in the CAM assay, underscoring that targeting CXCL5/CXCR2 axis is a promising approach for ccRCC treatment, specifically in *PBRM1*-defective ccRCC.

6. List of figures

7. List of tables

8. References

Addison, C. L., Daniel, T. O., Burdick, M. D., Liu, H., Ehlert, J. E., Xue, Y. Y., Buechi, L., Walz, A., Richmond, A., & Strieter, R. M. (2000). The CXC chemokine receptor 2, CXCR2, is the putative receptor for ELR+ CXC chemokine-induced angiogenic activity. *J Immunol*, *165*(9), 5269-5277. https://doi.org/10.4049/jimmunol.165.9.5269

Ahlmann-Eltze, C., Patil, I. (2022). ggsignif: R Package for Displaying Significance Brackets for 'ggplot2'. R package version 0.6.4. In https://psyarxiv.com/7awm6.

Armstrong, A. J., Geva, R., Chung, H. C., Lemech, C., Miller, W. H., Jr., Hansen, A. R., Lee, J. S., Tsai, F., Solomon, B. J., Kim, T. M., Rolfo, C., Giranda, V., Ren, Y., Liu, F., Kandala, B., Freshwater, T., & Wang, J. S. (2024). CXCR2 antagonist navarixin in combination with pembrolizumab in select advanced solid tumors: a phase 2 randomized trial. *Invest New Drugs*, *42*(1), 145-159. https://doi.org/10.1007/s10637-023-01410-2

Barnes, B., Buttmann-Schweiger, N., Dahm, S., Franke, M., Schönfeld, I., Kraywinkel, K., Wienecke, A. (2024). Cancer in Germany 2019/2020. 14th edition. Robert Koch Institute (ed.) and the Association of Population-based Cancer Registries in Germany (ed.). Available from: https://www.krebsdaten.de/Krebs/EN/Content/Publications/Cancer_in_Germany/cancer_in_germany.html

Bergers, G., & Benjamin, L. E. (2003). Tumorigenesis and the angiogenic switch. *Nature Reviews Cancer*, *3*(6), 401-410. https://doi.org/10.1038/nrc1093

Bhat, R. V., Shanley, J., Correll, M. P., Fieles, W. E., Keith, R. A., Scott, C. W., & Lee, C. M. (2000). Regulation and localization of tyrosine216 phosphorylation of glycogen synthase kinase-3beta in cellular and animal models of neuronal degeneration. *Proc Natl Acad Sci U S A*, *97*(20), 11074-11079. https://doi.org/10.1073/pnas.190297597

Blighe, K., Rana, S., & Lewis, M. (2023). EnhancedVolcano: Publication-ready volcano plots with enhanced colouring and labeling. R package version 1.22.0. In https://bioconductor.org/packages/EnhancedVolcano.

Braun, D. A., Hou, Y., Bakouny, Z., Ficial, M., Sant' Angelo, M., Forman, J., Ross-Macdonald, P., Berger, A. C., Jegede, O. A., Elagina, L., Steinharter, J., Sun, M., Wind-Rotolo, M., Pignon, J.-C., Cherniack, A. D., Lichtenstein, L., Neuberg, D., Catalano, P., Freeman, G. J., . . . Choueiri, T. K. (2020). Interplay of somatic alterations and immune infiltration modulates response to PD-1 blockade in advanced clear cell renal cell carcinoma. *Nature Medicine*, *26*(6), 909-918. https://doi.org/10.1038/s41591-020-0839-y

Braun, D. A., Ishii, Y., Walsh, A. M., Van Allen, E. M., Wu, C. J., Shukla, S. A., & Choueiri, T. K. (2019). Clinical Validation of PBRM1 Alterations as a Marker of Immune Checkpoint Inhibitor Response in Renal Cell Carcinoma. *JAMA Oncology*, *5*(11), 1631-1633. https://doi.org/10.1001/jamaoncol.2019.3158

Bray, F., Laversanne, M., Sung, H., Ferlay, J., Siegel, R. L., Soerjomataram, I., & Jemal, A. (2024). Global cancer statistics 2022: GLOBOCAN estimates of incidence and mortality worldwide for 36 cancers in 185 countries. *CA: A Cancer Journal for Clinicians*, *74*(3), 229-263. https://doi.org/https://doi.org/10.3322/caac.21834

Brodaczewska, K. K., Szczylik, C., Fiedorowicz, M., Porta, C., & Czarnecka, A. M. (2016). Choosing the right cell line for renal cell cancer research. *Molecular Cancer*, *15*(1), 83. https://doi.org/10.1186/s12943-016-0565-8

Brownlee, P. M., Chambers, A. L., Cloney, R., Bianchi, A., & Downs, J. A. (2014). BAF180 promotes cohesion and prevents genome instability and aneuploidy. *Cell Rep*, *6*(6), 973-981. https://doi.org/10.1016/j.celrep.2014.02.012

Bruno Miguel, L.-B., Wen G, J., & Jun, C. A. I. (2016). Tumour–Endothelial Cell Communications: Important and Indispensable Mediators of Tumour Angiogenesis. *Anticancer Research*, *36*(3), 1119. http://ar.iiarjournals.org/content/36/3/1119.abstract

Burrows, A. E., Smogorzewska, A., & Elledge, S. J. (2010). Polybromo-associated BRG1-associated factor components BRD7 and BAF180 are critical regulators of p53 required for induction of replicative senescence. *Proc Natl Acad Sci U S A*, *107*(32), 14280-14285. https://doi.org/10.1073/pnas.1009559107

Caduff, J. H., Fischer, L. C., & Burri, P. H. (1986). Scanning electron microscope study of the developing microvasculature in the postnatal rat lung. *Anat Rec*, *216*(2), 154-164. https://doi.org/10.1002/ar.1092160207

Cai, W., Su, L., Liao, L., Liu, Z. Z., Langbein, L., Dulaimi, E., Testa, J. R., Uzzo, R. G., Zhong, Z., Jiang, W., Yan, Q., Zhang, Q., & Yang, H. (2019). PBRM1 acts as a p53 lysine-acetylation reader to suppress renal tumor growth. *Nature Communications*, *10*(1), 5800. https://doi.org/10.1038/s41467-019-13608-1

Carmeliet, P., & Jain, R. K. (2011). Molecular mechanisms and clinical applications of angiogenesis. *Nature*, *473*(7347), 298-307. https://doi.org/10.1038/nature10144

Chabanon, R. M., Morel, D., Eychenne, T., Colmet-Daage, L., Bajrami, I., Dorvault, N., Garrido, M., Meisenberg, C., Lamb, A., Ngo, C., Hopkins, S. R., Roumeliotis, T. I., Jouny, S., Hénon, C., Kawai-Kawachi, A., Astier, C., Konde, A., Del Nery, E., Massard, C., . . . Postel-Vinay, S. (2021). PBRM1 Deficiency Confers Synthetic Lethality to DNA Repair Inhibitors in Cancer. *Cancer Research*, *81*(11), 2888-2902. https://doi.org/10.1158/0008-5472.Can-21-0628

Chambers, S. E. J., Pathak, V., Pedrini, E., Soret, L., Gendron, N., Guerin, C. L., Stitt, A. W., Smadja, D. M., & Medina, R. J. (2021). Current concepts on endothelial stem cells definition, location, and markers. *Stem Cells Transl Med*, *10 Suppl 2*(Suppl 2), S54-s61. https://doi.org/10.1002/sctm.21-0022

Chen, Y.-W., Beckermann, K., Haake, S. M., Reddy, A., Shyr, Y., Atkins, M. B., Mar, N., Ornstein, M. C., Pal, S. M., Zhang, T., Rathmell, W. K., & Rini, B. I. (2023). Optimal treatment by invoking biologic clusters in renal cell carcinoma (OPTIC RCC). *Journal of Clinical Oncology*, *41*(6_suppl), TPS742-TPS742. https://doi.org/10.1200/JCO.2023.41.6_suppl.TPS742

Cheng, Y., Ma, X.-l., Wei, Y.-q., & Wei, X.-W. (2019). Potential roles and targeted therapy of the CXCLs/CXCR2 axis in cancer and inflammatory diseases. *Biochimica et Biophysica Acta (BBA) - Reviews on Cancer*, *1871*(2), 289-312. https://doi.org/https://doi.org/10.1016/j.bbcan.2019.01.005

Chevrier, S., Levine, J. H., Zanotelli, V. R. T., Silina, K., Schulz, D., Bacac, M., Ries, C. H., Ailles, L., Jewett, M. A. S., Moch, H., van den Broek, M., Beisel, C., Stadler, M. B., Gedye, C., Reis, B., Pe'er, D., & Bodenmiller, B. (2017). An Immune Atlas of Clear Cell Renal Cell Carcinoma. *Cell*, *169*(4), 736-749 e718. https://doi.org/10.1016/j.cell.2017.04.016

Cho, H., Du, X., Rizzi, J. P., Liberzon, E., Chakraborty, A. A., Gao, W., Carvo, I., Signoretti, S., Bruick, R. K., Josey, J. A., Wallace, E. M., & Kaelin, W. G. (2016). On-target efficacy of a HIF-2α antagonist in preclinical kidney cancer models. *Nature*, *539*(7627), 107-111. https://doi.org/10.1038/nature19795

Choueiri, T. K., Powles, T., Peltola, K., Velasco, G. d., Burotto, M., Suarez, C., Ghatalia, P., Iacovelli, R., Lam, E. T., Verzoni, E., Gümüş, M., Stadler, W. M., Kollmannsberger, C., Melichar, B., Venugopal, B., Gross-Goupil, M., Poprach, A., Santis, M. D., Schutz, F. A., . . . Rini, B. (2024). Belzutifan versus Everolimus for Advanced Renal-Cell Carcinoma. *New England Journal of Medicine*, *391*(8), 710-721. https://doi.org/doi:10.1056/NEJMoa2313906

Chu, P. Y., Koh, A. P., Antony, J., & Huang, R. Y. (2022). Applications of the Chick Chorioallantoic Membrane as an Alternative Model for Cancer Studies. *Cells Tissues Organs*, *211*(2), 222-237. https://doi.org/10.1159/000513039

Chung, A. S., Lee, J., & Ferrara, N. (2010). Targeting the tumour vasculature: insights from physiological angiogenesis. *Nature Reviews Cancer*, *10*(7), 505-514. https://doi.org/10.1038/nrc2868

Clark, D. J., Dhanasekaran, S. M., Petralia, F., Pan, J., Song, X., Hu, Y., da Veiga Leprevost, F., Reva, B., Lih, T. M., Chang, H. Y., Ma, W., Huang, C., Ricketts, C. J., Chen, L., Krek, A., Li, Y., Rykunov, D., Li, Q. K., Chen, L. S., . . . Zhang, H. (2019). Integrated Proteogenomic Characterization of Clear Cell Renal Cell Carcinoma. *Cell*, *179*(4), 964-983.e931. https://doi.org/10.1016/j.cell.2019.10.007

Creighton, C. J., Morgan, M., Gunaratne, P. H., Wheeler, D. A., Gibbs, R. A., Gordon Robertson, A., Chu, A., Beroukhim, R., Cibulskis, K., Signoretti, S., Vandin Hsin-Ta Wu, F., Raphael, B. J., Verhaak, R. G. W., Tamboli, P., Torres-Garcia, W., Akbani, R., Weinstein, J. N., Reuter, V., Hsieh, J. J., . . . University of North Carolina at Chapel, H. (2013). Comprehensive molecular characterization of clear cell renal cell carcinoma. *Nature*, *499*(7456), 43-49. https://doi.org/10.1038/nature12222

Dalgliesh, G. L., Furge, K., Greenman, C., Chen, L., Bignell, G., Butler, A., Davies, H., Edkins, S., Hardy, C., Latimer, C., Teague, J., Andrews, J., Barthorpe, S., Beare, D., Buck, G., Campbell, P. J., Forbes, S., Jia, M., Jones, D., . . . Futreal, P. A. (2010). Systematic sequencing of renal carcinoma reveals inactivation of histone modifying genes [Research Support, Non-U.S. Gov't]. *Nature*, *463*(7279), 360-363. https://doi.org/10.1038/nature08672

De Palma, M., Biziato, D., & Petrova, T. V. (2017). Microenvironmental regulation of tumour angiogenesis. *Nature Reviews Cancer*, *17*(8), 457-474. https://doi.org/10.1038/nrc.2017.51

de Velasco, G., Miao, D., Voss, M. H., Hakimi, A. A., Hsieh, J. J., Tannir, N. M., Tamboli, P., Appleman, L. J., Rathmell, W. K., Van Allen, E. M., & Choueiri, T. K. (2016). Tumor Mutational Load and Immune Parameters across Metastatic Renal Cell Carcinoma Risk Groups. *Cancer Immunol Res*, *4*(10), 820-822. https://doi.org/10.1158/2326-6066.Cir-16-0110

de Visser, K. E., & Joyce, J. A. (2023). The evolving tumor microenvironment: From cancer initiation to metastatic outgrowth. *Cancer Cell*, *41*(3), 374-403. https://doi.org/https://doi.org/10.1016/j.ccell.2023.02.016

Dengler, V. L., Galbraith, M., & Espinosa, J. M. (2014). Transcriptional regulation by hypoxia inducible factors. *Crit Rev Biochem Mol Biol*, *49*(1), 1-15. https://doi.org/10.3109/10409238.2013.838205

Duan, C. (2016). Hypoxia-inducible factor 3 biology: complexities and emerging themes. *Am J Physiol Cell Physiol*, *310*(4), C260-269. https://doi.org/10.1152/ajpcell.00315.2015

Dudani, S., de Velasco, G., Wells, J. C., Gan, C. L., Donskov, F., Porta, C., Fraccon, A., Pasini, F., Lee, J. L., Hansen, A., Bjarnason, G. A., Beuselinck, B., Pal, S. K., Yuasa, T., Kroeger, N., Kanesvaran, R., Reaume, M. N., Canil, C., Choueiri, T. K., & Heng, D. Y. C. (2021). Evaluation of Clear Cell, Papillary, and Chromophobe Renal Cell Carcinoma Metastasis Sites and Association With Survival. *JAMA Netw Open*, *4*(1), e2021869. https://doi.org/10.1001/jamanetworkopen.2020.21869

Eckel-Passow, J. E., Serie, D. J., Cheville, J. C., Ho, T. H., Kapur, P., Brugarolas, J., Thompson, R. H., Leibovich, B. C., Kwon, E. D., Joseph, R. W., & Parker, A. S. (2017). BAP1 and PBRM1 in metastatic clear cell renal cell carcinoma: tumor heterogeneity and concordance with paired primary tumor. *BMC Urol*, *17*(1), 19. https://doi.org/10.1186/s12894-017-0209-3

Escudier, B., Porta, C., Schmidinger, M., Rioux-Leclercq, N., Bex, A., Khoo, V., Grünwald, V., Gillessen, S., & Horwich, A. (2019). Renal cell carcinoma: ESMO Clinical Practice Guidelines for diagnosis, treatment and follow-up. *Annals of Oncology*, *30*(5), 706-720. https://doi.org/10.1093/annonc/mdz056

Espana-Agusti, J., Warren, A., Chew, S. K., Adams, D. J., & Matakidou, A. (2017). Loss of PBRM1 rescues VHL dependent replication stress to promote renal carcinogenesis. *Nature Communications*, *8*(1), 2026. https://doi.org/10.1038/s41467-017-02245-1

Evans, T. R. J., Basu, B., Hubner, R., Ma, Y. T., Meyer, T., Palmer, D. H., Pinato, D. J. J., Plummer, E. R., Ross, P. J., Samson, A., Sarker, D., Kendall, T., Bellamy, C., Reeves, H. L., Thomson, F., Lawless, C. A., Stobo, J., Sansom, O. J., Mann, D. A., & Bird, T. G. (2023). A phase I/II study of the CXCR2 inhibitor, AZD5069, in combination with durvalumab, in patients (pts) with advanced hepatocellular carcinoma (HCC). *Journal of Clinical Oncology*, *41*(4_suppl), TPS631-TPS631. https://doi.org/10.1200/JCO.2023.41.4_suppl.TPS631

Farley, M. N., Schmidt, L. S., Mester, J. L., Pena-Llopis, S., Pavia-Jimenez, A., Christie, A., Vocke, C. D., Ricketts, C. J., Peterson, J., Middelton, L., Kinch, L., Grishin, N., Merino, M. J., Metwalli, A. R., Xing, C., Xie, X. J., Dahia, P. L. M., Eng, C., Linehan, W. M., & Brugarolas, J. (2013). A novel germline mutation in BAP1 predisposes to familial clear-cell renal cell carcinoma. *Mol Cancer Res*, *11*(9), 1061-1071. https://doi.org/10.1158/1541-7786.Mcr-13-0111

Fergelot, P., Bernhard, J. C., Soulet, F., Kilarski, W. W., Leon, C., Courtois, N., Deminiere, C., Herbert, J. M., Antczak, P., Falciani, F., Rioux-Leclercq, N., Patard, J. J., Ferriere, J. M., Ravaud, A., Hagedorn, M., & Bikfalvi, A. (2013). The experimental renal cell carcinoma model in the chick embryo. *Angiogenesis*, *16*(1), 181-194. https://doi.org/10.1007/s10456-012-9311-z

Fischer, D., Fluegen, G., Garcia, P., Ghaffari-Tabrizi-Wizsy, N., Gribaldo, L., Huang, R. Y., Rasche, V., Ribatti, D., Rousset, X., Pinto, M. T., Viallet, J., Wang, Y., & Schneider-Stock, R. (2022). The CAM Model-Q&A with Experts. *Cancers (Basel)*, *15*(1). https://doi.org/10.3390/cancers15010191

Folkman, J. (1971). Tumor angiogenesis: therapeutic implications. *N Engl J Med*, *285*(21), 1182-1186. https://doi.org/10.1056/nejm197111182852108

Folkman, J., Kalluri, R (2003). Beginning of angiogenesis research. In: Kufe DW, Pollock RE, Weichselbaum RR, et al., editors. Holland-Frei Cancer Medicine. 6th edition.

Hamilton (ON): BC Decker. Available from: https://www.ncbi.nlm.nih.gov/books/NBK13877/

Gao, W., Li, W., Xiao, T., Liu, X. S., & Kaelin, W. G., Jr. (2017). Inactivation of the PBRM1 tumor suppressor gene amplifies the HIF-response in VHL-/- clear cell renal carcinoma. *Proc Natl Acad Sci U S A*, *114*(5), 1027-1032. https://doi.org/10.1073/pnas.1619726114

Gerber, P. A., Hippe, A., Buhren, B. A., Müller, A., & Homey, B. (2009). Chemokines in tumor-associated angiogenesis. *Biological Chemistry*, *390*(12), 1213-1223. https://doi.org/doi:10.1515/BC.2009.144

Gerlinger, M., Horswell, S., Larkin, J., Rowan, A. J., Salm, M. P., Varela, I., Fisher, R., McGranahan, N., Matthews, N., Santos, C. R., Martinez, P., Phillimore, B., Begum, S., Rabinowitz, A., Spencer-Dene, B., Gulati, S., Bates, P. A., Stamp, G., Pickering, L., . . . Swanton, C. (2014). Genomic architecture and evolution of clear cell renal cell carcinomas defined by multiregion sequencing. *Nature Genetics*, *46*(3), 225-233. https://doi.org/10.1038/ng.2891

Ghiglione, L., Fernandez-Mañas, L., Ferrer-Mileo, L., Aversa, C., Garcia de Herreros, M., Laguna, J. C., Gorria, T., Marin, M., Jiménez, N., Prat, A., Maurel, J., Mellado, B., & Reig, O. (2022). PBRM1 genomic alterations as a predictive biomarker to immune checkpoint inhibitors (ICI) and/or anti-angiogenic therapies (anti-VEGF) in metastatic renal cell carcinoma (mRCC): A systematic review and meta-analysis. *Journal of Clinical Oncology*, *40*(16_suppl), e16515-e16515. https://doi.org/10.1200/JCO.2022.40.16_suppl.e16515

Giuliano, S., Dufies, M., Ndiaye, P. D., Viotti, J., Borchiellini, D., Parola, J., Vial, V., Cormerais, Y., Ohanna, M., Imbert, V., Chamorey, E., Rioux-Leclercq, N., Savina, A., Ferrero, J. M., Mograbi, B., & Pagès, G. (2019). Resistance to lysosomotropic drugs used to treat kidney and breast cancers involves autophagy and inflammation and converges in inducing CXCL5. *Theranostics*, *9*(4), 1181-1199. https://doi.org/10.7150/thno.29093

Gordan, J. D., Lal, P., Dondeti, V. R., Letrero, R., Parekh, K. N., Oquendo, C. E., Greenberg, R. A., Flaherty, K. T., Rathmell, W. K., Keith, B., Simon, M. C., & Nathanson, K. L. (2008). HIF-α Effects on c-Myc Distinguish Two Subtypes of Sporadic VHL-Deficient Clear Cell Renal Carcinoma. *Cancer Cell*, *14*(6), 435-446. https://doi.org/10.1016/j.ccr.2008.10.016

Gordan, J. D., Thompson, C. B., & Simon, M. C. (2007). HIF and c-Myc: Sibling Rivals for Control of Cancer Cell Metabolism and Proliferation. *Cancer Cell*, *12*(2), 108-113. https://doi.org/https://doi.org/10.1016/j.ccr.2007.07.006

Gossage, L., Eisen, T., & Maher, E. R. (2015). VHL, the story of a tumour suppressor gene. *Nature Reviews Cancer*, *15*(1), 55-64. https://doi.org/10.1038/nrc3844

Grépin, R., Guyot, M., Giuliano, S., Boncompagni, M., Ambrosetti, D., Chamorey, E., Scoazec, J. Y., Negrier, S., Simonnet, H., & Pagès, G. (2014). The CXCL7/CXCR1/2 axis is a key driver in the growth of clear cell renal cell carcinoma. *Cancer Res*, *74*(3), 873-883. https://doi.org/10.1158/0008-5472.Can-13-1267

Griffin, G. K., Newton, G., Tarrio, M. L., Bu, D.-x., Maganto-Garcia, E., Azcutia, V., Alcaide, P., Grabie, N., Luscinskas, F. W., Croce, K. J., & Lichtman, A. H. (2012). IL-17 and TNF-α Sustain Neutrophil Recruitment during Inflammation through Synergistic Effects on Endothelial Activation. *The Journal of Immunology*, *188*(12), 6287-6299. https://doi.org/10.4049/jimmunol.1200385

Gu, Y. F., Cohn, S., Christie, A., McKenzie, T., Wolff, N., Do, Q. N., Madhuranthakam, A. J., Pedrosa, I., Wang, T., Dey, A., Busslinger, M., Xie, X. J., Hammer, R. E., McKay, R. M., Kapur, P., & Brugarolas, J. (2017). Modeling Renal Cell Carcinoma in Mice: Bap1 and Pbrm1 Inactivation Drive Tumor Grade. *Cancer Discov*, *7*(8), 900-917. https://doi.org/10.1158/2159-8290.CD-17-0292

Gu, Z., Eils, R., & Schlesner, M. (2016). Complex heatmaps reveal patterns and correlations in multidimensional genomic data. *Bioinformatics*, *32*(18), 2847-2849. https://doi.org/10.1093/bioinformatics/btw313

Guo, C., Sharp, A., Gurel, B., Crespo, M., Figueiredo, I., Jain, S., Vogl, U., Rekowski, J., Rouhifard, M., Gallagher, L., Yuan, W., Carreira, S., Chandran, K., Paschalis, A., Colombo, I., Stathis, A., Bertan, C., Seed, G., Goodall, J., . . . de Bono, J. S. (2023). Targeting myeloid chemotaxis to reverse prostate cancer therapy resistance. *Nature*, *623*(7989), 1053-1061. https://doi.org/10.1038/s41586-023-06696-z

Hakimi, A. A., Attalla, K., DiNatale, R. G., Ostrovnaya, I., Flynn, J., Blum, K. A., Ged, Y., Hoen, D., Kendall, S. M., Reznik, E., Bowman, A., Hwee, J., Fong, C. J., Kuo, F., Voss, M. H., Chan, T. A., & Motzer, R. J. (2020). A pan-cancer analysis of PBAF complex mutations and their association with immunotherapy response. *Nature Communications*, *11*(1), 4168. https://doi.org/10.1038/s41467-020-17965-0

Hakimi, A. A., Voss, M. H., Kuo, F., Sanchez, A., Liu, M., Nixon, B. G., Vuong, L., Ostrovnaya, I., Chen, Y. B., Reuter, V., Riaz, N., Cheng, Y., Patel, P., Marker, M., Reising, A., Li, M. O., Chan, T. A., & Motzer, R. J. (2019). Transcriptomic Profiling of the Tumor Microenvironment Reveals Distinct Subgroups of Clear Cell Renal Cell Cancer: Data from a Randomized Phase III Trial. *Cancer Discov*, *9*(4), 510-525. https://doi.org/10.1158/2159-8290.CD-18-0957

Hanahan, D., & Weinberg, R. A. (2000). The Hallmarks of Cancer. *Cell*, *100*(1), 57-70. https://doi.org/10.1016/S0092-8674(00)81683-9

Hanahan, D., & Weinberg, R. A. (2011). Hallmarks of cancer: the next generation. *Cell*, *144*(5), 646-674. https://doi.org/10.1016/j.cell.2011.02.013

Heiss, M., Hellström, M., Kalén, M., May, T., Weber, H., Hecker, M., Augustin, H. G., & Korff, T. (2015). Endothelial cell spheroids as a versatile tool to study angiogenesis in vitro. *The FASEB Journal*, *29*(7), 3076-3084. https://doi.org/https://doi.org/10.1096/fj.14-267633

Heng, D. Y., Xie, W., Regan, M. M., Warren, M. A., Golshayan, A. R., Sahi, C., Eigl, B. J., Ruether, J. D., Cheng, T., North, S., Venner, P., Knox, J. J., Chi, K. N., Kollmannsberger, C., McDermott, D. F., Oh, W. K., Atkins, M. B., Bukowski, R. M., Rini, B. I., & Choueiri, T. K. (2009). Prognostic factors for overall survival in patients with metastatic renal cell carcinoma treated with vascular endothelial growth factor-targeted agents: results from a large, multicenter study. *J Clin Oncol*, *27*(34), 5794-5799. https://doi.org/10.1200/jco.2008.21.4809

Highfill, S. L., Cui, Y., Giles, A. J., Smith, J. P., Zhang, H., Morse, E., Kaplan, R. N., & Mackall, C. L. (2014). Disruption of CXCR2-mediated MDSC tumor trafficking enhances anti-PD1 efficacy. *Sci Transl Med*, *6*(237), 237ra267. https://doi.org/10.1126/scitranslmed.3007974

Hillen, F., & Griffioen, A. W. (2007). Tumour vascularization: sprouting angiogenesis and beyond. *Cancer Metastasis Rev*, *26*(3-4), 489-502. https://doi.org/10.1007/s10555-007-9094-7

Hodis, E., Watson, I. R., Kryukov, G. V., Arold, S. T., Imielinski, M., Theurillat, J. P., Nickerson, E., Auclair, D., Li, L., Place, C., Dicara, D., Ramos, A. H., Lawrence, M.

S., Cibulskis, K., Sivachenko, A., Voet, D., Saksena, G., Stransky, N., Onofrio, R. C., . . . Chin, L. (2012). A landscape of driver mutations in melanoma. *Cell*, *150*(2), 251-263. https://doi.org/10.1016/j.cell.2012.06.024

Hoefflin, R., Harlander, S., Schäfer, S., Metzger, P., Kuo, F., Schönenberger, D., Adlesic, M., Peighambari, A., Seidel, P., Chen, C. Y., Consenza-Contreras, M., Jud, A., Lahrmann, B., Grabe, N., Heide, D., Uhl, F. M., Chan, T. A., Duyster, J., Zeiser, R., . . . Frew, I. J. (2020). HIF-1α and HIF-2α differently regulate tumour development and inflammation of clear cell renal cell carcinoma in mice. *Nat Commun*, *11*(1), 4111. https://doi.org/10.1038/s41467-020-17873-3

Holmes, D. I., & Zachary, I. (2005). The vascular endothelial growth factor (VEGF) family: angiogenic factors in health and disease. *Genome Biol*, *6*(2), 209. https://doi.org/10.1186/gb-2005-6-2-209

Hsieh, J. J., Chen, D., Wang, P. I., Marker, M., Redzematovic, A., Chen, Y. B., Selcuklu, S. D., Weinhold, N., Bouvier, N., Huberman, K. H., Bhanot, U., Chevinsky, M. S., Patel, P., Pinciroli, P., Won, H. H., You, D., Viale, A., Lee, W., Hakimi, A. A., . . . Motzer, R. J. (2017). Genomic Biomarkers of a Randomized Trial Comparing First-line Everolimus and Sunitinib in Patients with Metastatic Renal Cell Carcinoma. *Eur Urol*, *71*(3), 405-414. https://doi.org/10.1016/j.eururo.2016.10.007

Hsieh, J. J., Purdue, M. P., Signoretti, S., Swanton, C., Albiges, L., Schmidinger, M., Heng, D. Y., Larkin, J., & Ficarra, V. (2017). Renal cell carcinoma. *Nature Reviews Disease Primers*, *3*(1), 17009. https://doi.org/10.1038/nrdp.2017.9

Huang, K., Sun, R., Chen, J., Yang, Q., Wang, Y., Zhang, Y., Xie, K., Zhang, T., Li, R., Zhao, Q., Zou, L., & Li, J. (2020). A novel EZH2 inhibitor induces synthetic lethality and apoptosis in PBRM1-deficient cancer cells. *Cell Cycle*, *19*(7), 758-771. https://doi.org/10.1080/15384101.2020.1729450

Hughes, C. E., & Nibbs, R. J. B. (2018). A guide to chemokines and their receptors. *Febs j*, *285*(16), 2944-2971. https://doi.org/10.1111/febs.14466

Hurwitz, H., Fehrenbacher, L., Novotny, W., Cartwright, T., Hainsworth, J., Heim, W., Berlin, J., Baron, A., Griffing, S., Holmgren, E., Ferrara, N., Fyfe, G., Rogers, B., Ross, R., & Kabbinavar, F. (2004). Bevacizumab plus Irinotecan, Fluorouracil, and Leucovorin for Metastatic Colorectal Cancer. *New England Journal of Medicine*, *350*(23), 2335-2342. https://doi.org/doi:10.1056/NEJMoa032691

Ibragimova, I., Maradeo, M. E., Dulaimi, E., & Cairns, P. (2013). Aberrant promoter hypermethylation of PBRM1, BAP1, SETD2, KDM6A and other chromatin-modifying genes is absent or rare in clear cell RCC. *Epigenetics*, *8*(5), 486-493. https://doi.org/10.4161/epi.24552

Jain, R. K. (2001). Normalizing tumor vasculature with anti-angiogenic therapy: A new paradigm for combination therapy. *Nature Medicine*, *7*(9), 987-989. https://doi.org/10.1038/nm0901-987

Jamieson, T., Clarke, M., Steele, C. W., Samuel, M. S., Neumann, J., Jung, A., Huels, D., Olson, M. F., Das, S., Nibbs, R. J., & Sansom, O. J. (2012). Inhibition of CXCR2 profoundly suppresses inflammation-driven and spontaneous tumorigenesis. *J Clin Invest*, *122*(9), 3127-3144. https://doi.org/10.1172/jci61067

Jin, L., Tao, H., Karachi, A., Long, Y., Hou, A. Y., Na, M., Dyson, K. A., Grippin, A. J., Deleyrolle, L. P., Zhang, W., Rajon, D. A., Wang, Q. J., Yang, J. C., Kresak, J. L., Sayour, E. J., Rahman, M., Bova, F. J., Lin, Z., Mitchell, D. A., & Huang, J. (2019). CXCR1- or CXCR2-modified CAR T cells co-opt IL-8 for maximal antitumor efficacy

in solid tumors. *Nature Communications*, *10*(1), 4016. https://doi.org/10.1038/s41467-019-11869-4

Kabaria, R., Klaassen, Z., & Terris, M. K. (2016). Renal cell carcinoma: links and risks. *Int J Nephrol Renovasc Dis*, *9*, 45-52. https://doi.org/10.2147/ijnrd.S75916

Kakarougkas, A., Ismail, A., Chambers, A. L., Riballo, E., Herbert, A. D., Künzel, J., Löbrich, M., Jeggo, P. A., & Downs, J. A. (2014). Requirement for PBAF in transcriptional repression and repair at DNA breaks in actively transcribed regions of chromatin. *Mol Cell*, *55*(5), 723-732. https://doi.org/10.1016/j.molcel.2014.06.028

Kalra, S., Atkinson, B. J., Matrana, M. R., Matin, S. F., Wood, C. G., Karam, J. A., Tamboli, P., Sircar, K., Rao, P., Corn, P. G., Tannir, N. M., & Jonasch, E. (2016). Prognosis of patients with metastatic renal cell carcinoma and pancreatic metastases. *BJU Int*, *117*(5), 761-765. https://doi.org/10.1111/bju.13185

Kapitsinou, P. P., & Haase, V. H. (2008). The VHL tumor suppressor and HIF: insights from genetic studies in mice. *Cell Death & Differentiation*, *15*(4), 650-659. https://doi.org/10.1038/sj.cdd.4402313

Kassambara, A. (2023). ggpubr: 'ggplot2' Based Publication Ready Plots. R package version 0.6.0. In https://rpkgs.datanovia.com/ggpubr/.

Kassambara, A., Kosinski, M., & Biecek, P. (2021). survminer: Drawing Survival Curves using 'ggplot2'*. R package version 0.4.9.* In https://rpkgs.datanovia.com/survminer/index.html

Keane, M. P., Belperio, J. A., Xue, Y. Y., Burdick, M. D., & Strieter, R. M. (2004). Depletion of CXCR2 Inhibits Tumor Growth and Angiogenesis in a Murine Model of Lung Cancer1. *The Journal of Immunology*, *172*(5), 2853-2860. https://doi.org/10.4049/jimmunol.172.5.2853

Keeley, E. C., Mehrad, B., & Strieter, R. M. (2010). CXC chemokines in cancer angiogenesis and metastases. *Adv Cancer Res*, *106*, 91-111. https://doi.org/10.1016/s0065-230x(10)06003-3

Keith, B., Johnson, R. S., & Simon, M. C. (2012). HIF1α and HIF2α: sibling rivalry in hypoxic tumour growth and progression. *Nature Reviews Cancer*, *12*(1), 9-22. https://doi.org/10.1038/nrc3183

Kim, H. S., Skurk, C., Thomas, S. R., Bialik, A., Suhara, T., Kureishi, Y., Birnbaum, M., Keaney, J. F., Jr., & Walsh, K. (2002). Regulation of angiogenesis by glycogen synthase kinase-3beta. *J Biol Chem*, *277*(44), 41888-41896. https://doi.org/10.1074/jbc.M206657200

Kim, K. H., Kim, W., Howard, T. P., Vazquez, F., Tsherniak, A., Wu, J. N., Wang, W., Haswell, J. R., Walensky, L. D., Hahn, W. C., Orkin, S. H., & Roberts, C. W. M. (2015). SWI/SNF-mutant cancers depend on catalytic and non-catalytic activity of EZH2. *Nature Medicine*, *21*(12), 1491-1496. https://doi.org/10.1038/nm.3968

Kim, K. J., Li, B., Winer, J., Armanini, M., Gillett, N., Phillips, H. S., & Ferrara, N. (1993). Inhibition of vascular endothelial growth factor-induced angiogenesis suppresses tumour growth in vivo. *Nature*, *362*(6423), 841-844. https://doi.org/10.1038/362841a0

Ko, J. J., Xie, W., Kroeger, N., Lee, J. L., Rini, B. I., Knox, J. J., Bjarnason, G. A., Srinivas, S., Pal, S. K., Yuasa, T., Smoragiewicz, M., Donskov, F., Kanesvaran, R., Wood, L., Ernst, D. S., Agarwal, N., Vaishampayan, U. N., Rha, S. Y., Choueiri, T. K., & Heng, D. Y. (2015). The International Metastatic Renal Cell Carcinoma Database Consortium model as a prognostic tool in patients with metastatic renal cell

carcinoma previously treated with first-line targeted therapy: a population-based study. *Lancet Oncol*, *16*(3), 293-300. https://doi.org/10.1016/s1470-2045(14)71222-7

Korbecki, J., Kojder, K., Kapczuk, P., Kupnicka, P., Gawrońska-Szklarz, B., Gutowska, I., Chlubek, D., & Baranowska-Bosiacka, I. (2021). The Effect of Hypoxia on the Expression of CXC Chemokines and CXC Chemokine Receptors-A Review of Literature. *Int J Mol Sci*, *22*(2). https://doi.org/10.3390/ijms22020843

Korff, T., & Augustin, H. G. (1998). Integration of endothelial cells in multicellular spheroids prevents apoptosis and induces differentiation. *J Cell Biol*, *143*(5), 1341-1352. https://doi.org/10.1083/jcb.143.5.1341

Kremer, V., Ligtenberg, M. A., Zendehdel, R., Seitz, C., Duivenvoorden, A., Wennerberg, E., Colon, E., Scherman-Plogell, A. H., & Lundqvist, A. (2017). Genetic engineering of human NK cells to express CXCR2 improves migration to renal cell carcinoma. *J Immunother Cancer*, *5*(1), 73. https://doi.org/10.1186/s40425-017-0275-9

Kulbe, H., Thompson, R., Wilson, J. L., Robinson, S., Hagemann, T., Fatah, R., Gould, D., Ayhan, A., & Balkwill, F. (2007). The inflammatory cytokine tumor necrosis factor-alpha generates an autocrine tumor-promoting network in epithelial ovarian cancer cells. *Cancer Res*, *67*(2), 585-592. https://doi.org/10.1158/0008-5472.Can-06-2941

Kunz, P., Schenker, A., Sahr, H., Lehner, B., & Fellenberg, J. (2019). Optimization of the chicken chorioallantoic membrane assay as reliable in vivo model for the analysis of osteosarcoma. *PLoS One*, *14*(4), e0215312. https://doi.org/10.1371/journal.pone.0215312

Kuo, H.-Y., Khan, K. A., & Kerbel, R. S. (2024). Antiangiogenic–immune-checkpoint inhibitor combinations: lessons from phase III clinical trials. *Nature Reviews Clinical Oncology*, *21*(6), 468-482. https://doi.org/10.1038/s41571-024-00886-y

Lazennec, G., Rajarathnam, K., & Richmond, A. (2024). CXCR2 chemokine receptor – a master regulator in cancer and physiology. *Trends in Molecular Medicine*, *30*(1), 37-55. https://doi.org/https://doi.org/10.1016/j.molmed.2023.09.003

Lee, M. H., Laajala, E., Kreutzman, A., Järvinen, P., Nísen, H., Mirtti, T., Hollmén, M., & Mustjoki, S. (2022). The tumor and plasma cytokine profiles of renal cell carcinoma patients. *Scientific Reports*, *12*(1), 13416. https://doi.org/10.1038/s41598-022-17592-3

Leslie, J., Mackey, J. B. G., Jamieson, T., Ramon-Gil, E., Drake, T. M., Fercoq, F., Clark, W., Gilroy, K., Hedley, A., Nixon, C., Luli, S., Laszczewska, M., Pinyol, R., Esteban-Fabró, R., Willoughby, C. E., Haber, P. K., Andreu-Oller, C., Rahbari, M., Fan, C., . . . Mann, D. A. (2022). CXCR2 inhibition enables NASH-HCC immunotherapy. *Gut*, *71*(10), 2093-2106. https://doi.org/10.1136/gutjnl-2021-326259

Li, N., Liu, Q., Han, Y., Pei, S., Cheng, B., Xu, J., Miao, X., Pan, Q., Wang, H., Guo, J., Wang, X., Zhang, G., Lian, Y., Zhang, W., Zang, Y., Tan, M., Li, Q., Wang, X., Xiao, Y., . . . Qin, J. (2022). ARID1A loss induces polymorphonuclear myeloid-derived suppressor cell chemotaxis and promotes prostate cancer progression. *Nature Communications*, *13*(1), 7281. https://doi.org/10.1038/s41467-022-34871-9

Li, X., Chen, Y., Chang, Y., Li, S., Zhao, Z., & Zhang, H. (2016). CXCR2 is involved in pulmonary intravascular macrophage accumulation and angiogenesis in a rat model of hepatopulmonary syndrome. *Clinical Science*, *131*(2), 159-168. https://doi.org/10.1042/cs20160593

Liao, Y., Smyth, G. K., & Shi, W. (2013). The Subread aligner: fast, accurate and scalable read mapping by seed-and-vote. *Nucleic Acids Res*, *41*(10), e108. https://doi.org/10.1093/nar/gkt214

Liao, Y., Smyth, G. K., & Shi, W. (2014). featureCounts: an efficient general purpose program for assigning sequence reads to genomic features. *Bioinformatics*, *30*(7), 923-930. https://doi.org/10.1093/bioinformatics/btt656

Linehan, W. M., & Ricketts, C. J. (2019). The Cancer Genome Atlas of renal cell carcinoma: findings and clinical implications. *Nature Reviews Urology*, *16*(9), 539-552. https://doi.org/10.1038/s41585-019-0211-5

Liu, T., Xia, Q., Zhang, H., Wang, Z., Yang, W., Gu, X., Hou, T., Chen, Y., Pei, X., Zhu, G., He, D., Li, L., & Xu, S. (2020). CCL5-dependent mast cell infiltration into the tumor microenvironment in clear cell renal cell carcinoma patients. *Aging (Albany NY)*, *12*(21), 21809-21836. https://doi.org/10.18632/aging.103999

Liu, X.-D., Kong, W., Peterson, C. B., McGrail, D. J., Hoang, A., Zhang, X., Lam, T., Pilie, P. G., Zhu, H., Beckermann, K. E., Haake, S. M., Isgandrova, S., Martinez-Moczygemba, M., Sahni, N., Tannir, N. M., Lin, S.-Y., Rathmell, W. K., & Jonasch, E. (2020). PBRM1 loss defines a nonimmunogenic tumor phenotype associated with checkpoint inhibitor resistance in renal carcinoma. *Nature Communications*, *11*(1), 2135. https://doi.org/10.1038/s41467-020-15959-6

Liu, Y., Mei, J., Gonzales, L., Yang, G., Dai, N., Wang, P., Zhang, P., Favara, M., Malcolm, K. C., Guttentag, S., & Worthen, G. S. (2011). IL-17A and TNF-α Exert Synergistic Effects on Expression of CXCL5 by Alveolar Type II Cells In Vivo and In Vitro. *The Journal of Immunology*, *186*(5), 3197-3205. https://doi.org/10.4049/jimmunol.1002016

Liu, Z.-L., Chen, H.-H., Zheng, L.-L., Sun, L.-P., & Shi, L. (2023). Angiogenic signaling pathways and anti-angiogenic therapy for cancer. *Signal Transduction and Targeted Therapy*, *8*(1), 198. https://doi.org/10.1038/s41392-023-01460-1

Love, M. I., Huber, W., & Anders, S. (2014). Moderated estimation of fold change and dispersion for RNA-seq data with DESeq2. *Genome Biol*, *15*(12), 550. https://doi.org/10.1186/s13059-014-0550-8

Marshall, K. M., Kanczler, J. M., & Oreffo, R. O. (2020). Evolving applications of the egg: chorioallantoic membrane assay and ex vivo organotypic culture of materials for bone tissue engineering. *J Tissue Eng*, *11*, 2041731420942734. https://doi.org/10.1177/2041731420942734

Martin, J. D., Seano, G., & Jain, R. K. (2019). Normalizing Function of Tumor Vessels: Progress, Opportunities, and Challenges. *Annu Rev Physiol*, *81*, 505-534. https://doi.org/10.1146/annurev-physiol-020518-114700

Martin, J. D., Seano, G., & Jain, R. K. (2019). Normalizing Function of Tumor Vessels: Progress, Opportunities, and Challenges. *Annual Review of Physiology*, *81*(Volume 81, 2019), 505-534. https://doi.org/https://doi.org/10.1146/annurev-physiol-020518-114700

Martin, L. J., Koegl, M., Bader, G., Cockcroft, X. L., Fedorov, O., Fiegen, D., Gerstberger, T., Hofmann, M. H., Hohmann, A. F., Kessler, D., Knapp, S., Knesl, P., Kornigg, S., Müller, S., Nar, H., Rogers, C., Rumpel, K., Schaaf, O., Steurer, S., . . . McConnell, D. (2016). Structure-Based Design of an in Vivo Active Selective BRD9 Inhibitor. *J Med Chem*, *59*(10), 4462-4475. https://doi.org/10.1021/acs.jmedchem.5b01865

Mashtalir, N., D'Avino, A. R., Michel, B. C., Luo, J., Pan, J., Otto, J. E., Zullow, H. J., McKenzie, Z. M., Kubiak, R. L., St Pierre, R., Valencia, A. M., Poynter, S. J., Cassel,

S. H., Ranish, J. A., & Kadoch, C. (2018). Modular Organization and Assembly of SWI/SNF Family Chromatin Remodeling Complexes. *Cell*, *175*(5), 1272-1288.e1220. https://doi.org/10.1016/j.cell.2018.09.032

McCubrey, J. A., Fitzgerald, T. L., Yang, L. V., Lertpiriyapong, K., Steelman, L. S., Abrams, S. L., Montalto, G., Cervello, M., Neri, L. M., Cocco, L., Martelli, A. M., Laidler, P., Dulińska-Litewka, J., Rakus, D., Gizak, A., Nicoletti, F., Falzone, L., Candido, S., & Libra, M. (2017). Roles of GSK-3 and microRNAs on epithelial mesenchymal transition and cancer stem cells. *Oncotarget*, *8*(8), 14221-14250. https://doi.org/10.18632/oncotarget.13991

McDermott, D. F., Huseni, M. A., Atkins, M. B., Motzer, R. J., Rini, B. I., Escudier, B., Fong, L., Joseph, R. W., Pal, S. K., Reeves, J. A., Sznol, M., Hainsworth, J., Rathmell, W. K., Stadler, W. M., Hutson, T., Gore, M. E., Ravaud, A., Bracarda, S., Suárez, C., . . . Powles, T. (2018). Clinical activity and molecular correlates of response to atezolizumab alone or in combination with bevacizumab versus sunitinib in renal cell carcinoma. *Nature Medicine*, *24*(6), 749-757. https://doi.org/10.1038/s41591-018-0053-3

McGrail, D. J., Pilié, P. G., Rashid, N. U., Voorwerk, L., Slagter, M., Kok, M., Jonasch, E., Khasraw, M., Heimberger, A. B., Lim, B., Ueno, N. T., Litton, J. K., Ferrarotto, R., Chang, J. T., Moulder, S. L., & Lin, S. Y. (2021). High tumor mutation burden fails to predict immune checkpoint blockade response across all cancer types. *Ann Oncol*, *32*(5), 661-672. https://doi.org/10.1016/j.annonc.2021.02.006

Mehrad, B., Keane, M. P., & Strieter, R. M. (2007). Chemokines as mediators of angiogenesis. *Thromb Haemost*, *97*(5), 755-762.

Mestas, J., Burdick, M. D., Reckamp, K., Pantuck, A., Figlin, R. A., & Strieter, R. M. (2005). The Role of CXCR2/CXCR2 Ligand Biological Axis in Renal Cell Carcinoma1. *The Journal of Immunology*, *175*(8), 5351-5357. https://doi.org/10.4049/jimmunol.175.8.5351

Miao, D., Margolis, C. A., Gao, W., Voss, M. H., Li, W., Martini, D. J., Norton, C., Bosse, D., Wankowicz, S. M., Cullen, D., Horak, C., Wind-Rotolo, M., Tracy, A., Giannakis, M., Hodi, F. S., Drake, C. G., Ball, M. W., Allaf, M. E., Snyder, A., . . . Van Allen, E. M. (2018). Genomic correlates of response to immune checkpoint therapies in clear cell renal cell carcinoma. *Science*, *359*(6377), 801-806. https://doi.org/10.1126/science.aan5951

Michel, B. C., D'Avino, A. R., Cassel, S. H., Mashtalir, N., McKenzie, Z. M., McBride, M. J., Valencia, A. M., Zhou, Q., Bocker, M., Soares, L. M. M., Pan, J., Remillard, D. I., Lareau, C. A., Zullow, H. J., Fortoul, N., Gray, N. S., Bradner, J. E., Chan, H. M., & Kadoch, C. (2018). A non-canonical SWI/SNF complex is a synthetic lethal target in cancers driven by BAF complex perturbation. *Nature Cell Biology*, *20*(12), 1410-1420. https://doi.org/10.1038/s41556-018-0221-1

Miebach, L., Berner, J., & Bekeschus, S. (2022). In ovo model in cancer research and tumor immunology. *Front Immunol*, *13*, 1006064. https://doi.org/10.3389/fimmu.2022.1006064

Mills, K. H. G. (2023). IL-17 and IL-17-producing cells in protection versus pathology. *Nature Reviews Immunology*, *23*(1), 38-54. https://doi.org/10.1038/s41577-022-00746-9

Mitchell, T. J., Turajlic, S., Rowan, A., Nicol, D., Farmery, J. H. R., O'Brien, T., Martincorena, I., Tarpey, P., Angelopoulos, N., Yates, L. R., Butler, A. P., Raine, K., Stewart, G. D., Challacombe, B., Fernando, A., Lopez, J. I., Hazell, S., Chandra,

A., Chowdhury, S., . . . Campbell, P. J. (2018). Timing the Landmark Events in the Evolution of Clear Cell Renal Cell Cancer: TRACERx Renal. *Cell*, *173*(3), 611-623.e617. https://doi.org/10.1016/j.cell.2018.02.020

Mittal, P., & Roberts, C. W. M. (2020). The SWI/SNF complex in cancer — biology, biomarkers and therapy. *Nature Reviews Clinical Oncology*, *17*(7), 435-448. https://doi.org/10.1038/s41571-020-0357-3

Montemagno, C., Jacquel, A., Pandiani, C., Rastoin, O., Dawaliby, R., Schmitt, T., Bourgoin, M., Palenzuela, H., Rossi, A.-L., Ambrosetti, D., Durivault, J., Luciano, F., Borchiellini, D., Le Du, J., Gonçalves, L. C. P., Auberger, P., Benhida, R., Kinget, L., Beuselinck, B., . . . Dufies, M. (2024). Unveiling CXCR2 as a promising therapeutic target in renal cell carcinoma: exploring the immunotherapeutic paradigm shift through its inhibition by RCT001. *Journal of Experimental & Clinical Cancer Research*, *43*(1), 86. https://doi.org/10.1186/s13046-024-02984-2

Monzon, F. A., Alvarez, K., Peterson, L., Truong, L., Amato, R. J., Hernandez-McClain, J., Tannir, N., Parwani, A. V., & Jonasch, E. (2011). Chromosome 14q loss defines a molecular subtype of clear-cell renal cell carcinoma associated with poor prognosis. *Modern pathology : an official journal of the United States and Canadian Academy of Pathology, Inc*, *24*(11), 1470–1479. https://doi.org/10.1038/modpathol.2011.107

Morikawa, S., Baluk, P., Kaidoh, T., Haskell, A., Jain, R. K., & McDonald, D. M. (2002). Abnormalities in Pericytes on Blood Vessels and Endothelial Sprouts in Tumors. *The American Journal of Pathology*, *160*(3), 985-1000. https://doi.org/https://doi.org/10.1016/S0002-9440(10)64920-6

Motzer, R. J., Banchereau, R., Hamidi, H., Powles, T., McDermott, D., Atkins, M. B., Escudier, B., Liu, L.-F., Leng, N., Abbas, A. R., Fan, J., Koeppen, H., Lin, J., Carroll, S., Hashimoto, K., Mariathasan, S., Green, M., Tayama, D., Hegde, P. S., . . . Rini, B. (2020). Molecular Subsets in Renal Cancer Determine Outcome to Checkpoint and Angiogenesis Blockade. *Cancer Cell*, *38*(6), 803-817.e804. https://doi.org/10.1016/j.ccell.2020.10.011

Motzer, R. J., Choueiri, T. K., McDermott, D. F., Powles, T., Vano, Y. A., Gupta, S., Yao, J., Han, C., Ammar, R., Papillon-Cavanagh, S., Saggi, S. S., McHenry, M. B., Ross-Macdonald, P., & Wind-Rotolo, M. (2022). Biomarker analysis from CheckMate 214: nivolumab plus ipilimumab versus sunitinib in renal cell carcinoma. *J Immunother Cancer*, *10*(3). https://doi.org/10.1136/jitc-2021-004316

Motzer, R. J., Robbins, P. B., Powles, T., Albiges, L., Haanen, J. B., Larkin, J., Mu, X. J., Ching, K. A., Uemura, M., Pal, S. K., Alekseev, B., Gravis, G., Campbell, M. T., Penkov, K., Lee, J. L., Hariharan, S., Wang, X., Zhang, W., Wang, J., . . . Choueiri, T. K. (2020). Avelumab plus axitinib versus sunitinib in advanced renal cell carcinoma: biomarker analysis of the phase 3 JAVELIN Renal 101 trial. *Nature Medicine*, *26*(11), 1733-1741. https://doi.org/10.1038/s41591-020-1044-8

Mukaida, N., Sasaki, S., & Baba, T. (2014). Chemokines in cancer development and progression and their potential as targeting molecules for cancer treatment. *Mediators Inflamm*, *2014*, 170381. https://doi.org/10.1155/2014/170381

Muz, B., de la Puente, P., Azab, F., & Azab, A. K. (2015). The role of hypoxia in cancer progression, angiogenesis, metastasis, and resistance to therapy. *Hypoxia (Auckl)*, *3*, 83-92. https://doi.org/10.2147/hp.S93413

Najjar, Y. G., Rayman, P., Jia, X., Pavicic, P. G., Jr, Rini, B. I., Tannenbaum, C., Ko, J., Haywood, S., Cohen, P., Hamilton, T., Diaz-Montero, C. M., & Finke, J. (2017).

Myeloid-Derived Suppressor Cell Subset Accumulation in Renal Cell Carcinoma Parenchyma Is Associated with Intratumoral Expression of IL1β, IL8, CXCL5, and Mip-1α. *Clinical Cancer Research*, *23*(9), 2346-2355. https://doi.org/10.1158/1078-0432.Ccr-15-1823

Nargund, A. M., Pham, C. G., Dong, Y., Wang, P. I., Osmangeyoglu, H. U., Xie, Y., Aras, O., Han, S., Oyama, T., Takeda, S., Ray, C. E., Dong, Z., Berge, M., Hakimi, A. A., Monette, S., Lekaye, C. L., Koutcher, J. A., Leslie, C. S., Creighton, C. J., . . . Hsieh, J. J. (2017). The SWI/SNF Protein PBRM1 Restrains VHL-Loss-Driven Clear Cell Renal Cell Carcinoma. *Cell Rep*, *18*(12), 2893-2906. https://doi.org/10.1016/j.celrep.2017.02.074

Nickerson, M. L., Jaeger, E., Shi, Y., Durocher, J. A., Mahurkar, S., Zaridze, D., Matveev, V., Janout, V., Kollarova, H., Bencko, V., Navratilova, M., Szeszenia-Dabrowska, N., Mates, D., Mukeria, A., Holcatova, I., Schmidt, L. S., Toro, J. R., Karami, S., Hung, R., . . . Moore, L. E. (2008). Improved identification of von Hippel-Lindau gene alterations in clear cell renal tumors. *Clin Cancer Res*, *14*(15), 4726-4734. https://doi.org/10.1158/1078-0432.Ccr-07-4921

Pan, D., Kobayashi, A., Jiang, P., Ferrari de Andrade, L., Tay, R. E., Luoma, A. M., Tsoucas, D., Qiu, X., Lim, K., Rao, P., Long, H. W., Yuan, G.-C., Doench, J., Brown, M., Liu, X. S., & Wucherpfennig, K. W. (2018). A major chromatin regulator determines resistance of tumor cells to T cell–mediated killing. *Science*, *359*(6377), 770-775. https://doi.org/doi:10.1126/science.aao1710

Pérez-Gutiérrez, L., & Ferrara, N. (2023). Biology and therapeutic targeting of vascular endothelial growth factor A. *Nature Reviews Molecular Cell Biology*, *24*(11), 816-834. https://doi.org/10.1038/s41580-023-00631-w

Qiu, W. Z., Zhang, H. B., Xia, W. X., Ke, L. R., Yang, J., Yu, Y. H., Liang, H., Huang, X. J., Liu, G. Y., Li, W. Z., Xiang, Y. Q., Kang, T. B., Guo, X., & Lv, X. (2018). The CXCL5/CXCR2 axis contributes to the epithelial-mesenchymal transition of nasopharyngeal carcinoma cells by activating ERK/GSK-3β/snail signalling. *J Exp Clin Cancer Res*, *37*(1), 85. https://doi.org/10.1186/s13046-018-0722-6

Raval, R. R., Lau, K. W., Tran, M. G., Sowter, H. M., Mandriota, S. J., Li, J. L., Pugh, C. W., Maxwell, P. H., Harris, A. L., & Ratcliffe, P. J. (2005). Contrasting properties of hypoxia-inducible factor 1 (HIF-1) and HIF-2 in von Hippel-Lindau-associated renal cell carcinoma. *Molecular and cellular biology*, *25*(13), 5675–5686. https://doi.org/10.1128/MCB.25.13.5675-5686.2005

Remillard, D., Buckley, D. L., Paulk, J., Brien, G. L., Sonnett, M., Seo, H. S., Dastjerdi, S., Wühr, M., Dhe-Paganon, S., Armstrong, S. A., & Bradner, J. E. (2017). Degradation of the BAF Complex Factor BRD9 by Heterobifunctional Ligands. *Angew Chem Int Ed Engl*, *56*(21), 5738-5743. https://doi.org/10.1002/anie.201611281

Ritchie, M. E., Phipson, B., Wu, D., Hu, Y., Law, C. W., Shi, W., & Smyth, G. K. (2015). limma powers differential expression analyses for RNA-sequencing and microarray studies. *Nucleic Acids Research*, *43*(7), e47-e47. https://doi.org/10.1093/nar/gkv007

Robinson, M. D., McCarthy, D. J., & Smyth, G. K. (2010). edgeR: a Bioconductor package for differential expression analysis of digital gene expression data. *Bioinformatics*, *26*(1), 139-140. https://doi.org/10.1093/bioinformatics/btp616

Rooney, M. S., Shukla, S. A., Wu, C. J., Getz, G., & Hacohen, N. (2015). Molecular and genetic properties of tumors associated with local immune cytolytic activity. *Cell*, *160*(1-2), 48-61. https://doi.org/10.1016/j.cell.2014.12.033

Sadek, M., Sheth, A., Zimmerman, G., Hays, E., & Vélez-Cruz, R. (2022). The role of SWI/SNF chromatin remodelers in the repair of DNA double strand breaks and cancer therapy. *Front Cell Dev Biol*, *10*, 1071786. https://doi.org/10.3389/fcell.2022.1071786

Saliby, R. M., Labaki, C., Jammihal, T. R., Xie, W., Sun, M., Shah, V., Saad, E., Kane, M. H., Kashima, S., Sadak, K., El Zarif, T., Poduval, D., Motzer, R. J., Powles, T., Rini, B. I., Albiges, L., Pal, S. K., McGregor, B. A., McKay, R. R., . . . Braun, D. A. (2024). Impact of renal cell carcinoma molecular subtypes on immunotherapy and targeted therapy outcomes. *Cancer Cell*, *42*(5), 732-735. https://doi.org/10.1016/j.ccell.2024.03.002

Sarogni, P., Mapanao, A. K., Marchetti, S., Kusmic, C., & Voliani, V. (2021). A Standard Protocol for the Production and Bioevaluation of Ethical In Vivo Models of HPV-Negative Head and Neck Squamous Cell Carcinoma. *ACS Pharmacology & Translational Science*, *4*(3), 1227-1234. https://doi.org/10.1021/acsptsci.1c00083

Sato, Y., Yoshizato, T., Shiraishi, Y., Maekawa, S., Okuno, Y., Kamura, T., Shimamura, T., Sato-Otsubo, A., Nagae, G., Suzuki, H., Nagata, Y., Yoshida, K., Kon, A., Suzuki, Y., Chiba, K., Tanaka, H., Niida, A., Fujimoto, A., Tsunoda, T., . . . Ogawa, S. (2013). Integrated molecular analysis of clear-cell renal cell carcinoma. *Nature Genetics*, *45*(8), 860-867. https://doi.org/10.1038/ng.2699

Schneider-Stock, R., & Ribatti, D. (2021). The CAM Assay as an Alternative In Vivo Model for Drug Testing. *Handb Exp Pharmacol*, *265*, 303-323. https://doi.org/10.1007/164_2020_375

Şenbabaoğlu, Y., Gejman, R. S., Winer, A. G., Liu, M., Van Allen, E. M., de Velasco, G., Miao, D., Ostrovnaya, I., Drill, E., Luna, A., Weinhold, N., Lee, W., Manley, B. J., Khalil, D. N., Kaffenberger, S. D., Chen, Y., Danilova, L., Voss, M. H., Coleman, J. A., . . . Hakimi, A. A. (2016). Tumor immune microenvironment characterization in clear cell renal cell carcinoma identifies prognostic and immunotherapeutically relevant messenger RNA signatures. *Genome Biol*, *17*(1), 231. https://doi.org/10.1186/s13059-016-1092-z

Shain, A. H., & Pollack, J. R. (2013). The spectrum of SWI/SNF mutations, ubiquitous in human cancers. *PLoS One*, *8*(1), e55119. https://doi.org/10.1371/journal.pone.0055119

Sharma, B., Nawandar, D. M., Nannuru, K. C., Varney, M. L., & Singh, R. K. (2013). Targeting CXCR2 Enhances Chemotherapeutic Response, Inhibits Mammary Tumor Growth, Angiogenesis, and Lung Metastasis. *Molecular Cancer Therapeutics*, *12*(5), 799-808. https://doi.org/10.1158/1535-7163.Mct-12-0529

Shen, C., Beroukhim, R., Schumacher, S. E., Zhou, J., Chang, M., Signoretti, S., & Kaelin, W. G., Jr. (2011). Genetic and functional studies implicate HIF1α as a 14q kidney cancer suppressor gene. *Cancer Discov*, *1*(3), 222-235. https://doi.org/10.1158/2159-8290.Cd-11-0098

Siegel, R. L., Giaquinto, A. N., & Jemal, A. (2024). Cancer statistics, 2024. *CA: A Cancer Journal for Clinicians*, *74*(1), 12-49. https://doi.org/https://doi.org/10.3322/caac.21820

Siemerink, M. J., Klaassen, I., Vogels, I. M., Griffioen, A. W., Van Noorden, C. J., & Schlingemann, R. O. (2012). CD34 marks angiogenic tip cells in human vascular endothelial cell cultures. *Angiogenesis*, *15*(1), 151-163. https://doi.org/10.1007/s10456-011-9251-z

Singla, N., Xie, Z., Zhang, Z., Gao, M., Yousuf, Q., Onabolu, O., McKenzie, T., Tcheuyap, V. T., Ma, Y., Choi, J., McKay, R., Christie, A., Torras, O. R., Bowman, I. A., Margulis, V., Pedrosa, I., Przybycin, C., Wang, T., Kapur, P., . . . Brugarolas, J. (2020). Pancreatic tropism of metastatic renal cell carcinoma. *JCI Insight*, *5*(7). https://doi.org/10.1172/jci.insight.134564

Slaughter, M. J., Shanle, E. K., McFadden, A. W., Hollis, E. S., Suttle, L. E., Strahl, B. D., & Davis, I. J. (2018). PBRM1 bromodomains variably influence nucleosome interactions and cellular function. *J Biol Chem*, *293*(35), 13592-13603. https://doi.org/10.1074/jbc.RA118.003381

Sorensen, A. G., Emblem, K. E., Polaskova, P., Jennings, D., Kim, H., Ancukiewicz, M., Wang, M., Wen, P. Y., Ivy, P., Batchelor, T. T., & Jain, R. K. (2012). Increased survival of glioblastoma patients who respond to antiangiogenic therapy with elevated blood perfusion. *Cancer Res*, *72*(2), 402-407. https://doi.org/10.1158/0008-5472.Can-11-2464

Staton, C. A., Reed, M. W., & Brown, N. J. (2009). A critical analysis of current in vitro and in vivo angiogenesis assays. *Int J Exp Pathol*, *90*(3), 195-221. https://doi.org/10.1111/j.1365-2613.2008.00633.x

Steele, C. W., Karim, S. A., Leach, J. D. G., Bailey, P., Upstill-Goddard, R., Rishi, L., Foth, M., Bryson, S., McDaid, K., Wilson, Z., Eberlein, C., Candido, J. B., Clarke, M., Nixon, C., Connelly, J., Jamieson, N., Carter, C. R., Balkwill, F., Chang, D. K., . . . Morton, J. P. (2016). CXCR2 Inhibition Profoundly Suppresses Metastases and Augments Immunotherapy in Pancreatic Ductal Adenocarcinoma. *Cancer Cell*, *29*(6), 832-845. https://doi.org/10.1016/j.ccell.2016.04.014

Subramanian, A., Tamayo, P., Mootha, V. K., Mukherjee, S., Ebert, B. L., Gillette, M. A., Paulovich, A., Pomeroy, S. L., Golub, T. R., Lander, E. S., & Mesirov, J. P. (2005). Gene set enrichment analysis: a knowledge-based approach for interpreting genome-wide expression profiles. *Proc Natl Acad Sci U S A*, *102*(43), 15545-15550. https://doi.org/10.1073/pnas.0506580102

Tang, L., Nogales, E., & Ciferri, C. (2010). Structure and function of SWI/SNF chromatin remodeling complexes and mechanistic implications for transcription. *Prog Biophys Mol Biol*, *102*(2-3), 122-128. https://doi.org/10.1016/j.pbiomolbio.2010.05.001

Tazzyman, S., Lewis, C. E., & Murdoch, C. (2009). Neutrophils: key mediators of tumour angiogenesis. *Int J Exp Pathol*, *90*(3), 222-231. https://doi.org/10.1111/j.1365-2613.2009.00641.x

Team-TBD. (2023). BSgenome.Hsapiens.UCSC.hg38: Full genomic sequences for Homo sapiens (UCSC genome hg38). R package version 1.4.5. In https://bioconductor.org/packages/BSgenome.Hsapiens.UCSC.hg38/

Therneau, T. M. (2024). A Package for Survival Analysis in R. R package version 3.7-0. In https://CRAN.R-project.org/package=survival.

Therneau, T. M., & Grambsch, P. M. (2013). Modeling Survival Data: Extending the Cox Model. Springer New York. https://doi.org/10.1007/978-1-4757-3294-8

Tsherniak, A., Vazquez, F., Montgomery, P. G., Weir, B. A., Kryukov, G., Cowley, G. S., Gill, S., Harrington, W. F., Pantel, S., Krill-Burger, J. M., Meyers, R. M., Ali, L., Goodale, A., Lee, Y., Jiang, G., Hsiao, J., Gerath, W. F. J., Howell, S., Merkel, E., . . . Hahn, W. C. (2017). Defining a Cancer Dependency Map. *Cell*, *170*(3), 564-576.e516. https://doi.org/10.1016/j.cell.2017.06.010

Turajlic, S., Xu, H., Litchfield, K., Rowan, A., Chambers, T., Lopez, J. I., Nicol, D., O'Brien, T., Larkin, J., Horswell, S., Stares, M., Au, L., Jamal-Hanjani, M., Challacombe, B.,

Chandra, A., Hazell, S., Eichler-Jonsson, C., Soultati, A., Chowdhury, S., . . . Swanton, C. (2018). Tracking Cancer Evolution Reveals Constrained Routes to Metastases: TRACERx Renal. *Cell*, *173*(3), 581-594.e512. https://doi.org/10.1016/j.cell.2018.03.057

Turajlic, S., Xu, H., Litchfield, K., Rowan, A., Horswell, S., Chambers, T., O'Brien, T., Lopez, J. I., Watkins, T. B. K., Nicol, D., Stares, M., Challacombe, B., Hazell, S., Chandra, A., Mitchell, T. J., Au, L., Eichler-Jonsson, C., Jabbar, F., Soultati, A., . . . Swanton, C. (2018). Deterministic Evolutionary Trajectories Influence Primary Tumor Growth: TRACERx Renal. *Cell*, *173*(3), 595-610.e511. https://doi.org/10.1016/j.cell.2018.03.043

Van Coillie, E., Van Aelst, I., Wuyts, A., Vercauteren, R., Devos, R., De Wolf-Peeters, C., Van Damme, J., & Opdenakker, G. (2001). Tumor angiogenesis induced by granulocyte chemotactic protein-2 as a countercurrent principle. *Am J Pathol*, *159*(4), 1405-1414. https://doi.org/10.1016/s0002-9440(10)62527-8

Varela, I., Tarpey, P., Raine, K., Huang, D., Ong, C. K., Stephens, P., Davies, H., Jones, D., Lin, M. L., Teague, J., Bignell, G., Butler, A., Cho, J., Dalgliesh, G. L., Galappaththige, D., Greenman, C., Hardy, C., Jia, M., Latimer, C., . . . Futreal, P. A. (2011). Exome sequencing identifies frequent mutation of the SWI/SNF complex gene PBRM1 in renal carcinoma. *Nature*, *469*(7331), 539-542. https://doi.org/10.1038/nature09639

Vetsika, E. K., Koukos, A., & Kotsakis, A. (2019). Myeloid-Derived Suppressor Cells: Major Figures that Shape the Immunosuppressive and Angiogenic Network in Cancer. *Cells*, *8*(12). https://doi.org/10.3390/cells8121647

Wanior, M., Kramer, A., Knapp, S., & Joerger, A. C. (2021). Exploiting vulnerabilities of SWI/SNF chromatin remodelling complexes for cancer therapy. *Oncogene*, *40*(21), 3637-3654. https://doi.org/10.1038/s41388-021-01781-x

Wanior, M., Preuss, F., Ni, X., Krämer, A., Mathea, S., Göbel, T., Heidenreich, D., Simonyi, S., Kahnt, A. S., Joerger, A. C., & Knapp, S. (2020). Pan-SMARCA/PB1 Bromodomain Inhibitors and Their Role in Regulating Adipogenesis. *J Med Chem*, *63*(23), 14680-14699. https://doi.org/10.1021/acs.jmedchem.0c01242

Wickham, H. (2016). ggplot2 : Elegant Graphics for Data Analysis (2nd ed.). Springer International Publishing : Imprint: Springer. https://doi.org/10.1007/978-3-319-24277-4

Willett, C. G., Boucher, Y., di Tomaso, E., Duda, D. G., Munn, L. L., Tong, R. T., Chung, D. C., Sahani, D. V., Kalva, S. P., Kozin, S. V., Mino, M., Cohen, K. S., Scadden, D. T., Hartford, A. C., Fischman, A. J., Clark, J. W., Ryan, D. P., Zhu, A. X., Blaszkowsky, L. S., . . . Jain, R. K. (2004). Direct evidence that the VEGF-specific antibody bevacizumab has antivascular effects in human rectal cancer. *Nat Med*, *10*(2), 145-147. https://doi.org/10.1038/nm988

Winkler, F., Kozin, S. V., Tong, R. T., Chae, S. S., Booth, M. F., Garkavtsev, I., Xu, L., Hicklin, D. J., Fukumura, D., di Tomaso, E., Munn, L. L., & Jain, R. K. (2004). Kinetics of vascular normalization by VEGFR2 blockade governs brain tumor response to radiation: role of oxygenation, angiopoietin-1, and matrix metalloproteinases. *Cancer Cell*, *6*(6), 553-563. https://doi.org/10.1016/j.ccr.2004.10.011

Wu, F., Zhao, Y., Jiao, T., Shi, D., Zhu, X., Zhang, M., Shi, M., & Zhou, H. (2015). CXCR2 is essential for cerebral endothelial activation and leukocyte recruitment during

neuroinflammation. *Journal of Neuroinflammation*, *12*(1), 98. https://doi.org/10.1186/s12974-015-0316-6

Xia, W., Nagase, S., Montia, A. G., Kalachikov, S. M., Keniry, M., Su, T., Memeo, L., Hibshoosh, H., & Parsons, R. (2008). BAF180 is a critical regulator of p21 induction and a tumor suppressor mutated in breast cancer. *Cancer Res*, *68*(6), 1667-1674. https://doi.org/10.1158/0008-5472.Can-07-5276

Yagoda, A., Petrylak, D., & Thompson, S. (1993). Cytotoxic chemotherapy for advanced renal cell carcinoma. *Urol Clin North Am*, *20*(2), 303-321.

Yao, X., Hong, J. H., Nargund, A. M., Ng, M. S. W., Heng, H. L., Li, Z., Guan, P., Sugiura, M., Chu, P. L., Wang, L. C., Ye, X., Qu, J., Kwek, X. Y., Lim, J. C. T., Ooi, W. F., Koh, J., Wang, Z., Pan, Y. F., Ong, Y. S., Tan, K. Y., … Teh, B. T. (2023). PBRM1-deficient PBAF complexes target aberrant genomic loci to activate the NF-κB pathway in clear cell renal cell carcinoma. *Nature cell biology*, *25*(5), 765–777. https://doi.org/10.1038/s41556-023-01122-y

Ye, W. (2016). The Complexity of Translating Anti-angiogenesis Therapy from Basic Science to the Clinic. *Dev Cell*, *37*(2), 114-125. https://doi.org/10.1016/j.devcel.2016.03.015

Yetkin-Arik, B., Vogels, I. M. C., Nowak-Sliwinska, P., Weiss, A., Houtkooper, R. H., Van Noorden, C. J. F., Klaassen, I., & Schlingemann, R. O. (2019). The role of glycolysis and mitochondrial respiration in the formation and functioning of endothelial tip cells during angiogenesis. *Scientific Reports*, *9*(1), 12608. https://doi.org/10.1038/s41598-019-48676-2

Young, M., Jackson-Spence, F., Beltran, L., Day, E., Suarez, C., Bex, A., Powles, T., & Szabados, B. (2024). Renal cell carcinoma. *The Lancet*. https://doi.org/https://doi.org/10.1016/S0140-6736(24)00917-6

Yu, G., Wang, L. G., Han, Y., & He, Q. Y. (2012). clusterProfiler: an R package for comparing biological themes among gene clusters. *Omics*, *16*(5), 284-287. https://doi.org/10.1089/omi.2011.0118

Zaware, N., & Zhou, M.-M. (2019). Bromodomain biology and drug discovery. *Nature Structural & Molecular Biology*, *26*(10), 870-879. https://doi.org/10.1038/s41594-019-0309-8

Zhang, Y., Zhu, C., Sun, B., Lv, J., Liu, Z., Liu, S., & Li, H. (2017). Integrated High Throughput Analysis Identifies GSK3 as a Crucial Determinant of p53-Mediated Apoptosis in Lung Cancer Cells. *Cell Physiol Biochem*, *42*(3), 1177-1191. https://doi.org/10.1159/000478873

Zhao, P., Li, Q., Shi, Z., Li, C., Wang, L., Liu, X., Jiang, C., Qian, X., You, Y., Liu, N., Liu, L. Z., Ding, L., & Jiang, B. H. (2015). GSK-3β regulates tumor growth and angiogenesis in human glioma cells. *Oncotarget*, *6*(31), 31901-31915. https://doi.org/10.18632/oncotarget.5043

9. Acknowledgements

First and foremost, I would like to express my sincere gratitude to my PhD supervisors, PD. Dr. Niklas Klümper and Prof. Dr. med. Michael Hölzel, for giving me the opportunity to explore various intriguing topics in their laboratories. I deeply appreciate their brilliant ideas, insightful discussions, and thoughtful guidance. Their extensive knowledge and relentless support have greatly contributed to my academic development and success. I am especially grateful to PD. Dr. Niklas Klümper, my direct mentor, for being not only an inspiring physician-scientist but also a generous and kind person. He created an environment that fostered my scientific growth, always welcomed my ideas and questions, and kept me focused on my goals.

I would also like to extend my thanks to Prof. Dr. med. Manuel Ritter for allowing me to join the Department of Urology and conduct my PhD research in a clinical and translational lab, where I was able to experience the vital intersection of clinical practice and scientific research.

My sincere appreciation goes to Prof. Dr. med. Kerstin Junker for being my second reviewer and Prof. Dr. med. Marieta Toma for being a part of my PhD committee. Thank you both for your time and assistance.

I am deeply grateful to Ms. Miriam Saponaro and Mrs. Anja Winkler, my dear colleagues and friends, without whom this work would not have been possible. Thank you for your scientific and emotional support, as well as for your indispensable help in the lab, especially during difficult times. The moments of joy and camaraderie we shared will never be forgotten.

I would also like to thank my immediate colleagues, Mrs. Doris Schmidt, Mrs. Karin Wörsdörfer, and Ms. Sana Hosni, for their generosity in offering help and advice, and for contributing to making the lab such a wonderful place to work.

A special thank you to the entire Institute of Experimental Oncology and Department of Urology for providing a supportive and collaborative working environment throughout my PhD. Your advice and encouragement have been invaluable.

I would like to express my deepest gratitude to my parents, Mrs. Tuyen Thi Kim Ho and Mr. Khanh Tran, for their boundless love and unshakeable belief in me, supporting me every step of the way. My sincerest thanks to my boyfriend, Mr. Truong Nhat Nguyen, for being my constant rock and for cheering me on through every challenge.

I also owe so much to my extended family and friends in Vietnam, as well as to my mentor in America. Despite the distance, your love and encouragement have given me the strength and confidence to complete my PhD in Germany.

Last but not least, I dedicate this work to my younger brother, Mr. Hung Khanh Tran, who is no longer with us. His absence leaves a permanent void in my life, and I will always carry him in my heart.

"*Was ist das Schwerste von allem? Was dir das Leichteste dünket:*
Mit den Augen zu sehn, was vor den Augen dir lieget."

Johann Wolfgang von Goethe

10. List of publication

NECTIN4 Amplification Is Frequent in Solid Tumors and Predicts Enfortumab Vedotin Response in Metastatic Urothelial Cancer

Journal of clinical oncology. 2024;42(20):2446-2455. doi:10.1200/JCO.23.01983

Niklas Klümper[*], **Ngoc Khanh Tran**[*], Stefanie Zschäbitz, Oliver Hahn, Thomas Büttner, Florian Roghmann, Christian Bolenz, Friedemann Zengerling, Constantin Schwab, Dora Nagy, Marieta Toma, Glen Kristiansen, Hendrik Heers, Philipp Ivanyi, Günter Niegisch, Camilla Marisa Grunewald, Christopher Darr, Arian Farid, Katrin Schlack, Mahmoud Abbas, Can Aydogdu, Jozefina Casuscelli, Theresa Mokry, Michael Mayr, Dora Niedersüß-Beke, Steffen Rausch, Dimo Dietrich, Jonas Saal, Jörg Ellinger, Manuel Ritter, Abdullah Alajati, Christoph Kuppe, Joshua Meeks, Francisco E. Vera Badillo, J Alberto Nakauma-González, Joost Boormans, Kerstin Junker, Arndt Hartmann, Viktor Grünwald, Michael Hölzel[#], Markus Eckstein[#]

[*, #] These authors contributed equally.